Materials Design for Advanced Nuclear Energy Systems: Refractory High Entropy Alloys and Metallic Multilayer Composites

by

Samuel W. McAlpine

B.S., University of California, Berkeley (2015)

Submitted to the Department of Nuclear Science and Engineering
in partial fulfillment of the requirements for the degree of

Doctor of Philosophy in Nuclear Science and Engineering

at the

MASSACHUSETTS INSTITUTE OF TECHNOLOGY

February 2022

Author .....
Department of Nuclear Science and Engineering
November 30, 2021

Certified by .....
Prof. Michael P. Short
Class of '42 Associate Professor of Nuclear Science and Engineering
Thesis Supervisor

Certified by .....
Prof. C. Cem Tasan
Thomas B. King Associate Professor of Metallurgy
Thesis Reader

Accepted by .....
Prof. Ju Li
Chairman, Department Committee on Graduate Studies
Battelle Energy Alliance Professor of Nuclear Science and Engineering
Professor of Materials Science and Engineering

Materials Design for Advanced Nuclear Energy Systems: Refractory High Entropy Alloys and Metallic Multilayer Composites

by

Samuel W. McAlpine

Submitted to the Department of Nuclear Science and Engineering
on November 30, 2021, in partial fulfillment of the
requirements for the degree of
Doctor of Philosophy in Nuclear Science and Engineering

Abstract

Advanced nuclear reactors present a multitude of materials challenges due to high operating temperatures, corrosive environments, and neutron radiation damage. In this thesis, I focus on two approaches to designing better materials for advanced reactors, high entropy alloys (HEAs) and metallic multilayer composites (MMLCs). HEAs are chemically disordered solid solutions combining 4-5 or more elements, which often have superior mechanical properties and radiation damage tolerance compared to advanced steels and Ni-base alloys. While HEAs have garnered immense attention within the research community, there is still no effective approach for predicting which compositions will tend to form a single phase microstructure. I develop an atomistic thermodynamic model which uses a quantity I coin as the atomistic mixing energy (AME) to understand phase stability in HEAs and predict which elements are more or less favored to mix within a given HEA system. The model also facilitates the correct calculation of the vacancy formation energy distribution in HEAs which gives insight to radiation damage, solid–state diffusion, and other vacancy–driven material behavior. To test the validity of the model, I synthesize and characterize 5 refractory HEA compositions: NbMoTaTiW, NbMoTaTiV, NbMoTaTiZr, NbMoTaHfW, and WTaVTiCr. Implications for single phase HEA design utilizing the model developed in this thesis are explored. The final part of the thesis focuses on MMLCs, in which different material functionalities are separated into different layers. Currently, few studies have aimed to understand radiation damage effects at the interface between different layers. I use interfacial self–ion irradiation along the bimetal interface within 2 MMLC systems to shed light on the radiation damage behavior of the interfacial region. Radiation–enhanced diffusion was observed in one MMLC, and a Cr-rich phase is observed along the interface in both MMLCs. The propensity for radiation–enhanced diffusion is related to the compositional gradient across the interface, while the Cr-rich interfacial phase could potentially lead to material embrittlement within MMLCs.

Thesis Supervisor: Prof. Michael P. Short
Title: Class of '42 Associate Professor of Nuclear Science and Engineering

Thesis Reader: Prof. C. Cem Tasan
Title: Thomas B. King Associate Professor of Metallurgy

Acknowledgments

First, I would like to express my gratitude towards my doctoral thesis advisor, Prof. Michael Short. I feel extremely fortunate to have ended up pursuing graduate studies at MIT under your mentorship. Although you have taught me a great deal about science, engineering, and research, the thing I will remember and cherish the most is your constant and unwavering support through the many personal and professional ups and downs of graduate school. I hope that as we move in to the future we continue to work together and collaborate, striving to understand more about the world and come up with creative solutions to the challenges we face. I am also very grateful to the other members of my thesis committee, Prof. Cem Tasan and Prof. Ju Li, for providing valuable feedback during my thesis writing and for serving as academic role models.

I am very fortunate to have ended up in a collaborative, social research group that facilitated by personal and scientific development more than I ever could have imaged. Although I have come to know many people through our research group, the MIT Mesoscale Nuclear Materials group, I would like to specifically name a few that I had a chance to spend many hours with in the lab and office: Weiyue, Charlie, Rachel, Sara, Cody, Andrew, Penghui, Max, Ben, Sean, Reid, Miaomiao, Julie and many more not named here. I am also very fortunate to have had the priveledge to serve as the Graduate Resident Assistant (GRA) for House 2 within New House. I have so many fond memories of Waffle Wednesdays, movie nights, and spontaneous deep conversations. I learned so much from House 2, and being a GRA helped me find meaning within my place in the MIT community.

I would like to acknowledge my immediate family, my parents Ed McAlpine and Anne Chambers and my brother Henry, for loving and supporting me throughout my educational journey. In addition to my immediate family, I have a large extended family who have been critical to my personal development as well. In particular, I

would like to acknowledge my late grandfather Robert R. Chambers, who received his Ph.D. in Chemistry from the University of Illinois, for his support of my education and dedication to helping spark an interest in science within me and a desire to understand more about the world. I would not be here without his influence.

Most importantly, I would like to thank my partner and future wife Jessica Coleman for constant support through all the ups and downs of grad school. I consider myself to be lucky in many ways, but I am most thankful that life brought us together and we have been able to grow together and support eachother in pursuing our dreams.

Finally, I would like to dedicate this thesis to my friend Matthew Brennan, who passed away suddenly on January 26, 2021. Matthew was on track to finish his PhD and move on to a prestigious postdoctoral fellowship at my alma mater, the University of California, Berkeley. Although Matthew was brilliant in many ways, what I will always remember was his unending, genuine kindness. I will carry his memory with me for the rest of my days and strive to treat others with the same kindness he did. Rest in peace.

Contents

List of Figures

List of Tables

Chapter 1

Introduction

Arguably the most difficult technical challenge facing humanity in the modern era is the emission of green house gases (GHG) such as methane and carbon dioxide associated with combustion of fossil fuels for energy. Although a complex solution is required for such a huge challenge, one key component is the development of alternative energy sources which do not directly produce GHG emissions, in order to allow people to live a high–quality, energy–intensive existence without necessarily producing harmful emissions as a result. Renewable sources of energy such as wind, solar, and geothermal are promising solutions for carbon-free energy production, but all sources of energy have certain drawbacks. First and foremost, solar and wind energy are obviously intermittent sources of energy - because they are natural there is no control to set a baseline level of power production, simply a capacity. Geothermal energy has many advantages but there are only a certain number of geothermal energy sources available which creates an inherent challenge of scalability. Nuclear energy stands alone as a technology capable of fully replacing the existing coal–fired and natural gas power plants which are the primary generators of baseload electricity in a manner which is scalable and can be located in many geographic settings, while producing no direct GHG emissions. Therefore, investment in the development, improvement, and deployment of nuclear technology for energy production is crucial to human civilization going forward. In this thesis, I focus on materials innovations that are critical to the development and operation of advanced nuclear energy systems in

the future, which likely will demand materials which can survive in more extreme environments for longer amounts of time than commercially available materials can achieve.

1.1 The Need for New Nuclear Materials

In order to harness the capacity of nuclear technology to produce useful electricity for productivity and enjoyment, suitable materials must be used to construct and operate the nuclear power plant in a safe, cost–effective manner. Although many different types of advanced nuclear reactor technologies have been developed, from the ARC fusion reactor, to the FHR molten salt reactor, to the liquid sodium–cooled fast reactors, these reactors remain, in the words of Admiral Hyman G. Rickover mostly "paper reactors" [1]. That being said, water–cooled nuclear reactors have served the human population effectively for decades, producing carbon–free electricity with overall little negative environmental consequences, with the exception of several severe and captivating nuclear accidents such as Chernobyl, Three Mile Island (TMI), and Fukushima Daiichi. Although some prototype reactors have been constructed, such as the molten salt reactor experiment (MSRE) designed primarily by Alvin Weinberg at Oak Ridge National Laboratory (ORNL) [2], for many reactor concepts there are not currently sufficient structural materials that can withstand the conditions in these reactors for several years to decades.

Although light-water reactors (LWRs) dominate the commercial nuclear energy industry, one successful implementation of advanced reactor technology is the high temperature gas–cooled reactor (HTGR) including the Fort St. Vrain Generating Station in Colorado which operated from 1979 to 1989, as well as a more recent development in China where the HTR–PM small modular HTGR has become the first commercially deployed Generation IV technology at the Shidao Bay Nuclear Power Plant. These HTGR designs use a He gas coolant, and the Fort St. Vrain Generating Station experienced water infiltration within the coolant which lead to major

corrosion issues [3]. Murty and Charit point out that along with challenges associated with determining a material with sufficient radiation damage and dimensional stability, corrosion resistance, and high temperature creep strength, the fabricability and weldability of the material are major engineering challenges which must be overcome as well [4]. We can consider there to be significant gaps in both the alloy and microstructural design of sufficient materials as well as the engineering required to build, qualify, and commercialize advanced nuclear technology.

Some of the primary challenges which materials need to overcome are the retention of high yield strength at operating temperatures of up to 700°C and beyond in some advanced designs, resistance to corrosion by highly corrosive coolants such as fluoride molten salts and liquid Pb, and tolerance to radiation damage by the energetic neutrons produced by the nuclear reactor, which can cause up to 100 dpa radiation damage or more in some fast reactor designs. Shown in Figure 1-1 is a diagram showing different advanced nuclear energy systems and the degradation characteristics of those designs in terms of temperature, corrosion, and radiation damage [5].

There is a fundamental gap between the performance of generally available materials and those required of materials in advanced nuclear reactors. One could view this gap in terms of fundamental contradictions as coined in the TRIZ system [6] as fundamental physical conflicts. In essence, the major classes of metallic materials have fundamental drawbacks which require further development to overcome. Advanced ferritic–martensitic steels for liquid metal fast reactor applications such as EK-181 [7] and EP-823 [8] developed in Russia, along with US–developed counterparts such as HT9 [9] and T92 [10], have generally good resistance to radiation damage and decent corrosion resistance due to their Cr content, but become fundamentally limited by creep deformation at operating temperatures above 600°C. The MSRE at ORNL facilitated the development of a Ni–base superalloy Hastelloy N (Ni–16Mo–7Cr–5Fe wt %) which has reasonable corrosion resistance in molten salt environments, along with good high temperature mechanical properties and void swelling resistance [11]. One

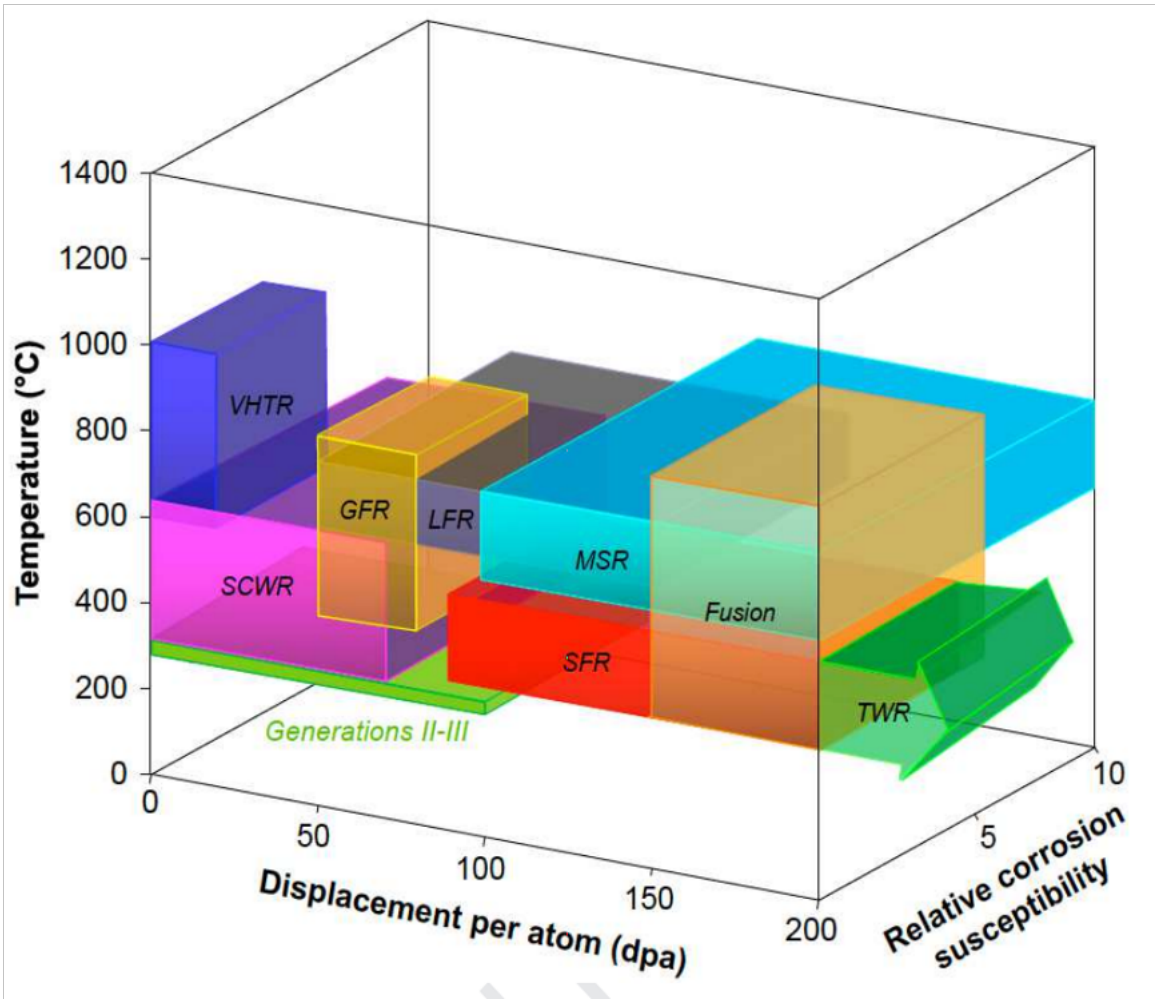

Figure 1-1: A diagram of materials degradation space for various advanced nuclear energy systems demonstrating the temperature, corrosion, and radiation damage for different designs (from [5])

effect was found of irradiation–enhanced creep rupture of Hastelloy N during high temperature creep tests with neutron irradiation, driven by He–induced grain boundary creep due to impurity boron causing He production through (n, α) reactions. This led to the development of modified Hastelloy N, containing small amounts of Nb or Ti in order to form boride precipitates and eliminate He production throughout the matrix, alleviating the radiation–enhanced creep rupture challenge [12]. Although Hastelloy N has many positive attributes, the Cr content within the alloy causes some susceptibility to Te–induced stress corrosion cracking in molten salt environments [13]. Simply put, advanced reactors pose so many extreme challenges for materials that in gen-

eral it is unlikely a single conventional alloy can meet these challenges simultaneously.

This thesis will focus on materials design using two distinct approaches. The first part of the thesis focuses on high entropy alloys (HEAs), which are not precisely defined and sometimes can be called many different names such as concentrated solid solution alloys (CSSAs), compositionally complex alloys (CCAs), and several other variations. The basic, underlying idea behind all these materials is moving beyond the concept of a single "base" metal (Fe in steels, Al in lightweight Al-alloys, etc) towards an equiatomic (or nearly equiatomic) mixture of metals to form a single–phase solid solution with overall beneficial properties. The second part of this thesis is focused on the design of metallic multilayer composite materials, a subset of functionally graded composites which applies spatial gradients of different elements in order to create a material which performs better overall than any of the constituent elements. This arises due to the functional separation of surface–related material phenomena, and what I will refer to as bulk/volumetric material phenomena. Examples of surface–related material degradation phenomena are corrosion, wear/fretting, and fouling. Examples of bulk/volumetric material phenomena include temperature/thermal effects, mechanical stress, and neutron–inducedba radiation damage. By combining the beneficial properties of mutliple metallic materials through a layering strategy,

The focus of this thesis will be on the design of materials for a variety of different nuclear energy systems. Although the specific material characteristics which are required depend on the details of the reactor design (ex: fast vs. thermal reactor, coolant, operating temperature) we can think of the nuclear materials challenge as the pursuit of a material which can survive and maintain necessary properties in high temperature, corrosive conditions along with the defect–producing neutron flux present in nuclear energy systems. There are several common material design approaches that I will briefly mention, and offer a rationale for down–selection.

1.2 Modern Nuclear Materials Design

In this section I briefly describe several general approaches to development of novel materials for advanced nuclear energy and other extreme high–temperature applications. A general overview of each approach is presented along with a brief summary of my personal perspective on the technical advantages and challenges associated with each approach.

Ceramic Composites

In general ceramics, ionically bonded solids, have certain material properties which are highly beneficial for certain types of nuclear applications, and certain drawbacks. Engineering ceramics, such as metal carbides, nitrides, and oxides, tend to have quite high melting points in comparison to pure metals. This can be highly beneficial for certain components in nuclear reactors in which melting would be a catastrophic reactor failure, such as the fuel and the control rod. Ceramics also tend to be very hard and strong materials, which is a beneficial in some ways but also corresponds to a highly brittle response where ceramics demonstrate almost no plastic deformation before fracture. So, although ceramics are very strong and have a high melting point, they have not been used extensively as structural materials in nuclear reactors due to their brittle nature. That being said, the most common nuclear fuel (UO_2) is a ceramic, and ceramics have played an important role in the "core catcher", which is a ceramic concrete plate installed under LWRs in order to contain molten reactor core material in case of a severe nuclear accident [14, 15]. So, although ceramics themselves seem to have limited applicability in advanced nuclear energy systems, several ceramic composite materials have been developed to enhance the potential functionality of ceramics.

One example of modern ceramic composite materials is TRISO fuel, which can survive without melting in accident scenarios and have been shown to have a very high degree of fission produce retention due to a layered carbon material design [16]. Within

the world of structural nuclear materials, the most important ceramic composite is SiC/SiC. Although, generally speaking SiC is very brittle like most other ceramics, pseudo–plastic behavior is achieved through a fiber/matrix composite design in which the material can pseudo–plastically deform through fiber "pulling out" of the SiC matrix [17, 18]. Unfortunately, the scaled production of SiC/SiC fiber/matrix composites is very challenging, and even the most modern techniques such as NITE (nano–infiltration transient eutectic) do not perform particularly well in forming a continuous matrix with no porosity [19].

Another recently popularized approach to nuclear materials design involving ceramics is the MAX phase approach, which are complex lamellar compounds consisting of a transition metal, an element from group A typically Al or Si, along with carbon or nitrogen [20–22]. Although MAX phases are promising in terms of combining the benefits of ceramics and refractory metals, in practice synthesis of these materials is difficult and often yields a multiphase composite microstructure including the MAX phase, intermetallic, and metal carbides [23].

Oxide–Dispersion Strengthened (ODS) Alloys

Oxide–dispersion strengthened (ODS) alloys have been shown to possess highly beneficial radiation damage tolerance and high temperature creep–resistance characteristics [24]. The general design concept is that the introduction of a high volume fraction of incoherent interfaces within the material provides a large sink density for point defects, significantly improving the radiation damage resistance and resistance to creep deformation. ODS alloys have ceramic oxide nanoparticles of compounds such as yttria (Y_2O_3) and titania (TiO_2) dispersed within a metallic matrix, most frequently a ferritic steel such as FeCrAl [25]. These oxide nanoparticles tend to be found at GBs or triple junctions within the ODS material, where the oxide forms an incoherent interface with the surrounding metallic matrix. This incoherent interface serves as a strong sink for point defects, which allows ODS materials to suppress the population and migration of point defects (vacancies and interstitials). Because point defects

play a key role in the mechanisms of radiation damage and creep, this allows ODS materials to demonstrate superior performance compared to conventional advanced steels [26]. The major drawback of ODS materials is the complex, difficult process by which these materials are synthesized [27]. Namely, the extensive ball–milling and sintering required to achieve the desired ODS nanostructure makes these materials very difficult to manufacture and also very challenging to machine. These challenges have limited the broad application of ODS alloys in nuclear energy systems despite the exceptional properties of this class of materials.

Metallic Multilayer Composites (MMLC)

MMLCs have been used in light-water reactors (LWRs), the current generation of nuclear reactors, as the reactor pressure vessels (RPV) is clad with stainless steel. These RPVs are clad with a duplex stainless steel (308SS) in order to prevent the corrosion of the RPV by the highly corrosive reactor water, which is not only at a high temperature and pressure but also contains compounds such as boric acid which are used as a burnable poison in the reactor but are also known to accelerate the corrosion of steel [28]. This has worked overall relatively successfully with the notable exception of one close–call relating to these materials which could have been catastrophic. This incident was known as the Davis–Besse incident as it occurred at one of the reactors at the Davis–Besse power plant in Ohio [29]. In this case, the low–alloy steel RPV was exposed to boric acid due to a crack in the RPV head, and it corroded through all the way to the overlay inner layer, and was identified before rupture preventing a catastrophic accident.

There has been an active field of study in the development of accident–tolerant fuel (ATF) for light water reactors in order to achieve materials with superior oxidation–resistance during severe accidents while maintaining sufficient neutronic performance. This includes innovations in fuel materials but also in fuel cladding materials, which are now commonly coated with different oxidation–resistant coatings. Although several oxidation–resistant materials have been proposed, including the SiC/SiC fiber/-

matrix composites mentioned earlier, oxidation–resistant FeCrAl, and Cr-coated Zircaloy fuel cladding, none are widely deployed at this point in time. In addition to accident tolerance, a challenge with pellet-cladding interactions (PCI) has led to so–called barrier fuel consisting of Zircaloy fuel cladding with a pure Zr barrier lining the inner diameter of the fuel cladding tube [30, 31]. A similar idea has been proposed for barrier layers for metallic fuels which utilize aluminum alloy fuel cladding with a refractory metal barrier layer lining [32] for sodium fast reactors.

The MMLC design approach has great potential for rapid innovation in the nuclear materials area, especially in terms of modifying already qualified materials for enhanced performance in highly corrosive environments. For instance, Incoloy 800H is approved for high temperature nuclear applications under the american society of mechanical engineers (ASME) boiler and pressure vessel (B&PV) code, yet is highly susceptible to corrosion in common nuclear coolants such as fluoride molten salts and liquid lead. A necessary aspect of the MMLC approach is the introduction of atleast one bimetal interface throughout the material. The joining of layers to form the interface is a challenge from a manufacturing perspective, but also little is known about the materials science of such bimetal interfaces in conditions of high temperature and radiation damage. For instance, thermally–driven diffusion can reduce the compositional gradient between layers and in some cases degrade the performance of the MMLC. The extent to which radiation damage and radiation–enhanced diffusion may be important in these systems is unknown. In the final primary chapter of the thesis I explore the question of whether the MMLC design approach can comprehensively be used to separate functionality into different layers of a material, with one of the layers in particular providing the high temperature strength and mechanical properties necessary for the structural aspects of the material in addition to resilience under neutron radiation damage, while another layer provides the resistance to corrosion from the operational environment.

High Entropy Alloys

High Entropy Alloys (HEAs) are a more recently–developed materials concept which moves the field of physical metallurgy towards more disordered solid solutions compared to dilute alloys based on common materials such as steel or Al, or even the modern Fe-Ni-Cr solid solution alloys which are commonly used for high temperature nuclear applications such as Incoloy 800H. HEAs are demonstrated to have several beneficial properties, such as radiation–damage tolerance [33–35], extremely high strength and ductility at cryogenic temperatures [36], among others intriguing properties such as superconductivity in some refractory HEA systems [37]. Although these materials show a high degree of promise, and do not necessarily have the inherent brittleness challenges that come with ceramics or the processing challenges of ODS materials, there is a lack of fundamental understanding within this relatively novel field. For instance, part of the primary rationale for the usage of HEAs is the stabilization of a single solid solution phase as opposed to the formation of a complex, multiphase microstructure. For HEAs composed of refractory metals, the challenge largely revolves around the challenge in determing a composition which has ductility, as the few single–phase refractory HEAs which have been identified generally lack ductility [38, 39]. Within the field of nuclear materials, particular interest has turned to refractory HEAs for low–activation applications in nuclear energy [40, 41]. Refractory HEAs in particular are generally found to take the BCC crystal structure [42].

Although HEAs are a more recent conceptual development, there has been an explosion of interest in these materials within the research community [43]. The fundamental thermodynamic behavior of these systems is still a somewhat open question in that there is no commonly accepted approach for determining which HEA compositions will tend to form a single–phase microstructure as opposed to a more complex multiphase microstructure.

1.3 Thesis Structure

The first part of this thesis will focus on HEAs. Specifically, I develop a new model and method of analyzing the thermodynamics of HEAs in order to better understand the energetics of mixing to gain insights into the design of single–phase HEAs. In order to test the validity of the model on materials relevant to nuclear applications and other high temperature environments, several refractory HEAs are analyzed in order to determine the mixing thermodynamics of those refractory HEAs as well as the distribution of the vacancy formation energy across different sites within the HEA. In addition to first–principles thermodynamic analysis, the refractory HEAs are also synthesized at a laboratory–scale using an arc melter, then sectioned, polished and characterized in order to determine the microstructural characteristics of the material. Connections are drawn between the behavior predicted by the first–principles model and the observed behavior in the synthesized materials. Design implications for HEAs and other single–phase complex solid solutions are discussed in addition to future research directions that are enabled by the model.

The second part of this thesis will focus on MMLCs, specifically examining the effects of radiation damage at the interface of the material. Heavy ion irradiation is conducted on diffusion–bonded MMLCs in order to rapidly emulate the effects of neutron radiation damage. Two different layered metal composites are examined by irradiation and sectioning, polishing, scanning electron microscopy in addition to electron microprobe analysis. The insights these observations provide to the understanding of MMLCs applied in nuclear energy systems is discussed, and further directions of inquiry are outlined in order to assess the applicability of MMLC designs in advanced nuclear energy systems.

The choice to focus on these two classes of materials/design approaches is based on exploiting the intrinisic ductility metals often have. The processing and engineering required for utilizing a ceramic–based material in a nuclear reactor for structural

applications is exceedingly difficult, so I have chosen to focus on metallic systems. In some ways they are opposite approaches. In HEAs, the disordered metallic material introduces new operable mechanisms to the material such as different mechanisms of plasticity like twinning–induced plasticity (TWIP) or transformation–induced plasticity (TRIP) [44–46], or the stabilization of "deep trap" defect sites and slowing of diffusion which are believed to alleviate radiation damage. In essence, the idea is to create a material with synergies that make it greater than the sum of elemental parts. On the other hand, in MMLCs the layers are purposefully separated to exploit the beneficial properties of multiple alloys within the same material. One could even potentially imagine a combination of these concepts, particularly if a refractory HEA with outstanding mechanical properties and radiation damage tolerance were to be developed, it might be combined with a specific corrosion–resistant alloy for a material combining the benefits of both design approaches.

Chapter 2

Background: Solid Solution Thermodynamics

In this chapter I will briefly review existing thermodynamic models for mixing in metallic solid solution alloys. The primary purpose of this chapter is to set the stage for the atomistic thermodynamic model for HEAs developed in the following chapter. I begin by focusing on the case of binary mixing and illustrate the characteristics and assumptions of the ideal, regular, and quasichemical solid solution models. Although HEA mixing is clearly more complicated than the case of binary mixing, these binary models help demonstrate the critical concepts in HEA thermodynamics. Then, I discuss current models used for predicting mixing behavior in HEAs before developing my atomistic mixing model in the following chapter. Knowledge of the basic concepts of alloy thermodynamics is critical for metallurgists and nuclear materials engineers developing new materials, especially because the formation of intermetallic precipitates can often lead to embrittlement and loss of ductility.

The thermodynamic equilibrium of a solution depends on global minimization of the free energy of the system. Typically the Gibbs free energy G, which is applicable in conditions of fixed temperature and pressure is applied to solid solutions:

$$G = H - TS \tag{2.1}$$

where H is the enthalpy of the system, S is the entropy of the system, and T is absolute temperature. The enthalpy H can be further expanded as:

$$H = U + PV \tag{2.2}$$

where U is the internal energy of the system, P is the pressure, and V is the volume of the system. For condensed matter systems (solids and liquids), it is widely accepted that $PV << U$ and therefore the enthalpy and internal energy are roughly equivalent and can be used interchangably. Furthermore, the Helmholtz free energy F, which is the applicable thermodynamic potential under conditions of fixed temperature and volume, can be considered as equivalent and interchangable with the Gibbs free energy in a condensed matter system:

$$F = U - TS \approx G \tag{2.3}$$

The thermodynamic equilibrium state is ultimately determined by which phase or combination of phases minimizes the free energy of the entire system. When considering a binary mixture of metals A and B, the change in free energy associated with mixing can be written as

$$\Delta F_{mix} = F - F_A^\circ X_A - F_B^\circ X_B \tag{2.4}$$

Where F is the molar free energy of the A–B mixture, F_A° and F_B° are the molar free energies of pure A and pure B respectively, and X_A and X_B are the atomic fractions of the different elements within the mixture.

$$X_B = \frac{N_B}{N_A + N_B} = 1 - X_A \tag{2.5}$$

We can also express the free energy of mixing more generally for an alloy with $\mathcal{C}$ components

$$\Delta F_{mix} = F - \sum_i^{\mathcal{C}} X_i F_i^\circ \tag{2.6}$$

where $X_i = N_i/N$ and N is the total number of atoms in the system. The free energy change of mixing can be partitioned into energetic and entropic components:

$$\Delta F_{mix} = \Delta U_{mix} - T\Delta S_{mix} \tag{2.7}$$

where ΔU_{mix} is the change in internal energy of the system upon mixing, and ΔS_{mix} is the change in entropy of the system upon mixing. The relative importance of the entropic component of the free energy in determining thermodynamic equilibrium is linearly proportional to the temperature. Generally speaking at high temperatures, entropy tends to dominate equilibrium while at lower temperatures the energy term tends to dominate equilibrium.

2.1 The Entropy of Mixing

Within the field of alloy thermodynamics, it is generally assumed that the dominant term in ΔS_{mix} is the change in configurational entropy upon mixing. In reality, the ΔS_{mix} term is more complicated and includes magnetic, electronic, and vibrational components in addition to the configurational term.

$$\Delta S_{mix} = \Delta S_{mix}^{config} + \Delta S_{mix}^{vib} + \Delta S_{mix}^{electronic} + \Delta S_{mix}^{magnetic} \tag{2.8}$$

Although in absolute terms the magnetic, vibrational, and electronic contribution to the entropy of a system are no less important than the configurational entropy, when we consider the **change** in entropy upon mixing of a system of pure metals into a disordered alloy, we expect that the configurational term will dominate the change in entropy of mixing:

$$\Delta S_{mix}^{config} \gg \Delta S_{mix}^{vib} + \Delta S_{mix}^{electronic} + \Delta S_{mix}^{magnetic} \tag{2.9}$$

Therefore, it is reasonable to make the assumption that we can ignore the magnetic, electronic, and vibrational contributions to the change in entropy upon mixing and

approximate this entropy change as being completely attributable to the change in configurational entropy upon mixing:

$$\Delta S_{mix} \approx \Delta S_{mix}^{config} \tag{2.10}$$

Now it has been established that the entropy change upon mixing can be approximated as being purely configurational, we will quantify this change in entropy of mixing. The entropy of a system is given by the Boltzmann entropy formula:

$$S = k_B \ln \Omega \tag{2.11}$$

where k_B is the Boltzmann constant and Ω is the number of possible microstates of the system. For a binary A–B solid solution crystal with N total atoms ($N = N_A + N_B$) the number of distinct microstates is given by

$$\Omega = \frac{N!}{N_A! N_B!} \tag{2.12}$$

and more generally for an alloy with $\mathcal{C}$ components:

$$\Omega = \frac{N!}{\prod_i^{\mathcal{C}} N_i!} \tag{2.13}$$

Applying Equation 2.11 we can write an expression for the entropy of the system as

$$S/k_B = \ln \Omega = \ln \frac{N!}{\prod_i^{\mathcal{C}} N_i!} = \ln N! - \sum_i^{\mathcal{C}} \ln N_i! \tag{2.14}$$

We can apply Stirling's approximation ($\ln m! \approx m \ln m - m$) and substitute $N_i = X_i N$ into the equation above and arrive at the following equation for the configurational entropy in a system with N atoms:

$$S/k_B N = -\sum_i^{\mathcal{C}} X_i \ln X_i \tag{2.15}$$

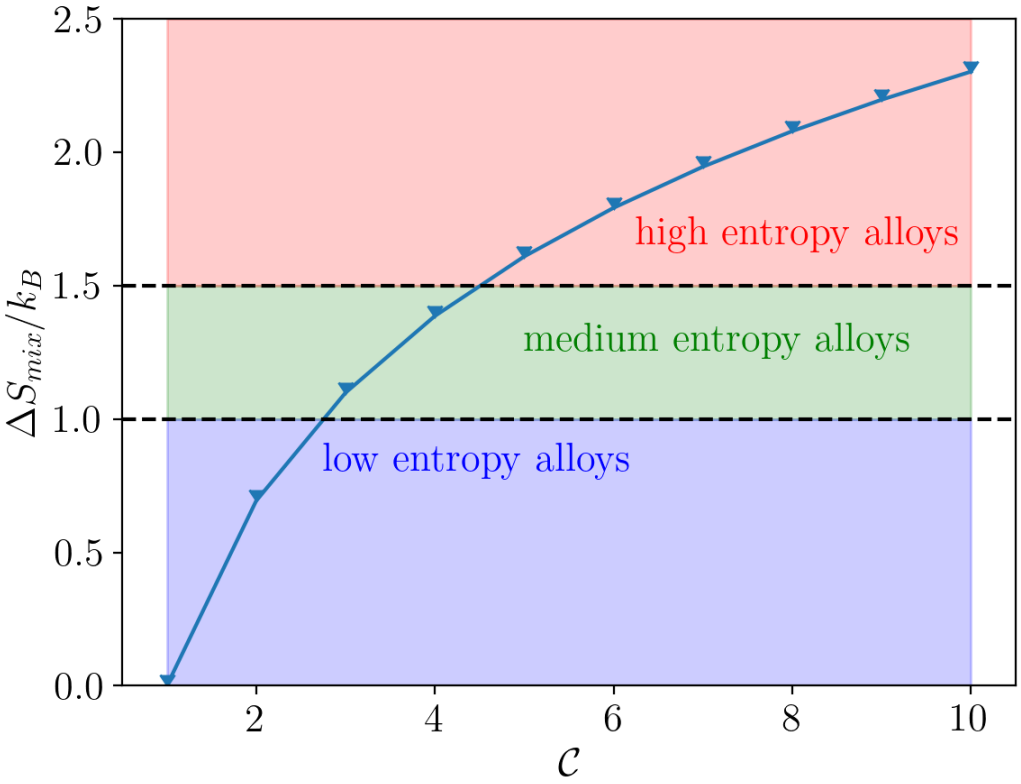

Figure 2-1: Plot of the ideal entropy of mixing ΔS_{mix}^{ideal} for an equimolar solid solution of $\mathcal{C}$ components.

Because pure defect–free metals have zero configurational entropy, the ideal entropy of mixing per atom for an alloy where mixing is completely random is:

$$\Delta S_{mix}^{ideal} = -k_B \sum_{i}^{\mathcal{C}} X_i \ln X_i \tag{2.16}$$

It is worth noting that the case of ideal mixing represents the theoretical upper limit of the increase in configurational entropy upon mixing. Any degree of short–range ordering (SRO) in which some atomic correlation is present at short length scales (distances less than 10 nm) will only serve to decrease the change in entropy upon mixing in the system. But, generally speaking the assumption of random mixing in solid solution alloys is usually considered to be reasonable.

For an alloy system with $\mathcal{C}$ components, the maximum change in entropy upon mixing occurs when all elements have an equal mole fraction: $X_i = 1/\mathcal{C}$. In this case, the ideal entropy of mixing is given by

$$\Delta S_{mix}^{ideal} = -k_B \sum_{i}^{\mathcal{C}} \mathcal{C}^{-1} \ln \mathcal{C}^{-1} = k_B \ln \mathcal{C} \tag{2.17}$$

There is no universal definition of what exactly constitutes an HEA, but can be used to help define HEAs in equimolar solid solutions. A useful definition was given by George, Raabe, and Ritchie [47] who use the ideal entropy of mixing in Equation 2.17 in order to define the entropy classification of an alloy. Solid solution alloys with an ideal entropy of mixing below $1k_B$ (on a per–atom basis) are classified as **low entropy alloys**, while alloys with an ideal entropy of mixing between $1k_B$ and $1.5k_B$ are classified as **medium entropy alloys**, while solid solutions with an ideal entropy of mixing above $1.5k_B$ are HEAs. Examining Figure 2-1, which plots the expression in Equation 2.17, we see that for equimolar systems, binary alloys are low entropy, ternary and quaternary alloys are considered medium entropy, and alloys quinary and above are HEAs. Now that we have addressed and quantified the entropy change in an alloy with random mixing, we will examining existing models for understanding the other component of mixing, namely the energy change ΔU_{mix}.

2.2 The Ideal Solid Solution Model

In an ideal solid solution, it is assumed there is no energy change upon mixing ($\Delta U_{mix}^{ideal} = 0$) and the only driving force for mixing is the change in entropy:

$$\Delta F_{mix}^{ideal} = -T\Delta S_{mix}^{ideal} \tag{2.18}$$

One result of this is that in an ideal solid solution, mixing is always favored ($\Delta F_{mix}^{ideal} < 0$) at non–zero temperature because the ideal entropy of mixing is always positive. For a binary A–B alloy, the ideal solution model assumes that the energy of A–A,

B–B, and A–B bonds are all the same. Clearly the ideal solution model is limited in applicability, but one case in which it does apply is isotopic mixing where different isotopes of the same element are mixed together. Because isotopes of the same element have identical chemical behavior, the only driving force for mixing is entropic.

For the binary A–B solid solution considered here, we can write the free energy of mixing as

$$\Delta F_{mix} = -k_B T \left((1 - X_B) \ln(1 - X_B) + X_B \ln X_B \right) \tag{2.19}$$

Because mixing two elements will always increase the configurational entropy of the system compared to the pure state, in the ideal solid solution model mixing is always favored at non–zero temperature: $\Delta F_{mix}^{ideal} < 0$. In HEAs, an ideal solid solution model is sometimes assumed, in which case single–phase formation would always be favored unless an intermetallic phase between some combination of elements within the HEA could form with a deeply negative enthalpy of formation.

2.3 The Regular Solution Model

The regular solid solution model allows us to account for the fact that there are energetic changes associated with mixing in addition to entropic changes, and we can relax the definiting assumption of the ideal solution model.

$$\Delta U_{mix}^{reg} \neq 0 \tag{2.20}$$

As with the ideal solution model discussed previously, it is assumed that the components of the solid solution are mixed randomly. In the regular solution model, the energy changes associated with mixing are viewed through the lens of pairwise interactions between neighboring atoms. Let us consider a binary alloy A–B, in which A–A bonds have an energy of ϵ_{AA}, B–B bonds have an energy of ϵ_{BB}, and A–B bonds have an energy of ϵ_{AB}. The energy change upon mixing for the alloy system is re-

lated to the energy change caused by the breaking of A–A and B–B bonds and the formation of A–B bonds in the mixed solid solution alloy. A useful parameter ω is typically defined in the literature:

$$\omega_{AB} = \epsilon_{AA} + \epsilon_{BB} - 2\epsilon_{AB} \tag{2.21}$$

where ω_{AB} encapsulates the energy change associated with breaking single A–A and B–B bonds and forming two A–B bonds. For a randomly mixed A–B alloy the energy change associated with mixing can be written as

$$\Delta U_{mix} = z\frac{N_A N_B}{N_A + N_B}\omega_{AB} = zNX_B(1 - X_B)\omega_{AB} \tag{2.22}$$

where z is the coordination number (number of nearest neighbors) in the A–B crystal. The regular solution model is a significantly more realistic improvement over the ideal solid solution model, but the model certainly still has drawbacks. The introduction of solutions with more than two components complicates the regular solution model analysis for several reasons.

First of all, the binary interaction between elements A and B can be parameterized simply with ω_{AB}, but in a more complex solid solution with 3 or more components, a parameter ω_{ij} is required for every possible pair of elements i–j in the alloy. The number of pairwise interaction energies needed to describe alloys with different numbers of elemental components is shown below in Table 2.1.

Table 2.1: Number of ω_{ij} parameters N_ω required to describe a $\mathcal{C}$ component alloy

$\mathcal{C}$	N_ω
2	1
3	3
4	6
5	10

There is an implicit assumption, which can be considered as a mean–field approximation, which assumes that the bond energies ϵ_{AA}, ϵ_{BB}, and ϵ_{AB} are constants and do not vary with composition of the system itself. For example, there is an implicit assumption that the energy of A–A bonds in pure A is the same as the energy of A–A bonds in a binary, equal mixture of A and B. For a binary alloy of chemically similar metals, this assumption might be reasonable but as the compositional complexity of the solid solution increases this assumption could break down.

If the pairwise interaction between atoms depends on the interatomic separation (as with interatomic potentials) it is generally taken as a given that the atoms are separated by the equilibrium distance which minimizes the interaction energy. So it follows that, rigorously speaking, the interaction energy should depend on the lattice parameter of the system and the crystal structure which together determine the nearest–neighbor separation. If A and B are metals with the same crystal structure and similar lattice parameters we would expect the approximation error to be small, but in the case of HEAs it is well known that local lattice distortion (LLD) is significant [48–50], driven by the atomic size mismatch of the components, so there is reason to believe that the mean–field approximation would break down in HEAs.

In addition to the mean–field nature of the regular solution model, it also assumes that the energetics of mixing are completely attributable to bonding interactions between nearest neighbors in a solution. For metals the valence electrons which determine the bonding behavior are delocalized, so it is reasonable to believe that metallic bonding includes the local chemical environment more generally as opposed to solely the nearest neighbor atoms. In order to more accurately account for the mixing energetics in an HEA one would need to include many–body interactions (triplet, quadruplet, etc) out to several coordination shells. In essence this approach amounts to the cluster expansion approach which is discussed in more detail later in this chapter.

2.4 The Quasichemical Solid Solution Model

It is possible to relax the assumption of perfectly random mixing that is taken in the regular solution model. At high temperatures, where the entropic driving force for mixing becomes the dominant component of the free energy of mixing, totally random mixing would be expected. In a system with non–zero mixing energy we would expect that as $T \rightarrow 0$ the energetic component of the free energy becomes more important and a higher degree of short–range ordering would be expected at equilibrium. The relaxation of the assumption that elements are mixed totally randomly results in the quasichemical model. I will briefly summarize the results of the quasichemical model for a binary A–B solid solution following the approach of Guggenheim [51]. The number of A–B bonds is given by N_{AB}. We will define a fraction $\bar{X}$: $N_{AB} = \bar{X}/z$ where N_{AB} is the number of A–B bonds. In the randomly mixed solid solution $\bar{X}$ is:

$$\bar{X} = \frac{N_A + N_B}{N_A N_B} \tag{2.23}$$

Here we utilize the ω A–B bond energy parameter defined previously in Equation 2.21 and define the quasichemical approximation as:

$$\bar{X}^2 = (N_A - \bar{X})(N_B - \bar{X}) \exp\left(-2\omega_{AB}/zk_BT\right) \tag{2.24}$$

Using the substitution $\eta = \exp\left(\omega_{AB}/zk_BT\right)$ we can recast Equation 2.24 as:

$$(N_A - \bar{X})(N_B - \bar{X}) - \eta^2\bar{X}^2 = 0 \tag{2.25}$$

Now defining another quantity β as

$$\bar{X} = \frac{N_A N_B}{N_A + N_B}\frac{2}{\beta + 1} \tag{2.26}$$

so that $\beta = 1$ corresponds to totally random mixing. Now expressing Equation 2.25 as a quadratic equation for β

$$\beta - (1 - 2X_B)^2 = 4\eta^2 X_B(1 - X_B) \tag{2.27}$$

with the solution

$$\beta = \sqrt{1 + 4X_B(1 - X_B)(\eta^2 - 1)} \tag{2.28}$$

The energy change associated with mixing in the quasichemical model is then written as:

$$\Delta U_{mix} = \frac{2}{\beta + 1} X_B(1 - X_B) N\omega_{AB} \tag{2.29}$$

The change in entropy of mixing in the quasichemical model is then:

$$\begin{aligned} -\Delta S_{mix}/k_B &= (1 - X_B)\ln(1 - X_B) + X_B \ln X_B \\ +\frac{1}{2}z\left((1 - X_B)\ln\frac{\beta + 1 - 2X_B}{(1 - X_B)(\beta + 1)} + X_B \ln\frac{\beta - 1 + 2X_B}{X_B(\beta + 1)}\right) \end{aligned} \tag{2.30}$$

So, in a quasichemical solid solution model we can account for non–random mixing driven by non–zero mixing energy characterized by the parameter ω_{AB}.

The quasichemical solid solution model provides an analytical framework to understand non–random mixing in a binary alloy but in practice applying such a model to HEAs is not convenient. A more typical way to capture the non–random mixing in HEAs is through the short–range order (SRO) concept quantified through use of the Warren–Cowley SRO parameter:

$$\alpha_m^{ij} = 1 - \frac{P_m^{ij}}{X_i X_j} \tag{2.31}$$

where P_m^{ij} is the i–j pair probability of the mth neighbor shell. Generally SRO is studied through computational techniques such as hybrid Monte Carlo methods [52] coupled with density–functional theory (DFT) or through the cluster expansion approach [53]. It has been found the SRO is computationally predicted in many

HEAs, but the degree of SRO is highly sensitive to temperature and it is unknown how much slow kinetics may prevent experimental observation of SRO in HEAs, especially refractory HEAs.

2.5 High Entropy Alloy Thermodynamics

The pursuit of understanding the thermodynamic behavior of HEAs is a field of intense focus in the world of materials research [54], and specifically an open and important questions is: what HEA compositions will tend to form a single–phase solid solution (SPSS) which was the original "HEA idea" proposed by Cantor, and which compositions will form a complex, multiphase microstructure? Although this is a simple question, in practice it is a complicated multidimensional global optimization problem. Furthermore, as the number of elemental components increases, the number of phases which can coexist at equilibrium also increases. Figure 2-2 illustrates the set of possible equilibrium structures for a model equiatomic ternary alloy. Although there are certainly advantages to the development of multiphase HEAs, there is a concept that the suppression of the formation of intermetallic phases can prevent embrittlement of the HEA. As the name "high entropy alloy" suggests, the primary focus has been to maximize the entropic driving force for mixing in Equation 2.7 by selecting equimolar or close to equimolar compositions and typically including 5 or more elemental components. Assuming that the system is randomly mixed and that other components of the entropy of mixing (electronic, magnetic, vibrational) can truly be ignored, then it is straightforward to quantify the entropy of mixing with Equation 2.16. The prediction of which crystal structure will tend to form for HEAs is determined through several heuristics which include the valence electron concentration (VEC) [55]. The energetic component of the free energy of mixing in Equation 2.7 is a more challenging quantity to deduce and this will be the purpose of the model I develop in the following chapter. Recent work used the formation energy of possible binary intermetallic compounds in order to screen for HEA single–phase stability [56].

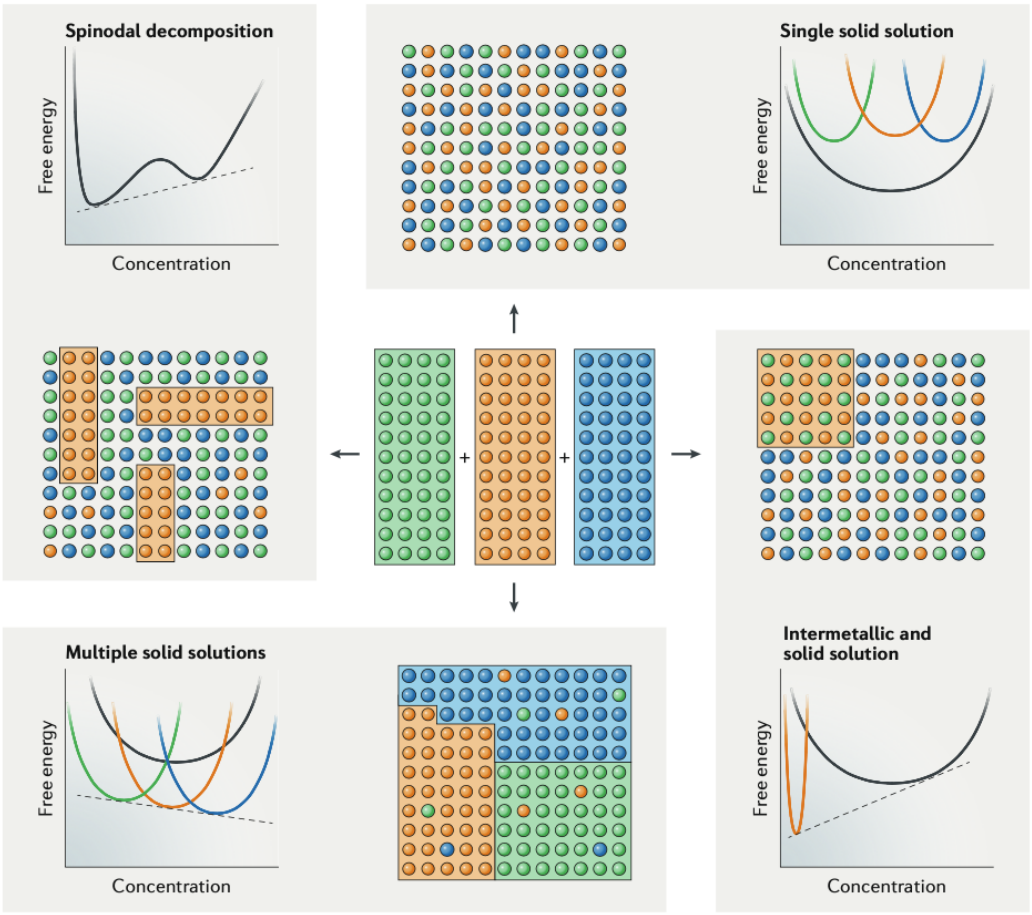

Figure 2-2: Possible equilibrium states schematic as appears in [47]. The possible microstructures which can form in a ternary system are a single–phase solid solution, multiple solid solution phases, spinodal decomposition which occurs when there are to local minima on the same free energy curve, and equilibrium between an intermetallic phase with a "sharp" free energy curve and a solid solution with a "broad" free energy curve.

The Miedema model [57] is the simplest approach to calculating the energy of mixing in HEA systems, and is based on empirical liquid–phase mixing energies and assumes binary interactions between elements as with the regular solution model.

$$\Delta U_{AB}^{mix} = f(X_A, X_B)\left(X_A \Delta U_{\text{A in B}}^{\text{sol}} + X_B \Delta U_{\text{B in A}}^{\text{sol}}\right) \tag{2.32}$$

with

$$f(X_A, X_B) = X_A X_B (1 + \delta X_A X_B) \tag{2.33}$$

where δ accounts for the effective contact area between atoms A and B. The model has been extended to multicomponent system in order to be more applicable to HEA design [58–60]. The drawbacks of the Miedema model are that it treats the mixing energetics as the summation of binary interactions between nearest neighbors and it is semi–empirical in the sense that it depends on the availability of experimental liquid–phase thermodynamic data for all possible binary pairs in a given HEA. Extensions have been developed for the Miedema model to explicitly account for the effects of elastic strain as well as the effect of crystal structure. Typically these binary interactions are summed over all possible binary pairs in the HEA [61]:

$$\Delta H_{mix} = \sum_{j=1} \sum_{i>j} 4\Gamma_{ij} X_i X_j \tag{2.34}$$

where the parameter Γ_{ij} captures the energetic binary interaction between atoms of type i and j from the Miedema model. Although this model works reasonably for predicting miscibility in binary metallic solid solutions, it is an empirically–based model which assumes all energetic interactions between elements are binary in nature and furthermore that the bond energy associated with these interactions have fixed, singular values. A more advanced approach could be taken using computational methods such as classical molecular dynamics (MD) if there were appropriate interatomic potentials such as embedded–atom method (EAM) potentials available for multicomponent solid solutions. Although these are fairly rare, recently some potentials for refractory HEAs have become available within the Interatomic Potentials Repository maintained by the National Institute for Standards and Technology (NIST) [62, 63].

In reality, within metals valence electrons typically are relatively *delocalized*, meaning that the traditional idea of a pairwise bond between atoms is not quite realistic and bonding in metals is more collective in nature. This could include perhaps several shells of nearest neighbor atoms within the collective metallic bond and include many–body interactions. Therefore, it is reasonable to expect that the bond energet-

ics will depend not only on the atomic types within the binary model but on the local chemical environment (LCE) more generally, leading to a spectrum of bond energies rather than a single value as is the case with mean–field models such as the regular solution model discussed previously.

One approach to calculating the thermodynamic behavior of a complex solid solution more accurately is the cluster expansion (CE) approach (also sometimes referred to as the cluster variation method) first developed by Kikuchi in 1951 [64]. In the CE framework an effective Hamiltonian is constructed for a set of atomic clusters (α) and the total energy is an explicit summation over possible nearest neighbor and many–body interactions. The cluster expansion formalism explicitly showing single–atom, pairwise, and three–body interactions is

$$U(\boldsymbol{\sigma}) = \sum_{i} E(\boldsymbol{\sigma}_i) + \sum_{ij} J_{ij}(\boldsymbol{\sigma}_i, \boldsymbol{\sigma}_j) + \sum_{ijk} K_{ijk}(\boldsymbol{\sigma}_i, \boldsymbol{\sigma}_j, \boldsymbol{\sigma}_k) + \dots \tag{2.35}$$

where $\boldsymbol{\sigma}_i$ represents the elemental occupation of site i, and the coefficients E, J, and K are known as the effective cluster interactions (ECI) which are obtained from fitting data from first–principles calculations. The clear advantage of the CE is the rigorous treatment of possible atomic interactions within a solid solution, but the truncation of the CE summation and the selection of included clusters and fitting of the ECI coefficients is data intensive and not always straightforward. Furthermore, as the complexity of the alloy system increases from a binary system, to ternary systems and beyond, the number of ECIs which must be obtained is combinatorial in nature. For example, in a binary BCC Mo–Ta alloy analyzed by cluster expansion techniques, 17 pairwise ECIs (J_{ij}) and 13 triplet ECIs (K_{ijk}) were included in the analysis [52]. For a more complex alloy such as a quinary HEA, many more ECIs would need to be obtained in order to model a single HEA composition. There is no expression for the exact number of ECIs required, but in one CE study of NbMoTaVW 428 ECIs were included in the Hamiltonian [53], while another limited the CE to only pairwise and 3–body interactions and used 120 ECIs [65].

In the following chapter, I develop an atomistic model which proposes the atomistic mixing energy spectrum as a manner in which the energetic driving force for mixing can be quantified and straightforwardly understood, without the need for the development of a full cluster expansion model. I demonstrate how the analysis can be used to determine the relative stability of solid solution alloys as well as determining which elements are most likely to participate in phase decomposition. Pairing this model with modern *ab initio* total energy electronic structure calculations, I analyze a set of relevant HEA compositions and demonstrate how the model can be utilized to screen compositions for likely multiphase microstructure formation as well as design likely single–phase solid solution compositions.

There is a certain implied conceptual framework for imagining the mixing energetics in HEAs which has so far prevailed that I imagine as a "chain link" model, where mixing causes discrete bonds between nearest neighbors to be broken and reformed, with the sum of energy differences associated with the different broken and reformed chain links leading to an overall mixing energy. An alternative, highly simplified view of mixing energetics is proposed here, which dispenses with the assumption of discrete, singular bond energies. I like to think of this framework as a viscous rosin model. Rosin is a natural glue–like material which is a complex mixture of a wide variety of different organic compounds. In my mental model, the "stickiness" of the rosin (which we will imagine is analogous to the mixing energy) depends on the overall composition of the rosin, but also on the local content of the organic molecules at the point of contact. Different elements will "feel" the "stickiness" differently, and the "stickiness" itself will be a function of both the local chemical environment and the overall composition.

In this chapter, I establish the thermodynamic background for HEAs and demonstrate that a realistic description of the mixing energy in HEAs will necessarily account for local interactions beyond just nearest–neighbor interactions as well as the variation

in interatomic separation due to LLD. In the following chapter I develop a model and methodology which facilitates the quantification of the driving force for mixing within an HEA, for each element at each site within an HEA crystal. The result is a spectral description of the distribution of mixing energies for each element within an HEA as opposed to a single–valued mixing energy for the entire HEA material. This novel approach to analyzing the thermodynamics of HEAs is further utilized to understand several refractory HEAs in chapters 4 and 5.

Chapter 3

A First–Principles Model of Mixing in High Entropy Alloys

In this chapter I develop a thermodynamic model which is the first fully–atomistic representation of the mixing energy in HEAs and facilitates the quantification of an element and site–specific mixing energy in solid solution alloys. The key physical insight of the model is that in metal solid solutions such as HEAs, there is a unique chemical potential for each elemental component at each lattice site, as well as a unique vacancy formation energy (equivalent to the vacancy chemical potential) at each site as well. I develop an approach to calculate the chemical potential of all components and vacancy formation energy (VFE) at each site in the solid solution following recent work by Li [66, 67]. Then the energetic driving force for mixing is quantified by finding the *change* in chemical potential for HEA components between the pure elemental state and the solid solution state, which provides a method to compare the different components of the HEA to determine which elements are more (or less) favored to mix into the solid solution. It is assumed that the mixing is random or near–random through the use of Sequential Quasirandom Structure (SQS) supercells to represent the HEA. The calculations are also conducted at zero temperature through first–principles density functional theory (DFT) calculations and magnetic effects are ignored due to the use of non–spin polarized DFT calculations. The model is demonstrated on a widely studied 5–component HEA CrMnFeCoNi, and the accu-

racy and implications of the model are immediately demonstrated on this HEA, while it can be extended to an arbitrary number of elements and composition making this a powerful and widely applicable model for HEAs.

First, I use the vacancy exchange potential as an example of the calculation of atomistic thermodynamic properties in a HEA, and demonstrate why there is a need for development of a new model and calculation methodology to understand thermodynamic behavior in HEAs, including fundamental defect properties such as the vacancy formation energy. After developing the model later in this chapter and demonstrating its application to CrMnFeCoNi, in the following 2 chapters this model is used to analyze several 5–component equimolar HEAs in the refractory HEA family and demonstrate how this model can be utilized to intuitively design thermodynamically stable solid solutions.

3.1 The Vacancy Formation Energy

The vacancy formation energy is a fundamental property materials and plays in important role in a variety of phenomena such as solid state diffusion and radiation damage. The vacancy formation energy of pure metals and can be easily calculated using DFT methods. Consider a pure system of an arbitrary metal that we will call A, containing N atoms and having an energy of U_{pure}. Consider the removal of an atom from the system, leaving $N-1$ atoms remaining and a single vacancy in the system. The energy of the system with a vacant site is denoted as U_{v}. We can write the energy change as

$$\mathrm{d}U = U_{\text{v}} - U_A^{\text{pure}} = E_{\text{v}}^f - \mu_A = E_{\text{v}}^f - \frac{U_A^{\text{pure}}}{N} \tag{3.1}$$

where μ_A is the chemical potential of A. The chemical potential of A is the partial derivative of the free energy of the system with respect to the number of A atoms

and can be expressed as:

$$\mu_i = \left.\frac{\partial F}{\partial N_i}\right|_{N_{j\neq i},T,V} \tag{3.2}$$

In pure A at zero temperature where $F = U$, the chemical potential is simply: $\mu_A = U_{\text{pure}}/N$. The vacancy formation energy E_{v}^f, which is equivalent to the vacancy chemical potential at zero temperature, can be calculated through the following equation:

$$E_{\text{v}}^f = U\text{v} - \frac{N-1}{N}U^{\text{pure}} \tag{3.3}$$

Using this expression coupled with first–principles calculations allows for the computation of the vacancy formation energy in pure metals. Applying this same procedure and expression to a complex solid solution yields valuable information but not the vacancy formation energy.

3.2 The Vacancy Exchange Potential

Assume we have a solid solution material represented by an SQS supercell (see section A.1 for more information about SQS) with N_{SQS} total atoms. We calculate the energy of the defect–free supercell U_{SQS} as well as the energy of the supercell with an atom missing at each site j U_{v}^j. If one applies the expression in Equation 3.3 in an attempt to calculate the vacancy formation energy at each site in the SQS, some questionable behavior arises. First of all, the calculated value of the vacancy formation energy depends on the element which was occupying the site within the pristine SQS. Second, for certain elements in certain materials, the apparent vacancy formation energy is negative. A negative vacancy formation energy appears to be a somewhat unphysical result as that would make the vacancy formation process spontaneous at zero temperature and would cause the equilibrium vacancy concentration to be extremely high. Furthermore, one would expect that the vacancy formation energy should depend on the elemental species surrounding the vacant site, but not on the "ghost atom" which occupied the site within the pristine SQS. The application of Equation 3.3 to solid solution crystals is not the correct approach, and I coin this

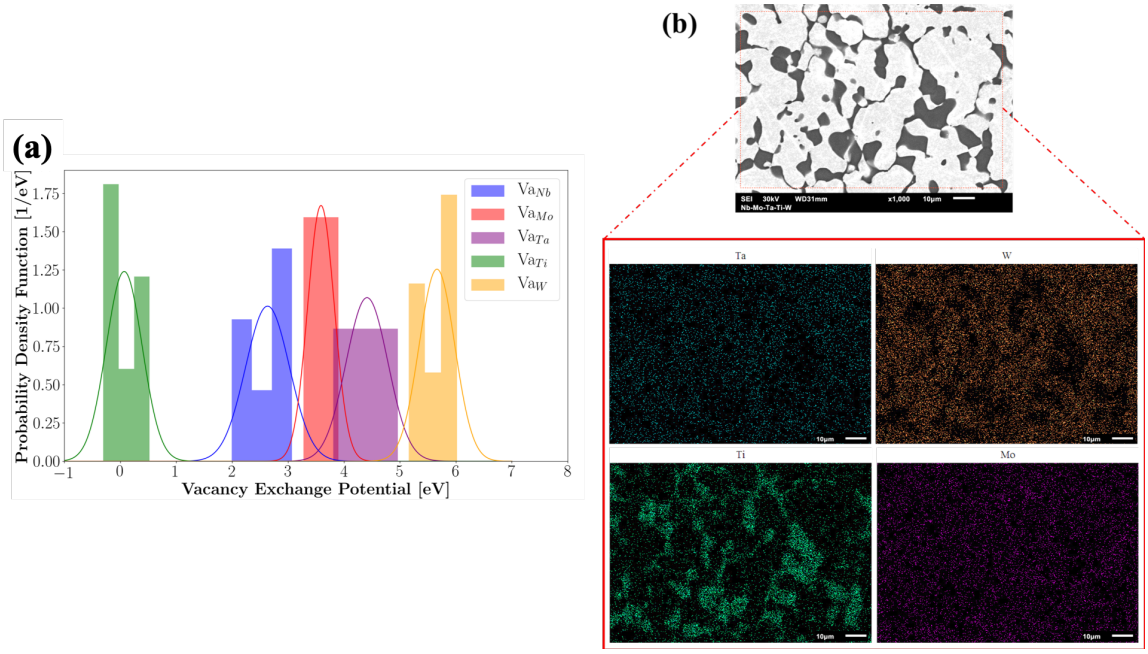

Figure 3-1: (a) The vacancy exchange potential distribution for 30–atom NbMoTaTiW SQS. Note that several Ti sites have a negative vacancy exchange potential. (b) SEM image of NbMoTaTiW as–cast microstructure (as appears in [68]) with corresponding EDX maps demonstrating a distinct bright phase rich in W and a dark phase rich in Ti.

quantity as the vacancy exchange potential instead of the vacancy formation energy:

$$\tilde{\mu}_{\mathrm{v}}^{j} = U_{\mathrm{v}}^{j} - \frac{N_{SQS}-1}{N_{SQS}} U_{SQS} \tag{3.4}$$

Although the vacancy exchange potential is distinct from the vacancy formation energy, there is still valuable physical insight to be gained from this quantity. A vacancy exchange potential analysis of a 30–atom NbMoTaTiW SQS is shown in Figure 3-1 along with the as–cast microstructure of the NbMoTaTiW HEA synthesized by arc melting. It appears that there is some correlation between the negative vacancy exchange potential and the inherent instability of Ti in the equimolar HEA. Another vacancy exchange potential analysis of NbMoTaTiW, for a 125–atom SQS supercell, is plotted in section A.2. This demonstrates the general behavior is essentially the same in the much larger 125–atom SQS, both confirming the results of the smaller analysis while also indicating that results on relatively smaller SQS supercells which

are less computationally intensive to analyze are still valid. That being said, one significant advantage of the larger supercell is the overall sampling of more possible local atomic configurations leading to more accurate distributions.

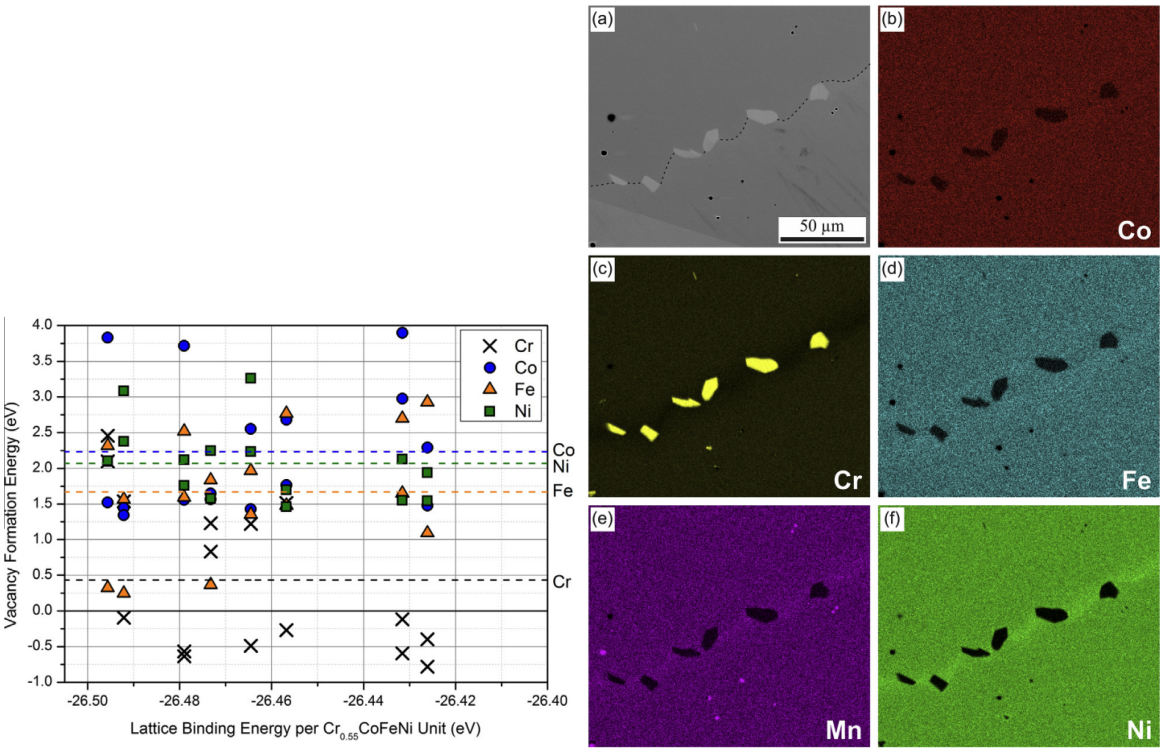

Figure 3-2: (top) Vacancy formation energies (VFEs) for the $Cr_{0.55}CoFeNi$ solid solution system reported by Middleburgh [69]. Note that many of the reported VFEs for Cr are negative. (bottom) SEM EDX of Cantor alloy [70]

In Figure 3.2 on the left side we can see the reported vacancy formation energy from a 2014 study [69] on the CrCoFeNi solid solution system. They report for the different elements significantly different vacancy formation energies, with many of the Cr vacancy formation energies reported as negative. We must assume that the vacancy formation energy reported is what I coin here as the vacancy exchange potential. On the right of Figure 3.2 we see the reported experimental results relating to the widely studied Cantor alloy CrMnFeCoNi, which demonstrate that this HEA does not for a single–phase solid solution but in fact Cr preferentially precipitates as a secondary phase [70]. Although the system studied by Middleburgh *et al* [69]

was $Cr_{0.55}CoFeNi$, so specifically a medium entropy Cantor alloy derivative, we see that again a negative vacancy exchange potential for a particular element within the Cantor HEA corresponds to phase separation of that element.

In this section, I develop the concept of a vacancy exchange potential as a quantity which is easily confused with the vacancy formation energy and show how the vacancy exchange potential can be used to gain insight to the thermodynamic behavior of HEAs. In the following section I develop a thermodynamic model and computational approach to accurately solve for the chemical potential of each element in the HEA along with the vacancy formation energy.

3.3 An Atomistic Model for Mixing in High Entropy Alloys

We will start by considering the vacancy formation process described in the previous section. For a solid solution where site j is occupied by an atom of type A, we can write the total change in energy associated with removing the A atom and creating a vacancy at site j as:

$$\Delta U^j_{A\to \mathrm{v}} = U^j_{\mathrm{v}} - U_{SQS} = \mu^j_{\mathrm{v}} - \mu^j_A \tag{3.5}$$

where the vacancy chemical potential at site j, μ^j_{v}, is equivalent to the vacancy formation energy at site j and μ^j_A is the chemical potential of element A at site j within the HEA supercell. While attaining this chemical potential value in a pure material is trivial, that is not the case in a solid solution and often the mistake is made of implicitly assuming $\mu^j_A = U_{SQS}/N$ or that $\mu^j_A = \mu^{\mathrm{pure}}_A$. Not only is it reasonable to expect that the chemical potential of a given element will be different in the HEA than in the pure material, but furthermore it seems likely that in fact there will be a *distribution* of chemical potentials at each site within the HEA SQS. Although, as I will demonstrate, it is possible to determine the chemical potential of each element

at every site in the SQS, it is much more straightforward to calculate *differences* in chemical potential between different elements at the various sites in the SQS. Consider an equiatomic SQS with $\mathcal{C}$ components, and N_{SQS} total atoms. Now consider site j in the SQS occupied by an atom of type A with a chemical potential of μ_A^j. If the atom type i is swapped to an atom of type B (note that the composition of the SQS has now changed and it is no longer equiatomic), the change in energy associated with this swap can be expressed as

$$\mathrm{d}U = \sum_i \mu_i \mathrm{d}N_i = \mu_B^j - \mu_A^j \tag{3.6}$$

Therefore, performing the atomic swap operations and calculating the corresponding difference in total energy gives relevant information about differences in chemical potential between elements involved in the swap at each site in the SQS. We can define this as the A to B swap energy at site j, which allows us to relate the chemical potential differences between elements at the same site:

$$\Delta U_{A\to B}^j = \mu_B^j - \mu_A^j = U_{A\to B}^j - U_{SQS} \tag{3.7}$$

where U_{SQS} is the total energy of the pristine equimolar SQS. There are $\mathcal{C}-1$ different atomic swap operations that are possible at each site in the SQS, and then an additional vacancy formation operation associated with the removal of the atom from the site without any corresponding replacement. This gives a system of $\mathcal{C}$ unique energy differences which can be calculated, with $\mathcal{C}+1$ independent variables, the set of $\mathcal{C}$ chemical potentials along with the vacancy formation energy at that site. In order to develop a system of linear equations which will facilitate the calculation of the chemical potential of all components of the system, we can use the following energy balance applied to each site within the SQS:

$$\sum_i^{\mathcal{C}} \mu_i^j N_i = U_{SQS} \tag{3.8}$$

For example, we can write for a quinary A–B–C–D–E SQS:

$$N_A\mu_A^j + N_B\mu_B^j + N_C\mu_C^j + N_D\mu_D^j + N_E\mu_E^j = U_{SQS} \tag{3.9}$$

In essence, this energy balance applied to each site in the SQS allows us to account for the pristine, equimolar SQS reference state and completes the system of equations needed to calculate the chemical potential of each element within the HEA.

3.3.1 The Swap Matrix

In order to facilitate the efficient solution of the system of linear equations developed in the previous section, here I develop a construct I will refer to as the swap matrix. The swap matrix encapsulates the compositional change of the system by the set of swap operations that are conducted on each site in the SQS. By constructing the swap matrix, and calculating several energies and energy changes, we can solve the matrix equation

$$\mathbf{S}\boldsymbol{\mu} = \mathbf{E} \tag{3.10}$$

in order to determine the vector of chemical potentials for each component of the system. On the right-hand side of the expression is $\mathbf{E}$, a column vector of energy differences that we will refer to as the exchange matrix. The general concept is that each row of the swap matrix $\mathbf{S}$ represents a separate compositional state of the system. Each row, or compositional state, corresponds to a specific swapping operation. The swap matrix is then multiplied by a vector containing the chemical potential of each component of the HEA, as well as the chemical potential of the vacancy, which can be considered as equivalent to the vacancy formation energy for that site in the HEA. This matrix multiplication is then equal to a vector of energies, or energy differences, corresponding to the swap operations carried out at the site. Finally, the bottom row of the swap matrix corresponds to the site–wise energy balance enumerated in Equation 3.8.

Consider the swap matrix at site k, occupied by an atom of i within the pristine SQS. The swap of type i to type j is represented through the following elements of the swap matrix:

$$\begin{aligned} S_{ji} &= \mathrm{d}N_i = -1 \\ S_{jj} &= \mathrm{d}N_j = +1 \end{aligned} \tag{3.11}$$

Where the first index (row position) corresponds to the swap, and the second index (column position) corresponds to the atomic types participating in the swap. All of the other swap matrix elements in row j are equal to 0. Because a swap of i to i results in no change to the composition or energy of the system, the swap matrix elements $S_{ii} = 0$ and in fact every element within row i of the swap matrix is equal to zero. Row $\mathcal{C} + 1$ of the swap matrix corresponds to the vacancy swap:

$$\begin{aligned} S_{(\mathcal{C}+1)i} &= -1 \\ S_{(\mathcal{C}+1)(\mathcal{C}+1)} &= +1 \end{aligned} \tag{3.12}$$

And the final, bottom row of the swap matrix contains the number of atoms of the different elements in the system:

$$S_{(\mathcal{C}+2)i} = N_i \tag{3.13}$$

for all elemental components i in the HEA. The matrix element on the last row corresponding to the vacancy will be zero as there are no vacancies in the pristine system:

$$S_{(\mathcal{C}+2)(\mathcal{C}+1)} = 0 \tag{3.14}$$

The corresponding element in the exchange vector simply equals the energy of the pristine SQS: $E_{\mathcal{C}+2} = U_{SQS}$. This matrix equation can be solved for each site in a crystal in order to give chemical potentials for each element in the system at every

site, as well as the unique vacancy formation energy for each site in the system.

$$\boldsymbol{\mu}^j = \begin{bmatrix} \mu_1^j \\ \vdots \\ \mu_{\mathcal{C}}^j \\ \mu_{\mathrm{v}}^j \end{bmatrix} \tag{3.15}$$

The general chemical potential vector for site j, $\boldsymbol{\mu}^j$, is shown above. The general form of the exchange vector $\mathbf{E}$ is

$$\mathbf{E} = \begin{bmatrix} \Delta U_{i\to 1} \\ \vdots \\ \Delta U_{i\to \mathcal{C}} \\ \Delta U_{i\to \mathrm{v}} \\ U_{pristine} \end{bmatrix} \tag{3.16}$$

where all of the energy differences contained within $\mathbf{E}$ are obtained through first–principles calculations.

To make clear how this construct is used practically to analyze the thermodynamics of HEAs, I will present an illustrative example. Consider a 125–atom, 5–component equiatomic HEA, and we will analyze the swap matrix for atom of type 2 occupying a given site within the pristine SQS. The swap matrix corresponding to the analysis of this site will be the following:

$$\mathbf{S} = \begin{bmatrix} 1 & -1 & 0 & 0 & 0 & 0 \\ 0 & 0 & 0 & 0 & 0 & 0 \\ 0 & -1 & 1 & 0 & 0 & 0 \\ 0 & -1 & 0 & 1 & 0 & 0 \\ 0 & -1 & 0 & 0 & 1 & 0 \\ 0 & -1 & 0 & 0 & 0 & 1 \\ 25 & 25 & 25 & 25 & 25 & 0 \end{bmatrix} \tag{3.17}$$

The corresponding exchange vector will then be:

$$\mathbf{E} = \begin{bmatrix} \Delta U_{2\to 1} \\ 0 \\ \Delta U_{2\to 3} \\ \Delta U_{2\to 4} \\ \Delta U_{2\to 5} \\ \Delta U_{2\to \mathrm{v}} \\ U_{pristine} \end{bmatrix} \tag{3.18}$$

Then, by solving the matrix equation $\mathbf{S}\boldsymbol{\mu} = \mathbf{E}$, the vector of chemical potentials can be determined. While the chemical potential of each element is useful information, and the vacancy chemical potential allows us to correctly determine the vacancy formation energy in solid solutions, a further refinement must be made in order to compare thermodynamic behavior across the different elements within the HEA. The value that is most useful in characterizing this behavior is the *change* in chemical potential associated with mixing. This quantity, which I coin as the "atomistic mixing energy" is formulated as:

$$\Delta\mu_i^{\mathrm{mix}} = \mu_i^{\mathrm{HEA}} - \mu_i^{\mathrm{pure}} \tag{3.19}$$

The atomistic mixing energy can be used to understand the inherent energetic driving force for mixing of each element in a solid solution. Furthermore, this quantity allows us to understand the distribution of this driving force for each component across all sites (and the local chemical environment surround those sites) within the simulation cell. When $\Delta\mu_{mix}^i > 0$, the mixing process for element i is thermodynamically disfavored while when $\Delta\mu_{mix}^i < 0$ mixing is favored. This gives us a new, straightforward way to quantify and understand the thermodynamic behavior of HEAs at an atomistic, element–specific level.

3.3.2 Case Study: Cantor Alloy CrMnFeCoNi

In order to demonstrate the application of this atomistic mixing energy (AME) model, I will begin by exploring the Cantor alloy. The Cantor alloy is generally considered the most widely studied and broadly known HEA, with an equimolar composition of five 3*d* top row transition metals: CrMnFeCoNi. These five elements are all next to each other within the periodic table, and the Cantor alloy has been found to take a face–centered cubic (FCC) crystal structure.

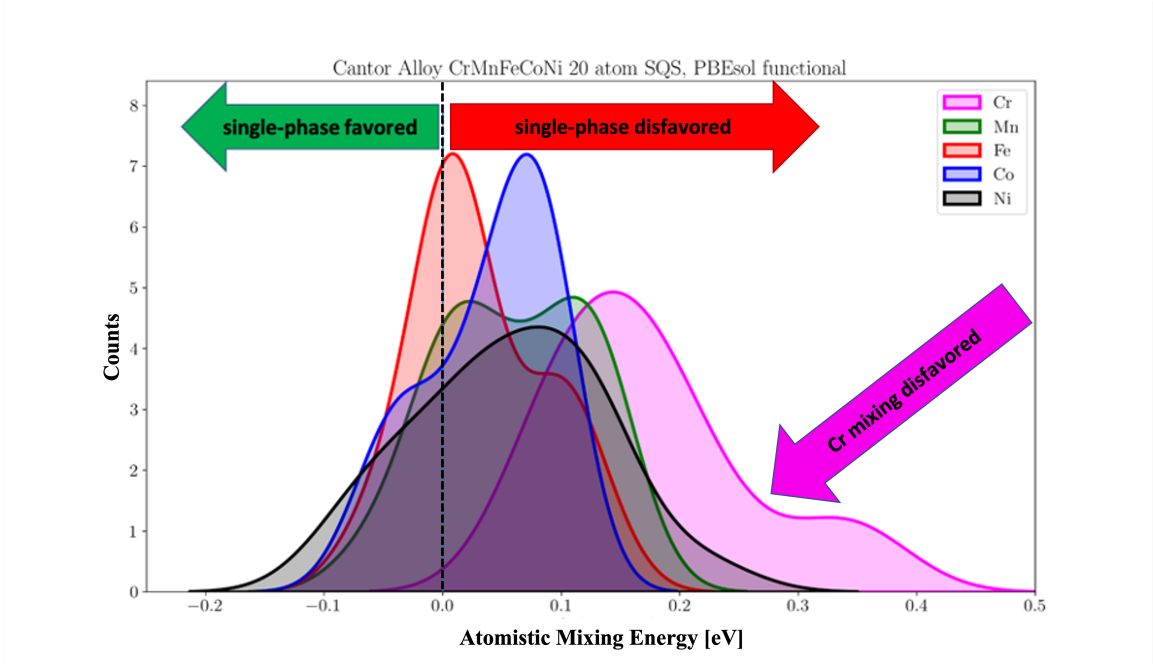

Figure 3-3: The atomistic mixing energy spectrum for Cantor alloy CrMnFeCoNi

The Cantor alloy was modeled by use of a 20–atom FCC SQS, with the atomistic mixing energy results plotted above in Figure 3-3. One initial impression that can be made is that for the Cantor alloy, generally it appears that most sites for most elements have actually a positive atomistic mixing energy indicating that formation of a single–phase is not favored. Examining the results more closely, we see that Cr has the highest atomistic mixing energy and essentially all sites in the SQS have a positive mixing energy for Cr. From this, we can conclude that Cr is the least stable element within the Cantor alloy. Then, it appears that Ni and Mn are the next least

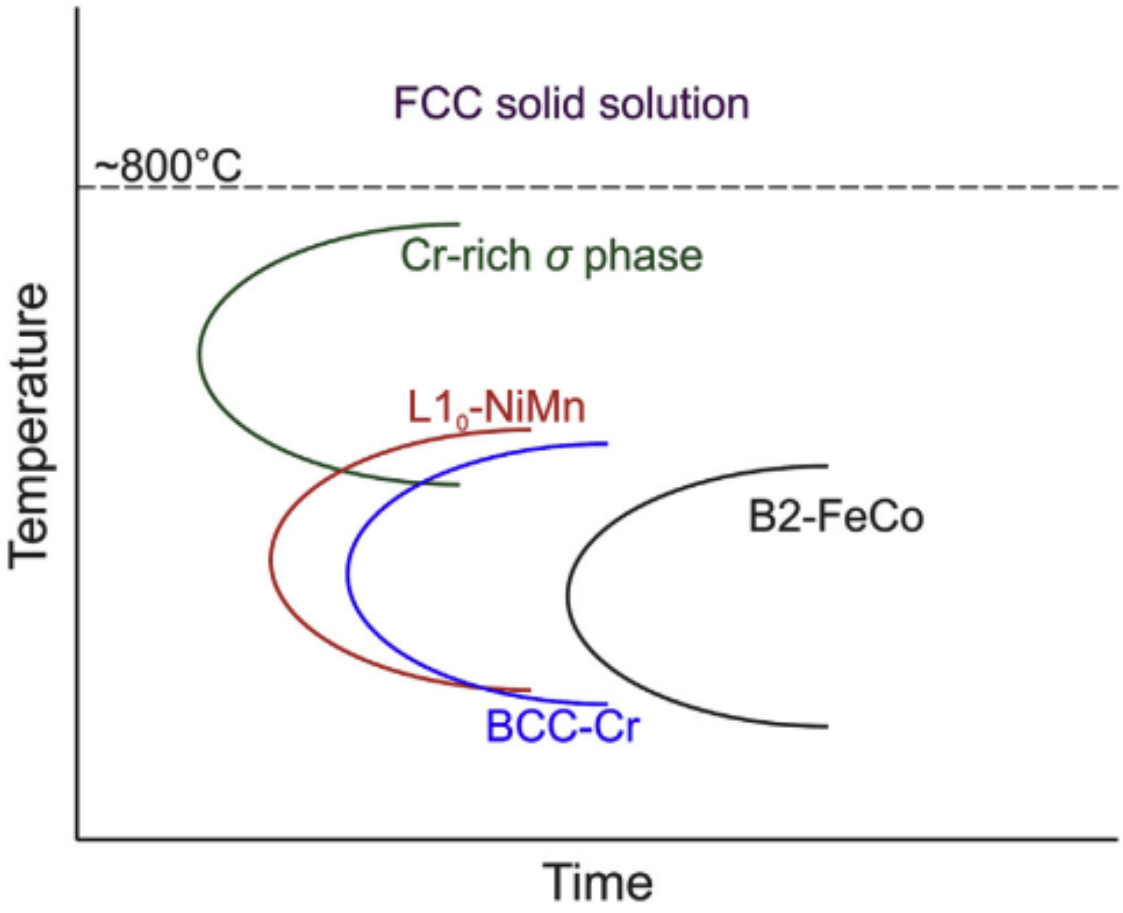

Figure 3-4: Hypothetical TTT diagram of CrMnFeCoNi based on experimental evidence [70]

stable elements in the alloy, followed by Fe and Co. Based on the understanding that can be obtained from the model that I have developed, we can conclude that the model indicates inherent instability of the FCC CrMnFeCoNi HEA with preferential phase separation of Cr, followed by Ni and Mn being the next most likely elements to phase separate. It is notable that the CrMnFeCoNi HEA is considered as the canonical HEA, yet the atomistic thermodynamic model developed in this thesis indicates that this most–studied HEA in fact is inherently unstable.

Although the Cantor alloy has previously been found to form a single phase, it has been demonstrated experimentally that the Cantor alloy eventually undergoes phase

decomposition at high temperatures [70], with Cr precipitating out as a Cr–rich σ–phase as seen on the right side of Figure 3.2. So, on the basis of Cr being the most inherently unstable element within the Cantor alloy, it appears that the atomistic mixing energy analysis matches well with experimental observation. Shown above in Figure 3-4 is a hypothesized schematic time–temperature–transformation (TTT) diagram of the Cantor alloy system [70]. The schematic TTT diagram which shows that although Cr precipitates out first, eventually Ni and Mn precipitate out as a $L1_0$ ordered intermetallic phase, followed by Fe and Co eventually forming a $B2$ structure intermetallic phase. So, this is futher evidence of the inherent instability of Cantor alloy predicted by the atomistic mixing energy and demonstrates agreement between the elemental trends in the atomistic mixing energy as well.

In this chapter, I introduce the concept of the vacancy exchange potential as a quantity which is often mistaken for the vacancy formation energy within the literature. I demonstrate how this quantity can be used to gather valuable information about the thermodynamic stability of HEAs, namely the presence of a negative vacancy exchange potential for a given element indicates that element is unstable within the system and will tend to precipitate out. This is demonstrated through my own computational and experimental analysis of the NbMoTaTiW system, as well as through other data reported in the literature. Then, I further develop the model and propose a methodology which allows for the calculation of the distribution of the chemical potentials of all elements within the HEA across all sites, in addition to the correct vacancy formation energy. Then, I use these chemical potentials to formulate a quantity I coin as the atomistic mixing energy which allows for the quantification of the energetic driving force for mixing in an element and site–specific manner within any HEA. In the following two chapters, I apply this model to a variety of refractory HEAs as well as experimentally synthesizing and characterizing these materials in order to test the validity of the model and gain further insight into the thermodynamic behavior of these important but relatively little–studied HEAs.

Chapter 4

NbMoTa–AB High Entropy Alloy System

In this chapter, I will present the computational and experimental results of this thesis concerning several refractory HEAs that all share the same Nb–Mo–Ta ternary base, but are 5–component equiatomic HEAs. Nb, Mo, and Ta all take the BCC crystal structure as the stable phase at zero temperature for these pure elements, so a simplistic rationale suggests starting with these elements should provide a reasonable starting point for developing a single–phase BCC alloy. In this chapter I show the results of atomistic simulations based on the model developed in chapter 3, including the atomistic mixing energy and vacancy formation energy, for 4 quinary HEAs: NbMoTaTiW, NbMoTaTiV, NbMoTaTiZr, and NbMoTaHfW. For the purposes of atomistic simulation, all HEAs in this chapter are modeled as BCC solid solutions. The vacancy formation energy is of particular importance in the context of HEAs due to the effect of increasing stabilization of vacancies in HEAs predicted by Wang *et al.* [71], which correspondingly makes the formation energy itself a very important parameter in the overall equilibrium vacancy concentration. In addition to analysis of these materials by atomistic simulation, the equimolar compositions were also synthesized at the laboratory–scale by the electric arc melting approach as described in more detail in section B.1.

Previous studies have been conducted on similarly composed HEAs, namely the NbMoTaVW system [72], in which all 5 components of the HEA are BCC at zero temperature, and found a very high strength for the alloy. Efforts have been made to compose refractory HEAs which are intrinsically ductile, as determined by the tendency to shear vs. clever in tension. Previous researchers have claimed to tailor the intrinsic ductility through control of the valence electron concentration (VEC) [73].

Other researchers have previously sought to develop a system to predict which HEA compositions will tend to form a single–phase HEA including King *et al.* [74, 75] along with Troparevsky *et al.* [56]. The model by King *et al.* is based on the use of the Miedema model to predict the mixing energy of the solid solution phase, and compares this mixing energy against the formation energy of possible binary intermetallics formed between the HEA components to predict which compositions will form a single–phase HEA. The model developed by Troparevsky *et al.* ignores the mixing energy of the solid solution and uses the formation energy of possible intermetallics compared to the entropic driving force for mixing to predict which HEA compositions will form a single–phase HEA. The results reported by Troparevsky *et al.* indicate a single–phase HEA microstructure predicted for NbMoTaTiW, NbMoTaTiV, NbMoTaTiZr and a multi–phase microstructure for NbMoTaHfW. Furthermore, the model by Troparevsky *et al.* also predicts a single–phase microstructure for CrMnFeCoNi. In the previous chapter I demonstrate that the atomistic model developed in this work predicts a multiphase microstructure for CrMnFeCoNi with Cr preferentially separating into a different phase, which is confirmed by experiments. In this chapter I will further demonstrate the atomistic model developed in this work is more effective in predicting phase stability in NbMoTa–base refractory HEAs as well.

4.1 NbMoTaTiW

I will begin by examining the NbMoTaTiW HEA discussed in the previous chapter. The distribution of atomistic mixing energies for each element within the HEA across

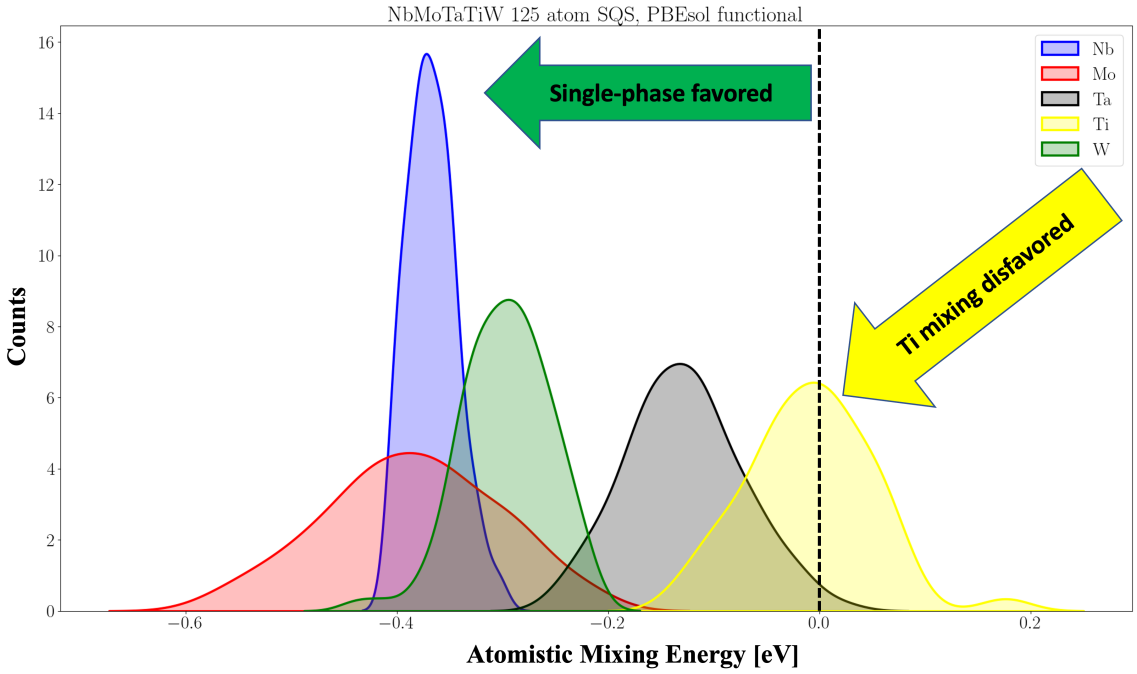

Figure 4-1: Atomistic mixing energy distribution for NbMoTaTiW 125-atom SQS.

all sites is shown in Figure 4-1. We see that in this case the mixing energy for Ti across many sites is positive and the peak of the distribution roughly zero. Therefore we expect that Ti is fundamentally unstable in NbMoTaTiW, which is in good agreement with the results shown Figure 3-1. Aside from Ti, the other elements generally have negative atomistic mixing energies, with Ta having perhaps some small fraction of positive atomistic mixing energy sites within the SQS. The components in order from highest mean AME to lowest are: Ti, Ta, W, Nb, Mo. It is noteworthy that the distribution for Nb is particularly narrow while the AME distribution for Mo is particularly broad. Qualitatively, we can interpret this as meaning that the Mo atomistic mixing energy is much more sensitive to the local chemical environment than Nb.

Along with the AME distribution, the vacancy formation energy of NbMoTaTiW was also calculated for each site within the SQS. A histogram of vacancy formation energies is shown in Figure 4-2. Within the NbMoTaTiW 125–atom SQS, the vacancy formation energy ranges from $\sim$ 2.6 eV up to 4.25 eV, with a peak in the distribution around 3.4 eV. It is worth noting that in a HEA at equilibrium, not all of the sites

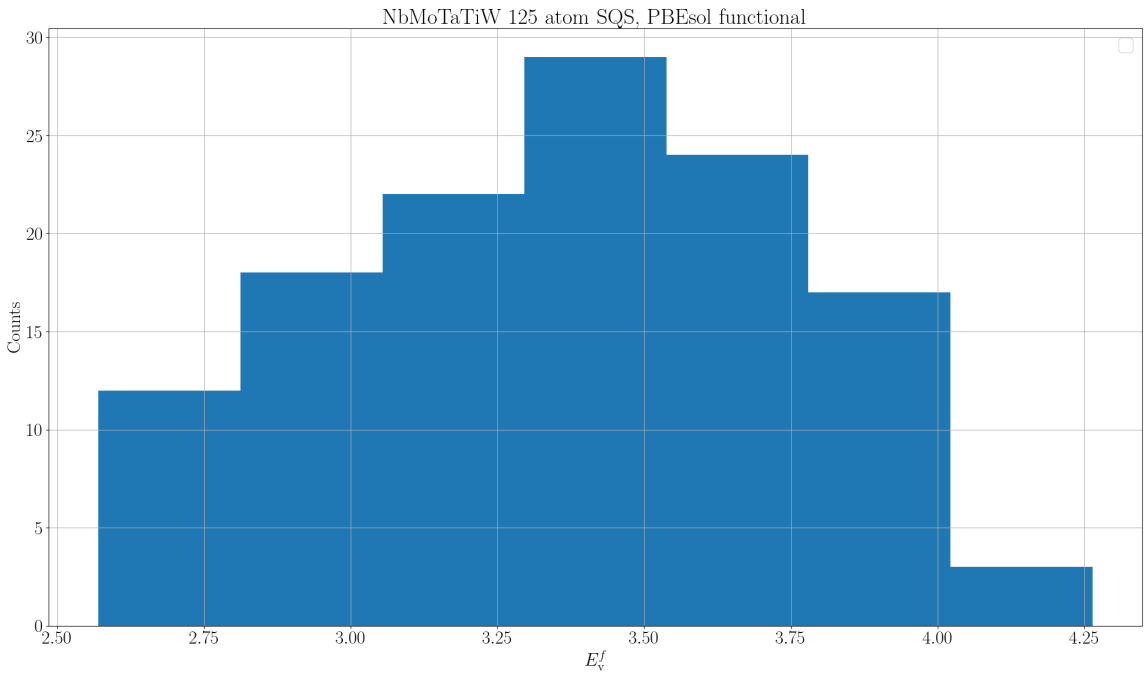

Figure 4-2: The distribution of vacancy formation energies in a 125–atom NbMoTaTiW BCC SQS.

reported here would be represented in the physical material. Specifically, at lower temperatures the low–energy vacancy sites will be strongly preferred and would be observed much more frequently than the higher energy vacancy sites.

The vacancy formation energy of the pure elements calculated by first–principles methods is reported as:

Table 4.1: Reported vacancy formation energies for pure element components of NbMoTaTiW [76]

element	0 K structure	E_v^f [eV]
Nb	BCC	2.94
Mo	BCC	2.90
Ta	BCC	3.12
Ti	HCP	2.07
W	BCC	3.27

The rule–of–mixing average for the vacancy formation energy of the elemental components which compose the HEA is 2.86 eV. It is notable that the vacancy formation energy distribution is skewed towards higher energies, and the high energy tail of the distribution goes well past the highest elemental vacancy formation energy.

4.1.1 As–Cast Microstructure

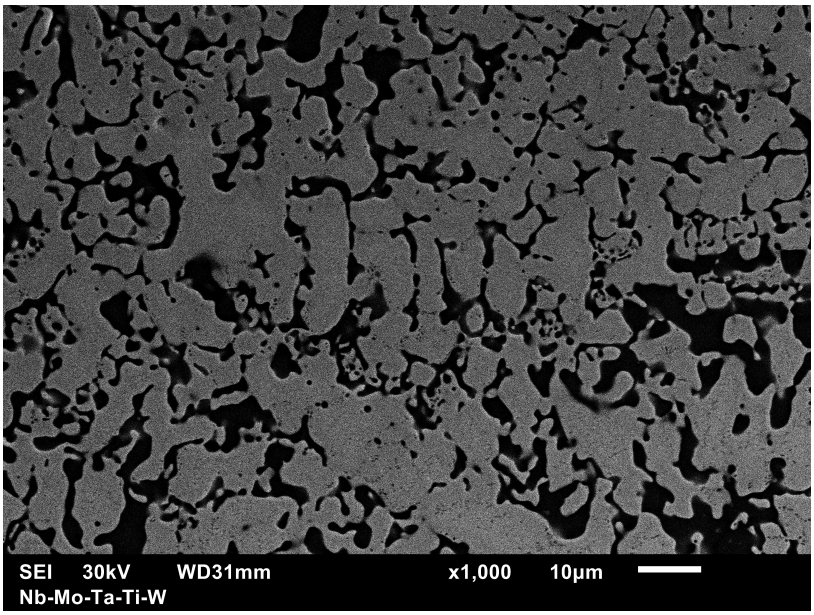

Figure 4-3: A SEM image of as–cast NbMoTaTiW showing distinct light and dark regions.

An SEM image of the as–cast microstructure of NbMoTaTiW is shown in Figure 4-3 demonstrating two distinct region, one which appears dark/black in the SEM image and another that appears as light gray. Given the SEM/EDX analysis of NbMoTaTiW shown previously in Figure 3-1(b), we can see that this dark phase is very enriched in Ti while the lighter phase appears to be somewhat enriched in W. A powder X–ray diffraction (XRD) pattern for the as–cast NbMoTaTiW is shown in Figure 4-4 demonstrating distinct BCC and HCP patterns present in the diffraction pattern for the material. This indicates that NbMoTaTiW forms a dual–phase microstructure with W–rich BCC phase in coexistence with a Ti-rich HCP phase.

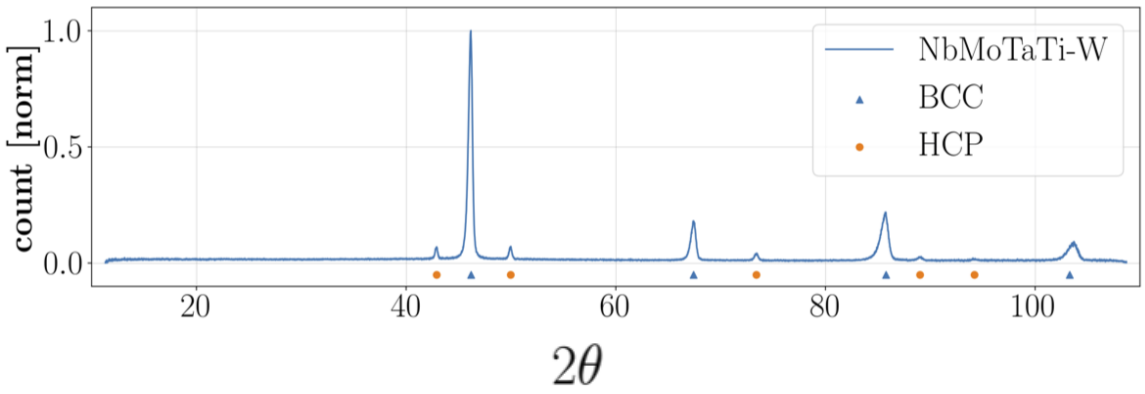

Figure 4-4: The powder X–ray diffraction pattern obtained from the as–cast NbMoTaTiW HEA. The pattern shows superimposed BCC and HCP patterns indicating a dual–phase BCC/HCP microstructure.

4.2 NbMoTaTiV

The NbMoTaTiV system was analyzed by the atomistic mixing energy approach described in the previous chapter is shown in Figure 4-5. We see that for the case of NbMoTaTiV mixing is energetically favored for all components, and the elements ordered from least negative AME (least driving force for mixing) to most negative AME are: V, Ti, Ta, Nb, and Mo. Again, similar to the case of NbMoTaTiW, Nb has a narrow AME distribution while Mo has a relatively broad distribution. This indicates that in NbMoTaTiV, just as in NbMoTaTiW, it appears that Nb is relatively less sensitive to the local chemical environment while Mo is more sensitive to the local chemical environment. We can view these sensitivities as being connect qualitatively to the propensity for short range ordering. Since Mo is more sensitive to the local chemical environment, there will be a larger driving force for short range ordering of Mo from higher energy local atomic configurations to lower energy local atomic configurations.

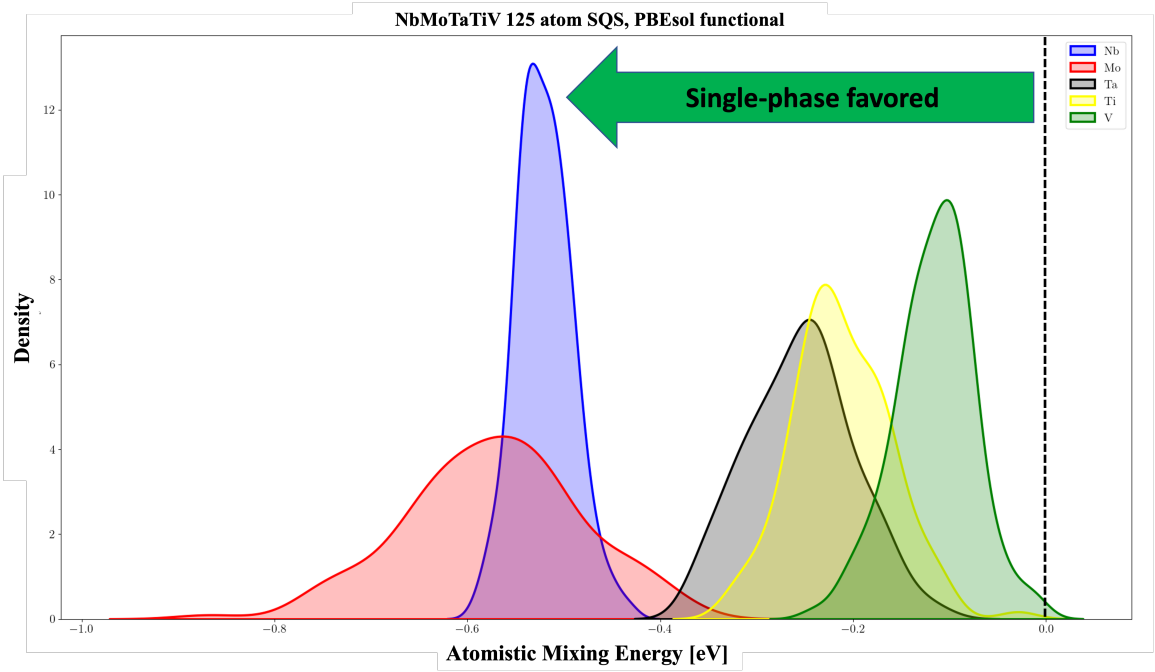

Figure 4-5: The calculated AME spectrum for BCC NbMoTaTiV. Note that all elements have a negative distribution of AME values, with Ti and V being the least negative elements in the solid solution.

The vacancy formation energy distribution for the 125–atom NbMoTaTiV SQS is shown in Figure 4-6. The distribution of vacancy formation energies has a distinctive low–energy tail beginning at approximately 1.5 eV but otherwise is a relatively symmetric distribution. These low vacancy formation energy sites are the most likely to be activated at low temperatures and can be considered as likely trap sites for vacancy point defects in a material, in which it is reasonable to suspect that isolated vacancies will have a smaller driving force for vacancy–interstitial annihilation or agglomeration into vacancy–cluster defects.

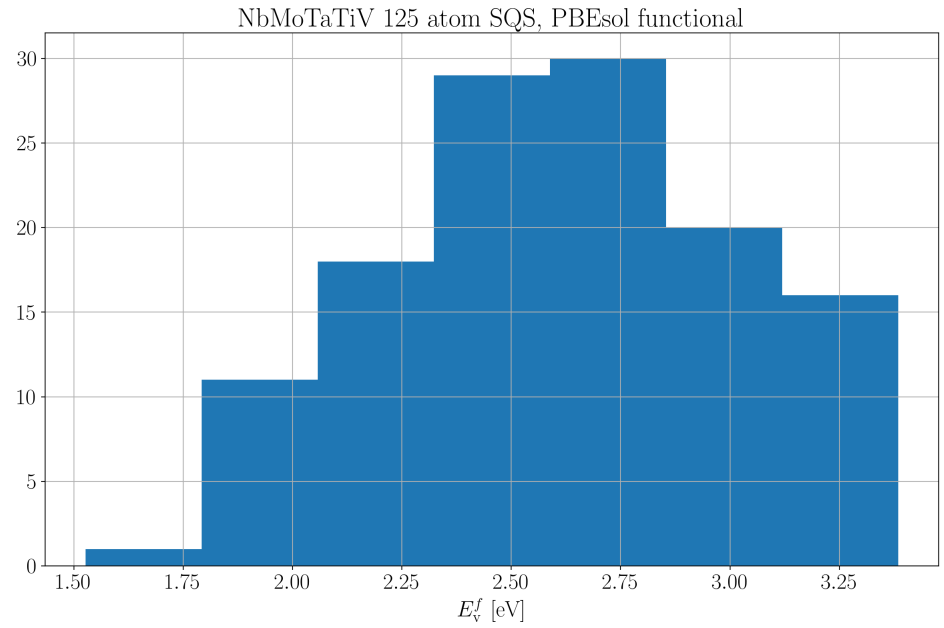

Figure 4-6: The vacancy formation energy distribution for NbMoTaTiV

Table 4.2: Reported vacancy formation energies for pure element components of NbMoTaTiV [76]

element	0 K structure	E_v^F [eV]
Nb	BCC	2.94
Mo	BCC	2.90
Ta	BCC	3.12
Ti	HCP	2.07
V	BCC	2.66

A comparison of the elemental vacancy formation energies for the refractory metals composing the HEA is shown in Table 4.2. The rule–of–mixing average vacancy formation energy of the NbMoTaTiV HEA is 2.74 eV. It is worth noting that the low–energy tail of the distribution, in this case, goes below the vacancy formation energy of any of the pure elements. At the same time, the high–energy tail of the distribution also varies past the highest pure element vacancy formation. In this case,

the peak of the distribution roughly coincides with the rule–of–mixing average.

4.2.1 As–Cast Microstructure

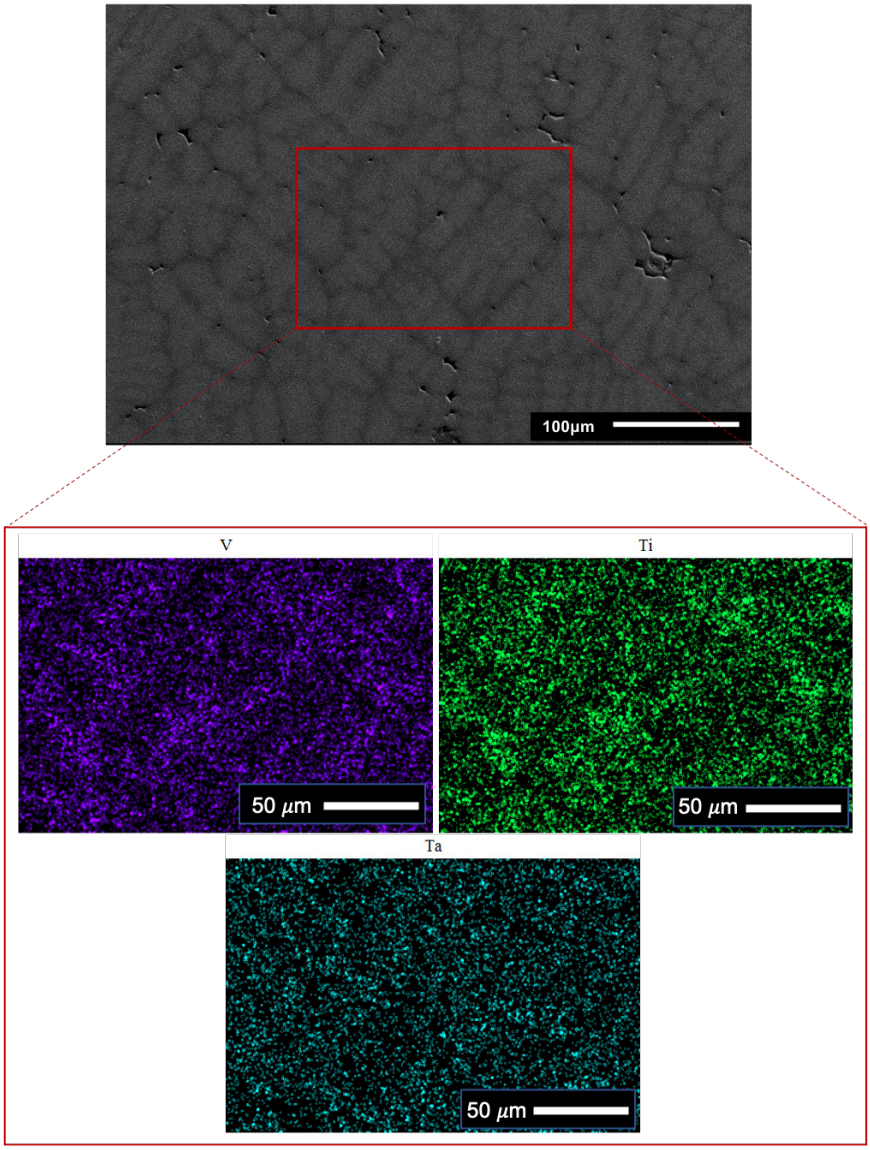

Figure 4-7: SEM image along with V, Ti, and Ta compositional maps.

The as–cast microstructure of NbMoTaTiV is shown in Figure 4-7. We can see that there appears to be a single–phase microstructure but with what appears to be some degree of elemental segregation. EDX analysis, including the elemental map shown in Figure 4-7, reveals that the slightly darker region of material is enriched in Ti and

V while depleted in Ta. Mo and Nb do not appear to have undergone segregation between the regions. A powder XRD pattern for the as–cast NbMoTaTiV HEA is shown in Figure 4-8 confirming the structure as a single–phase BCC material.

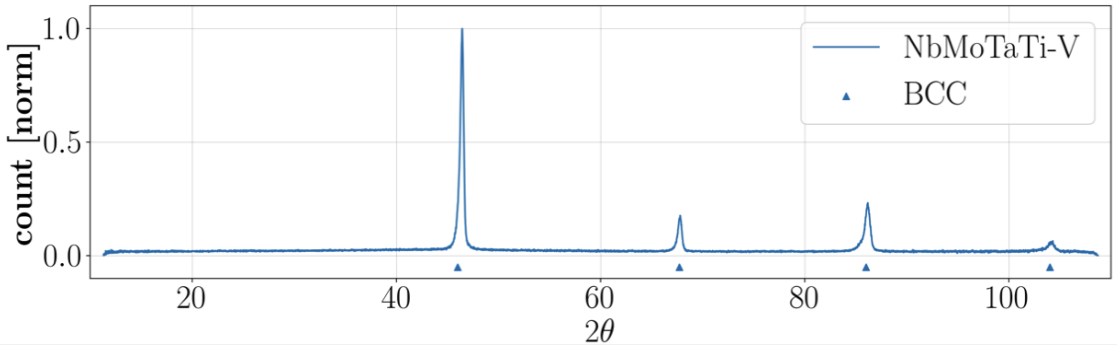

Figure 4-8: Powder XRD pattern of the as–cast NbMoTaTiV HEA showing only BCC diffraction peaks present in the material.

4.2.2 Annealed Microstructure

After finding that the NbMoTaTiV appears to form a single–phase microstructure as–cast with some degree of dendritic segregation, an annealing was performed for 24 hours at 1600°C in an inert argon atmosphere in order to determine if this single–phase stability persists at higher temperatures. After annealing the microstructure of the sample was analyzed using SEM and EDX. SEM images of the annealed microstructure can be seen in Figure 4-9, in which it is clear that significant microstructural evolution occurred during the annealing process. There are no apparent remnants of the dendritic microstructure, but a secondary, dark phase has formed within the light gray matrix. This dark phase is rich in Ti and V. The phase appears to be present both along GBs, with a clear pattern of precipitates densely covering the GB, along with a relatively uniform dispersion of precipitates within the matrix. It appears that there is some preferred orientation relationship between the precipitate and the matrix phase as there appears to be a tendency for the precipitates to be oriented parallel to eachother or at a roughly 90° orientation with respect to the other precipitates. Although this cross–sectional view is not sufficient to totally understand

the precipitate morphology, it appears that the matrix–dispersed precipitates tend to take on a disc–shape.

An EDX linescan of the annealed microstructure is presented in Figure 4-10, demonstrating the strong enrichment of Ti and V within the precipitate phase. Although NbMoTaTiV formed a single–phase upon casting, the formation of precipitates rich in Ti and V at elevated temperatures is demonstrated here. Although the properties of the material were not directly tested here, I suspect that the presence of precipitates within the microstructure will lead to a significant precipitation strengthening effect, but embrittlement is also possible in this case.

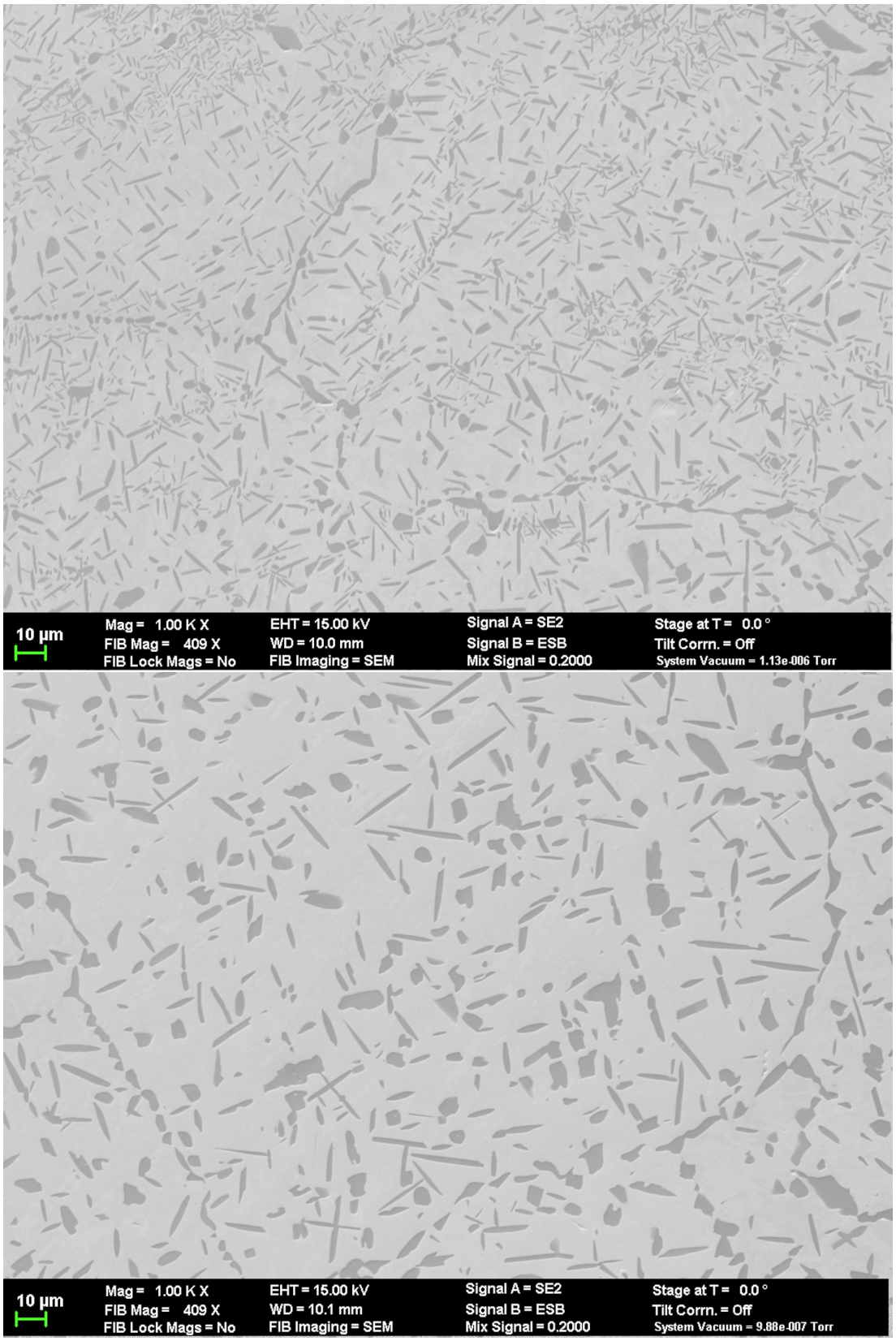

Figure 4-9: SEM images of the annealed microstructure of NbMoTaTiV after annealing at 1600°C.

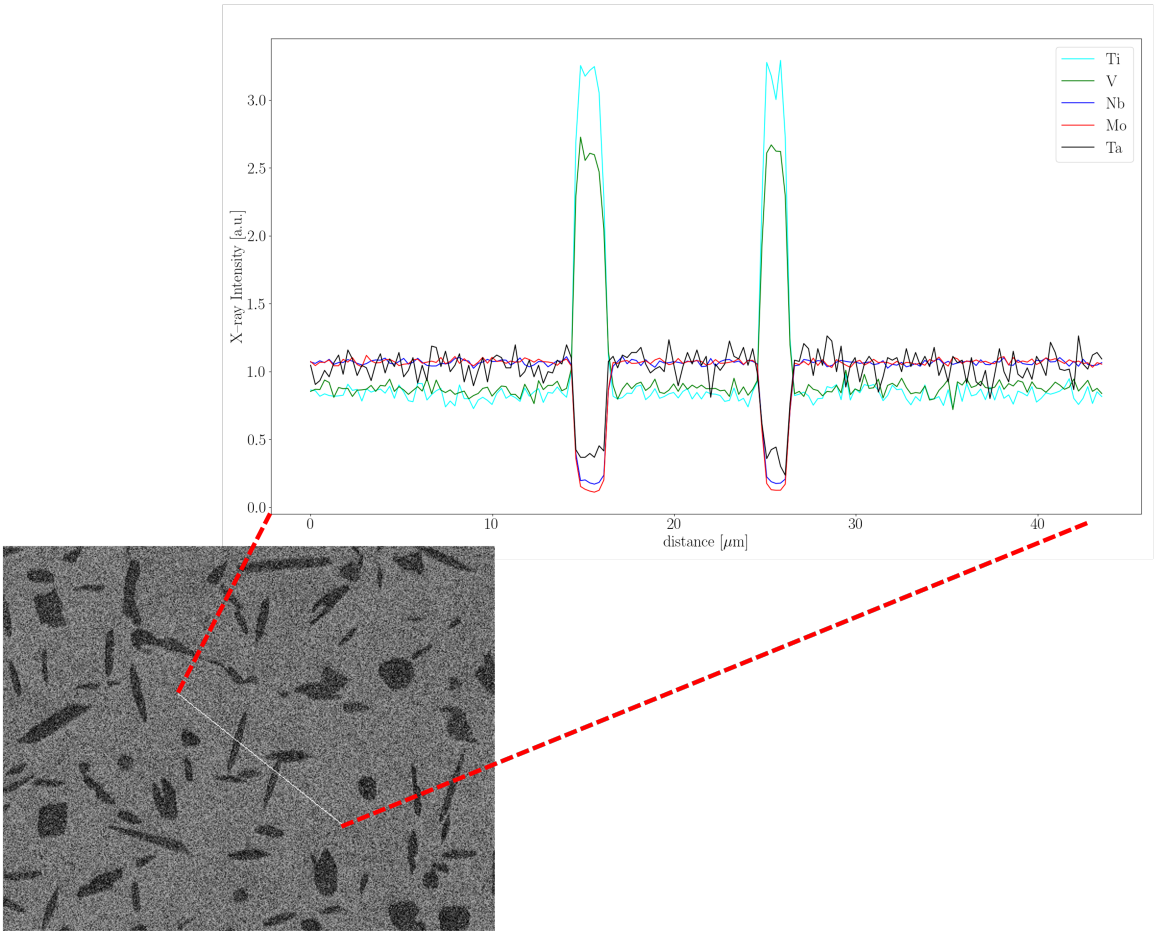

Figure 4-10: EDX linescan of the NbMoTaTiV microstructure after annealing at 1600°C for 24 hours. The linescan path is indicated by the diagonal line on the on the image. The dark precipitate phase is rich in Ti and V.

4.3 NbMoTaTiZr

The NbMoTaTiZr atomistic mixing energy spectrum for a 30–atom BCC SQS is shown in Figure 4-11. In this HEA system, Zr is the least thermodynamically favored component on the basis of the atomistic mixing energy. For Zr the peak of the distribution is slightly negative but there is a significant tail in the positive atomistic mixing energy region. We can see that the ordering from least negative atomistic mixing energy to most negative atomistic mixing energy we have: Zr, Ti, Ta, Mo, and Nb. Again we see that Nb has the most narrow mixing energy spectrum and

appears to be the least sensitive to the local chemical environment. The atomistic mixing energy spectrum for Mo in NbMoTaTiZr appears to be strongly negative but it is relatively broad indicating that Mo is sensitive to the local chemical environment. In this case Ti and Ta have similarly shaped distributions while Ta is slightly more negative.

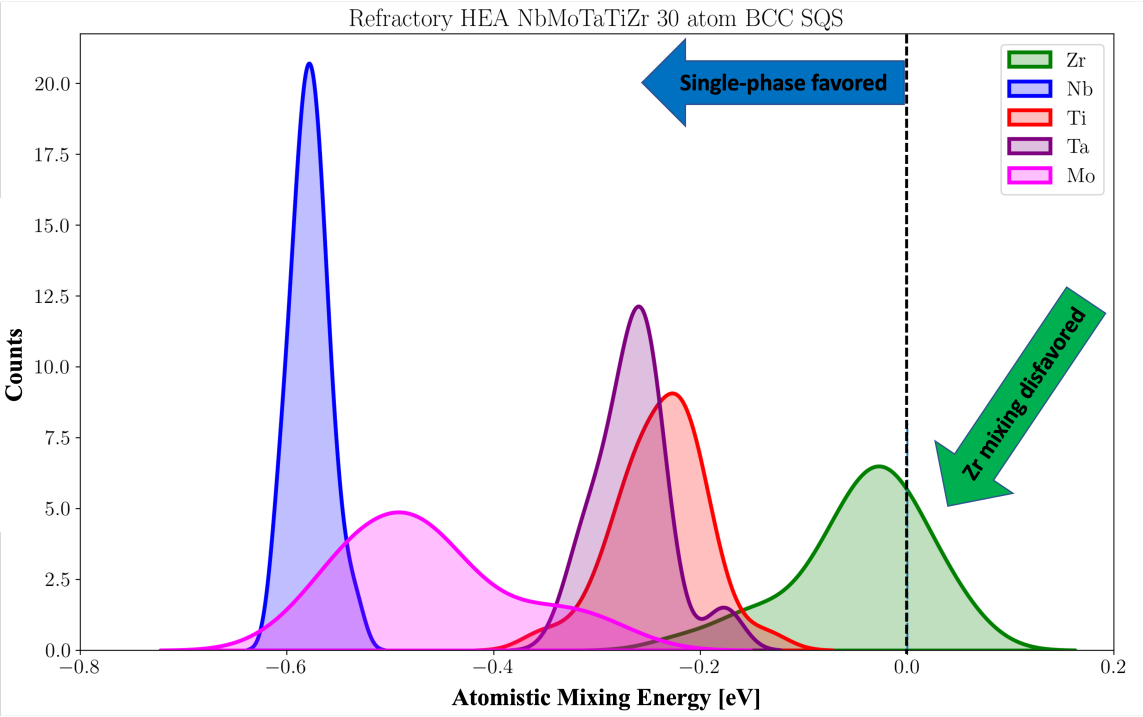

Figure 4-11: The atomistic mixing energy spectrum for a 30–atom NbMoTaTiZr BCC SQS.

4.3.1 As–Cast Microstructure

A low magnification (100x) SEM image of the as–cast microstructure of the NbMoTaTiZr HEA is shown in Figure 4-12. We can see there is a distinct two–phase dendritic structure that developed in the as–cast material. A pair of higher magnification (10,000x and 20,000x) SEM images of the as–cast microstructure are shown in Figure 4-13. Here we see at the interface between the two phases constituting the dendrites and the interdendritic phase, at the sub–micron scale there is an intriguing pattern which appears quite similar to the dendritic pattern in the much lower mag-

nification SEM image.

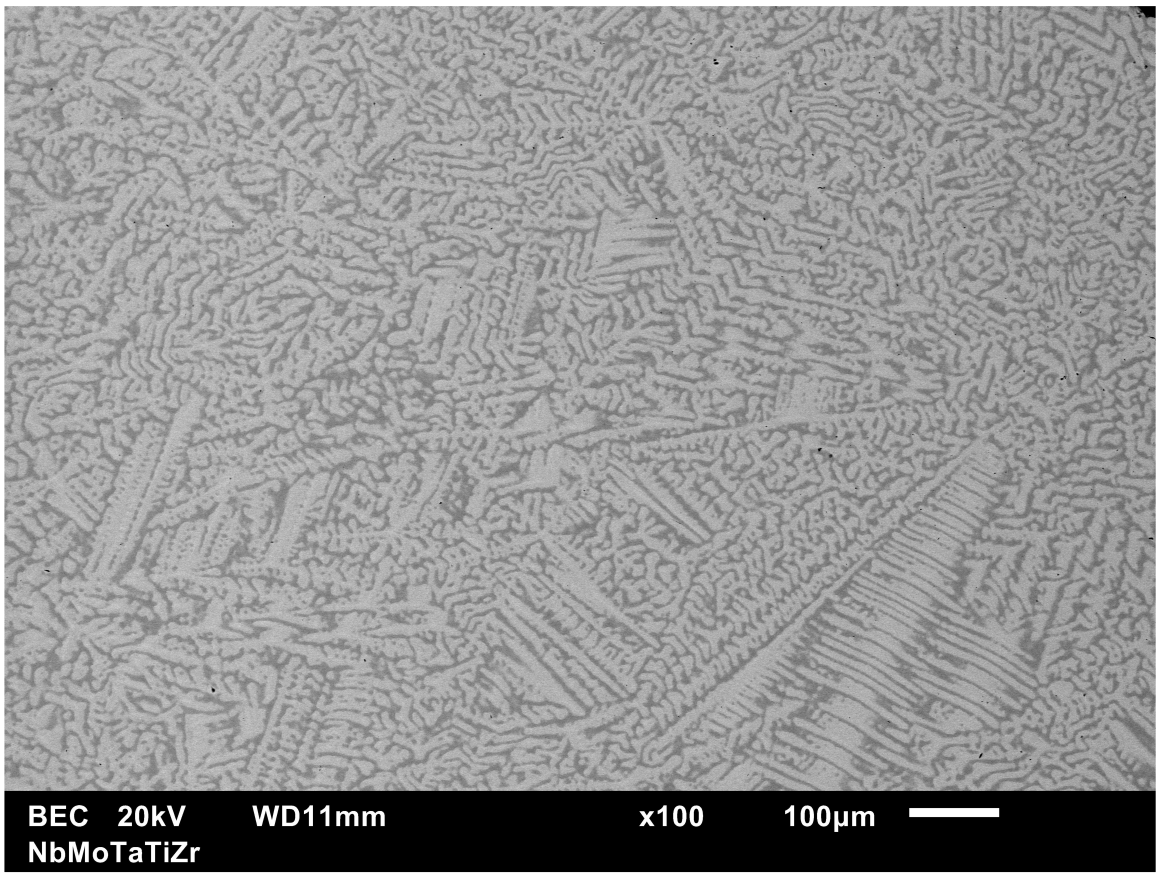

Figure 4-12: Low–magnification SEM image of as–cast NbMoTaTiZr showing large dendrites with dark interdendritic regions.

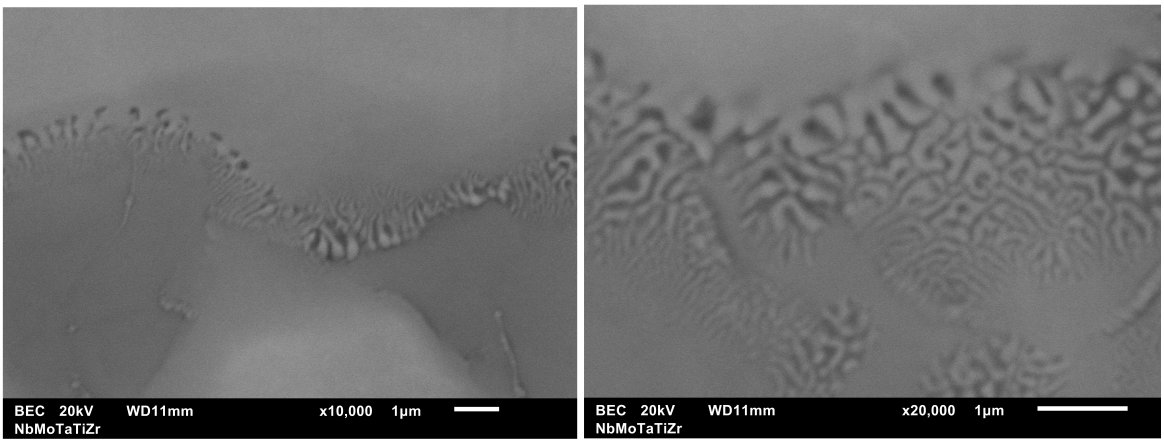

Figure 4-13: Higher magnification SEM images of as–cast NbMoTaTiZr showing the interface between the dendritic and interdendritic regions.

Shown in Figure 4-14 is further characterization analysis of the as–cast NbMoTaTiZr microstructure. The dark interdendritic phase of the material is shown to be enriched in Zr and Nb while the brighter dendrite phase has relatively higher concentrations of Mo and Ta while Ti appears to have only slightly segregated into the dark phase. The results of the phase analysis are somewhat surprising given the negativity of the Nb atomistic mixing energy, but this case clearly shows the importance of the consideration of the other potential phases which can form besides the disordered solid solution BCC phase. This same alloy has been studied previously, with intended applications in biomedical implants. This study also found a multiphase microstructure with similar reported XRD patterns as the XRD pattern shown in Figure 4-14 showing 2 distinct sets of BCC peaks [77]. One notable difference is that I report enrichment of Nb in the interdendritic phase, while previous studies found that Nb was co–located with Ta and Mo instead.

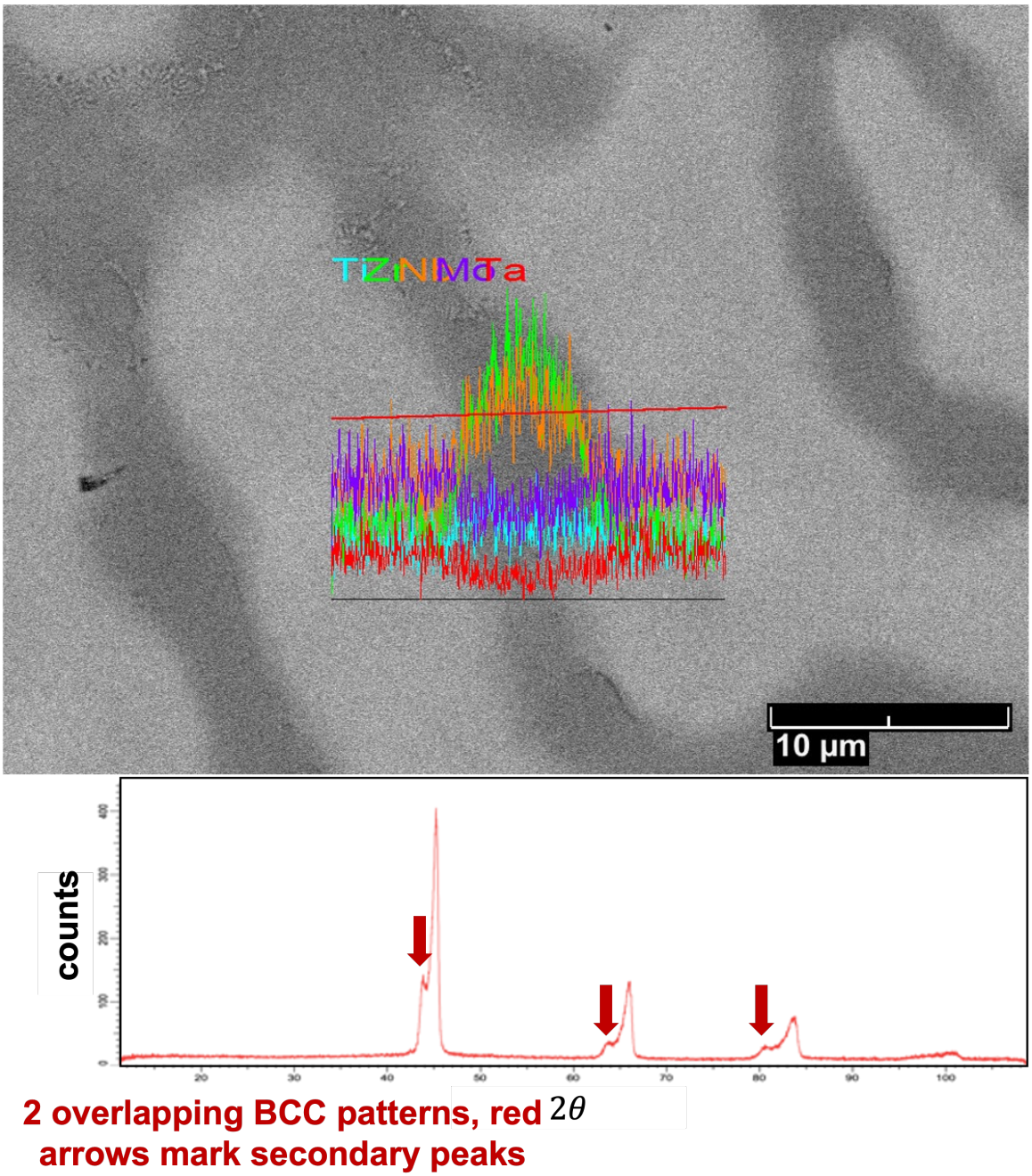

Figure 4-14: EDX linescan (top) and powder XRD analysis (bottom) of as–cast NbMoTaTiZr.

4.4 NbMoTaHfW

The atomistic mixing energy spectrum for a NbMoTaHfW 125–atom BCC SQS is shown in Figure 4-15. The peak of Nb in the atomistic mixing energy distribution is noticeably tall and narrow, while Mo has the negative distribution though it appears quite broad including some positive atomistic mixing energy sites. Ta and W appear to have quite similar distributions in this HEA, and both appear slighlty negative but with significant positive mixing energy tails. Finally, Hf has a broad, positive atomistic mixing energy distribution in this material indicating clearly a preference for Hf to not mix with the disordered solid solution.

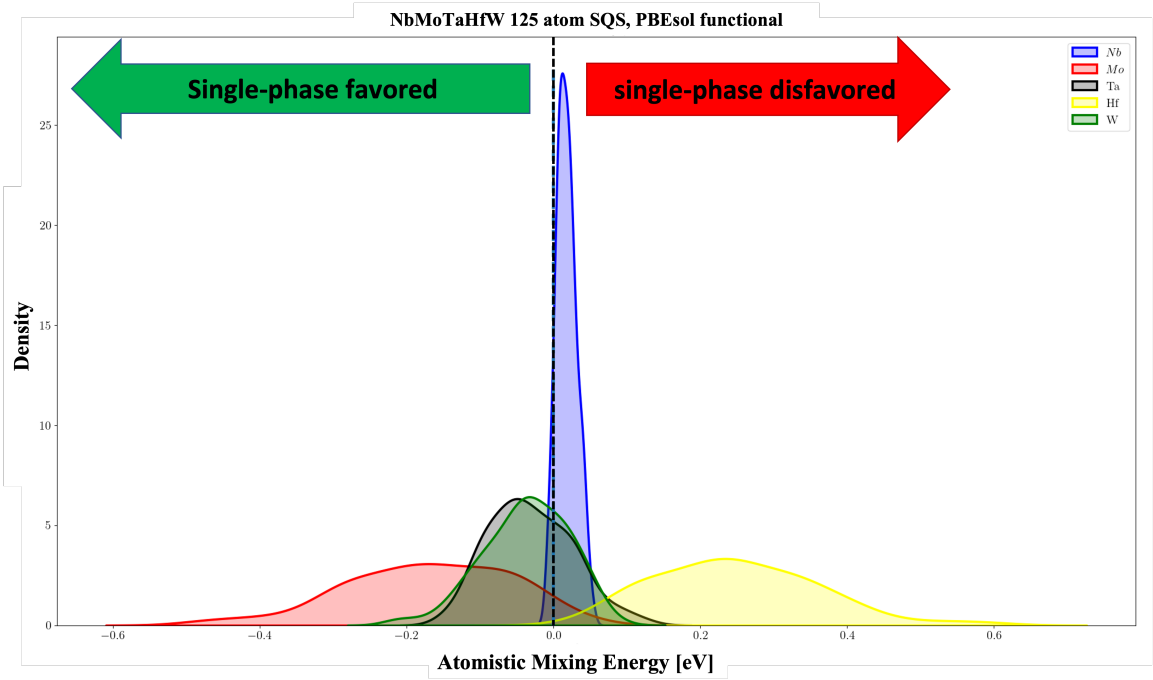

Figure 4-15: The atomistic mixing energy distribution for a 125–atom BCC NbMoTaHfW SQS.

The vacancy formation energy distribution for equimolar NbMoTaHfW is shown in Figure 4-16. The distribution of vacancy formation energies is interesting in that there is a low energy tail around 1 eV while also a large fraction of sites with vacancy

formation energies above 3.5 eV. Overall the distribution is skewed towards high vacancy formation energy sites.

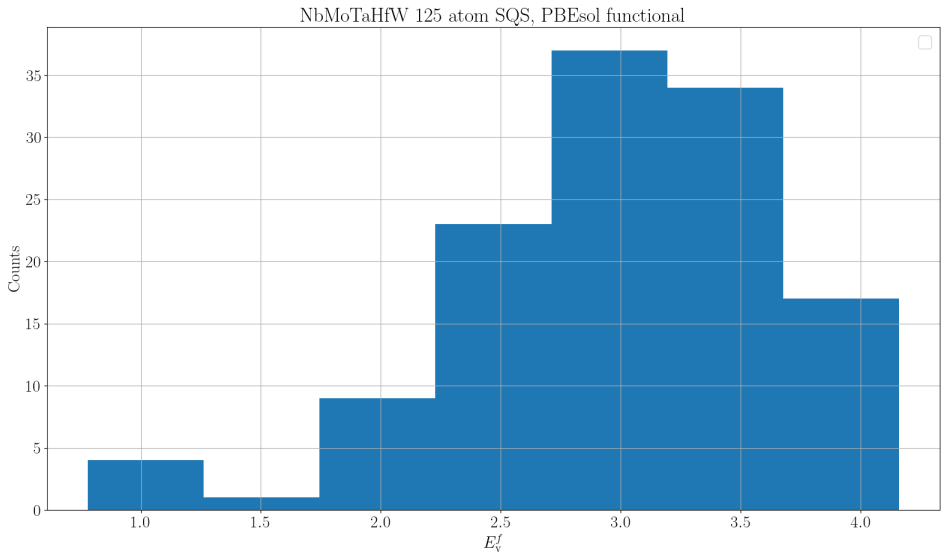

Figure 4-16: Vacancy formation energy distribution for 125–atom NbMoTaHfW SQS

The vacancy formation energy for the elemental components are given below in Table 4.3, while the rule–of–mixing average vacancy formation energy is 2.88 eV, which generally corresponds with the mode of the distribution shown in Figure 4-16, while it is also worth noting that there is a significantly skewed low energy VFE distribution in addition to quite high energy VFE sites as well. Again, we see that the range of vacancy formation energies calculated for the equimolar BCC SQS is greater than the range between the pure element components.

Table 4.3: Reported vacancy formation energies for pure element components of NbMoTaHfW [76]

element	0 K structure	E_{v}^{f} [eV]
Nb	BCC	2.94
Mo	BCC	2.90
Ta	BCC	3.12
Hf	HCP	2.19
W	BCC	3.27

4.4.1 As–Cast and Annealed Microstructure

A backscatter electron (BSE) micrograph of the as–cast NbMoTaHfW microstructure is shown in Figure 4-17. We can see clearly in the BSE image two distinct regions of material. Although this microstructure could certainly be described as dendritic it is also unique that it appears there is a segregated dark region between the dendrites, but also some degree of segregation at the dendrite core, which appears darker and forms channels to the interdendrite phase. The NbMoTaHfW was also annealed for 24 hours at 1600°C after casting, but the microstructure appeared to undergo little change during the annealing, with the same multiphase structure observed. Figure 4-18 shows an EDX elemental map of the annealed NbMoTaHfW HEA demonstrating the remaining multiphase structure after annealing and the dark phase appearing enriched in Hf while the primary bright matrix phase is enriched in Mo compared to the dark phase, which is generally in agreement with the behavior predicted by the atomistic mixing energy analysis.

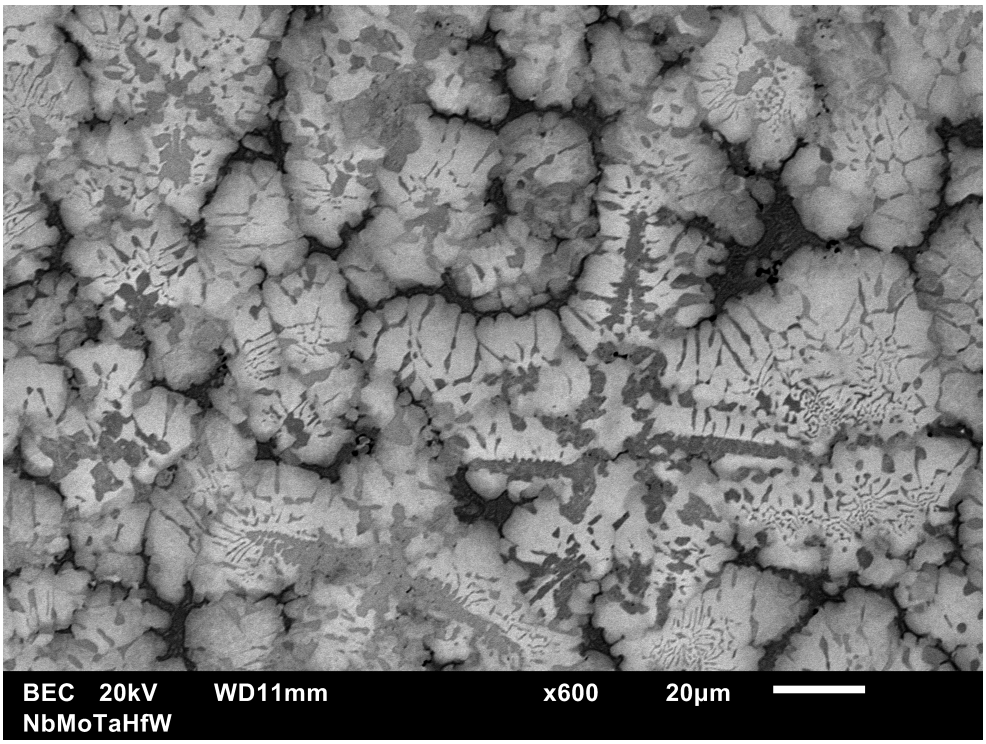

Figure 4-17: Backscatter SEM image of the as–cast NbMoTaHfW HEA.

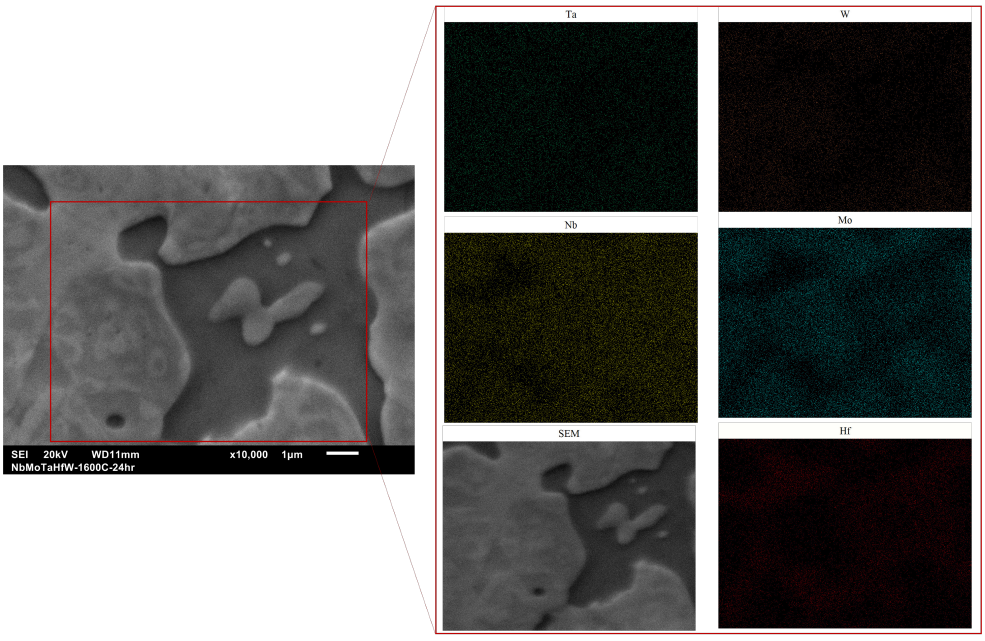

Figure 4-18: SEM image and EDX elemental map of NbMoTaHfW annealed for 24 hours at 1600°C.

4.5 Discussion

In this chapter the atomistic model developed in the previous chapter is applied to 4 different 5–component HEAs, all sharing the NbMoTa ternary base: NbMoTaTiW, NbMoTaTiV, NbMoTaTiZr, and NbMoTaHfW. The only composition which was found to form a single–phase microstructure in the cast material was NbMoTaTiV, while multiphase microstructures were found in NbMoTaTiW, NbMoTaTiZr, and NbMoTaHfW. Although NbMoTaTiV was single–phase, some degree of elemental segregation was also found, which is not uncommon in HEAs studied previously [78]. A 24 hour anneal of NbMoTaTiV at 1600°C caused precipitation of finely dispersed precipitates rich in Ti and V within the BCC matrix as well as along the GBs.

The atomistic mixing energy results for NbMoTaTiV showed that all elements take a negative mixing energy meaning that mixing into the disordered alloy is thermodynamically favored for all elements. Furthermore, of the elements present in the HEA, Ti and V had the least negative atomistic mixing energy indicating that these were the 2 elements least favored to mix in the HEA. Considering that these elements were those present in the intermetallic precipitate which formed after annealing at 1600°, it seems that the atomistic mixing energy analysis can provide useful insights into the thermodynamics of HEAs.

In the other HEAs explored in this chapter, the presence of elements with a positive atomistic mixing energy within the HEA system was a dependable indicator of thermodynamic instability of the single–phase BCC system. In the NbMoTaTiW HEA, Ti takes a reasonably large fraction of positive sites, and in the as–cast NbMoTaTiW HEA a multiphase microstructure was found, with a dark Ti rich phase, which was found by XRD to be HCP Ti. In NbMoTaTiZr, a positive mixing energy for some sites was observed for Zr, and in the as–cast NbMoTaTiZr material a dual–phase dendritic microstructure formed which included a Zr–rich dark interdendritic phase. Within NbMoTaTiZr, Nb was shown to have a strongly negative atomistic mixing

energy compared to other HEAs analyzed but in the as–cast alloy it appears that Nb segregates into the Zr–rich dark interdendritic phase. This can be intuitively understood as a result of a strong attractive Nb–Zr interaction on the BCC lattice which induced the formation of a secondary Nb–Zr rich BCC phase. Finally, NbMoTaHfW included Hf which had the most positive mixing energy of any of the elements and systems studied in this chapter. All sites in the SQS studied had a positive mixing energy for Hf. In the as–cast material there was a distinct dual–phase structure with a Hf–rich dark phase and Mo–rich dendritic phase (Mo had the most negative atomistic mixing energy).

The results in this chapter reveal that the atomistic mixing energy approach to analyzing HEA thermodynamics is versatile and reliable in giving nuanced information about the thermodynamic mixing behavior of refractory HEAs and complex solid solution alloys more generally. In addition to the insights provided which are relevant to alloy design, the approach developed in this work also facilitates the proper calculation of the vacancy formation energy in disordered solid solutions. The ability to understand not just the mean value of the vacancy formation energy but the entire distribution in a complex solid solution provides novel insights into the fundamental defect behavior of these materials. For instance, often times the low and high energy tails of the vacancy formation energy distribution span a significantly wider range than the range of the vacancy formation energy of the pure elements. This is important, because one conclusion that can be drawn is that the rule–of–mixing approach might provide a reasonable estimate of the mode of the vacancy formation energy distribution, but the range of possible vacancy formation energies is quite broad and the tails of the distribution could have an important influence on the behavior of the system. For instance, at relatively low temperatures the low energy vacancy formation energy sites will be activated while the high energy tail will not be as involved. In the case of non–equilibrium processes such as radiation damage, the high energy tail will also play a role, and the distribution of formation energies would play an important role in recombination and clustering/agglomeration of vacancies.

Finally, it is worth noting that the atomistic mixing energy model developed in this work performs significantly better in predicting the phase stability of HEAs in comparison with previous models developed by King *et al.* [74, 75] and Troparevsky *et al.* [56]. We can conclude from this better performance that the mixing energy of the solid solution phase, and the different driving forces for different elements, is a significant factor in phase stability and cannot be ignored as it is in the model developed by Troparevsky *et al.* Additionally, we can conclude that the more accurate atomistic model developed in this work is highly valuable compared to the mean–field, simplistic approach of the Miedema model in giving more quantitatively accurate information about the mixing energy along with allowing to discern the different driving forces for mixing for each HEA component.

Chapter 5

WTaVTiCr High Entropy Alloy System

In the previous chapter, several high entropy alloys which all contained both Nb and Mo were analyzed by atomistic simulation, synthesized in the laboratory using the arc melting approach, and characterized in order to determine the resulting microstructure. Although this work is important for the development of refractory alloys for potential advanced nuclear applications, especially in which the operating temperature is relatively high, there are some disadvantages to the inclusion of both Nb and Mo. In particular, these two elements undergo transmutation reactions when exposed to neutrons that leads to long–lived radioisotopes which make material handling and eventual disposition challenging. Of the other refractory metals, in addition to Mo and Nb, Hf also creates long–lived radionuclides while the other 6 refractory metals (V, Ti, W, Ta, Zr, Cr) generally have good neutron activation characteristics [41]. Therefore, in focusing specifically on refractory HEAs for nuclear energy applications it is reasonable to limit the elemental components to these 6 low–activation refractory metals. In this chapter, I focus specifically on the WTaVTiCr HEA system, which has received attention previously as a potential HEA for nuclear fusion applications. In particular WTaVTiCr and derivative alloys within this system have attracted interest for fusion first wall applications and other plasma–facing components [79–81]. I use the atomistic mixing energy approach to analyze the WTaVTiCr in order to

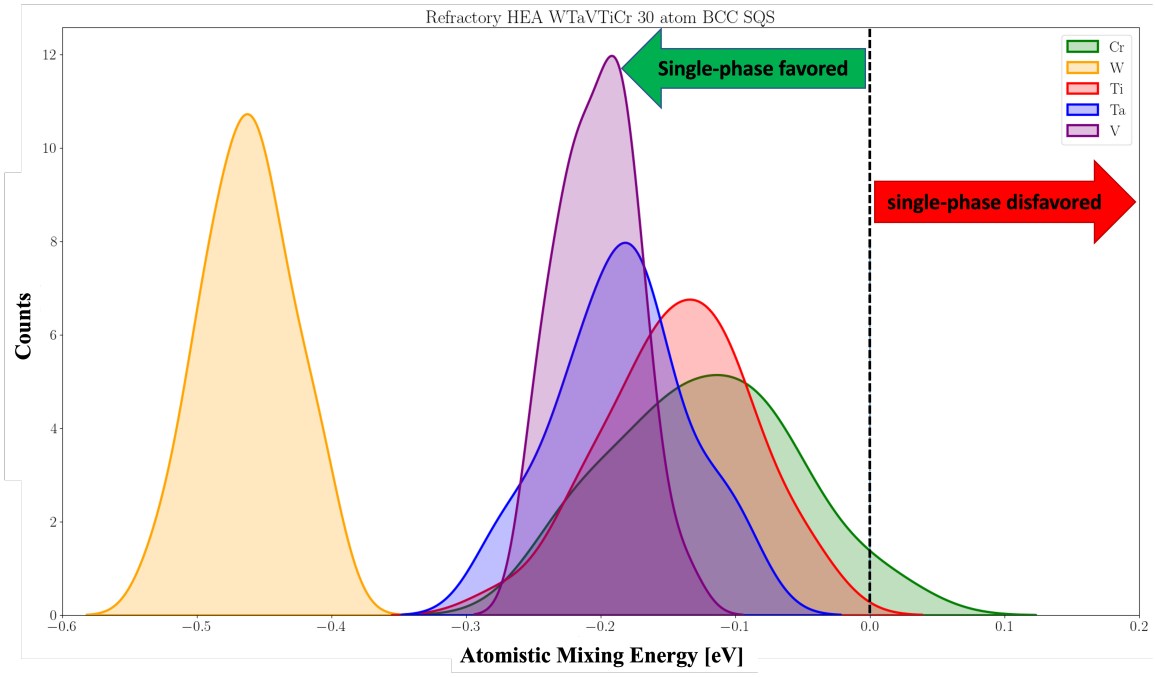

Figure 5-1: The calculated atomistic mixing energy spectrum for WTaVTiCr 30–atom BCC SQS. The analysis shows W has a larger driving force for mixing than any other component in this HEA.

understand this system and suggest paths forward for single–phase alloy design.

5.1 Atomistic Simulation

The WTaVTiCr system was modeled as a BCC solid solution in the same manner as the other refractory HEAs studied previously in this work. A 30–atom BCC SQS produced using the `mcsqs` package within ATAT. More detail about the SQS and generating SQS supercells is available in section A.1. The results of the atomistic mixing energy analysis of the 30–atom SQS for WTaVTiCr is shown in Figure 5-1.

We see in the atomistic mixing energy spectrum that the mixing energy is generally negative for most components, while Cr does have some number of positive AME sites. Generally it appears that Ti and Cr have the least negative atomistic mixing energy and are predicted to be less favored to mix in the HEA. W clearly has the most negative atomistic mixing energy, while Ta and V both have comparably

negative atomistic mixing energy distributions. It is also noteworthy that W and Ta appear to have the most narrow atomistic mixing energy distributions indicating that they are relatively less sensitive to the local chemical environment in comparison to V, Ti, and Cr. Based on the atomistic mixing energy spectrum we can conclude that the analysis predicts W, Ta, and V will be relatively more stable in the BCC WTaVTiCr HEA while Ti and Cr will be relatively less stable.

The vacancy formation energy distribution for the WTaVTiCr 30–atom SQS is shown in Figure 5-2. It is apparent that the vacancy formation energy distribution ranges from approximately 2 eV to 3.75 eV. It is worth noting again that the lowest energy vacancy sites will be active at lower temperatures while the entire distribution of vacancies will be active at high temperatures. Previously, Shang *et al.* calculated using first–principles simulation the vacancy formation energy of many pure elements in different crystal structures [76]. The pure element vacancy formation energies for the components of WTaVTiCr are shown in Table 5.1.

Table 5.1: Reported vacancy formation energies for pure element components of WTaVTiCr [76]

element	0 K structure	E_{v}^{f} [eV]
Ta	BCC	3.12
W	BCC	3.27
V	BCC	2.66
Ti	HCP	2.07
Cr	BCC	2.93

For an equimolar WTaVTiCr alloy, the rule-of-mixing (ROM) predicted value for the VFE is 2.81 eV. This value is quite close to the peak of the distribution, while the higher VFE tail of the distribution varies well past the highest elemental VFE (W, 3.27 eV). Meanwhile, the low VFE tail of the distribution approximately coincides

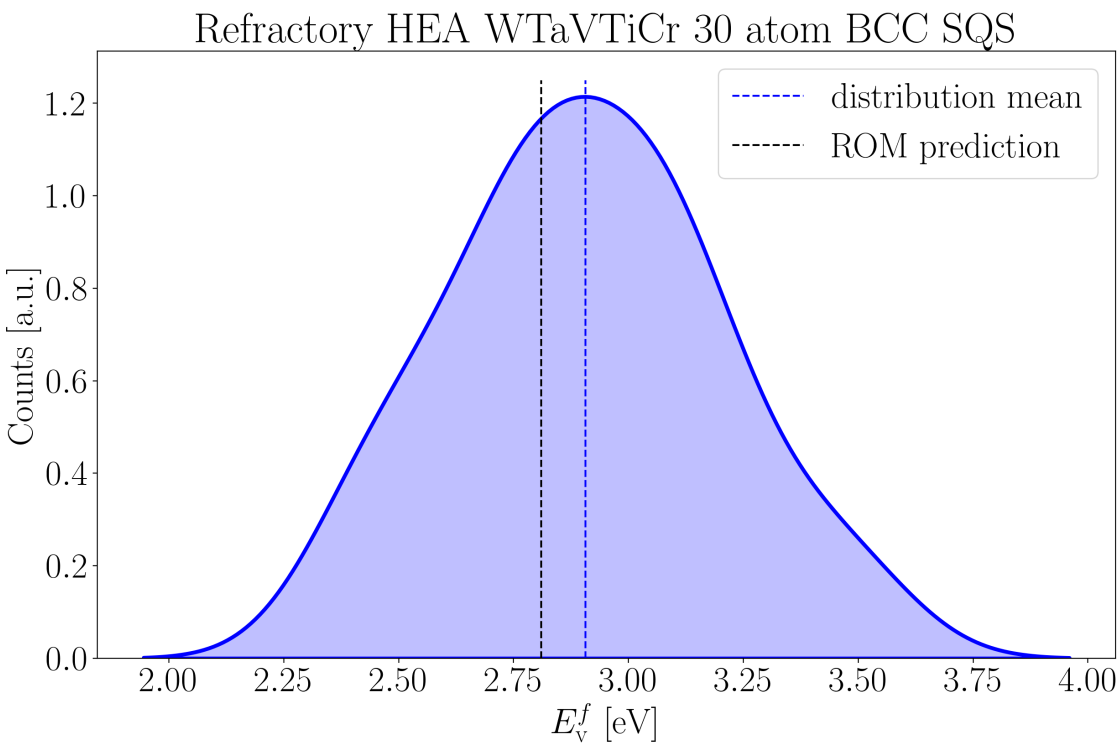

Figure 5-2: The calculated vacancy formation energy distribution for the WTaTiVCr HEA in a 30–atom BCC SQS.

with the lowest elemental VFE (Ti, 2.07 eV). This demonstrates that it appears the ROM gives a reasonable estimate of the most likely VFE, but using atomistic simulation to understand the distribution of VFEs across different sites allows us to develop a more fine–grained understanding, especially the high–VFE tail indicating higher formation energy vacancies than any of the constituent elements.

5.2 As–Cast Microstructure

The equimolar WTaVTiCr HEA was synthesized at the laboratory–scale using the arc–melter approach, as described in section B.1. After casting, the sample was cut into sections using a low–speed saw, then mounted in conductive bakelite mounting material for sample polishing and microstructural characterization. A low–magnification SEM image of the as–cast microstructure is shown in Figure 5-3. The as–cast microstructure shows a pronounced dendritic structure along with casting defects. The

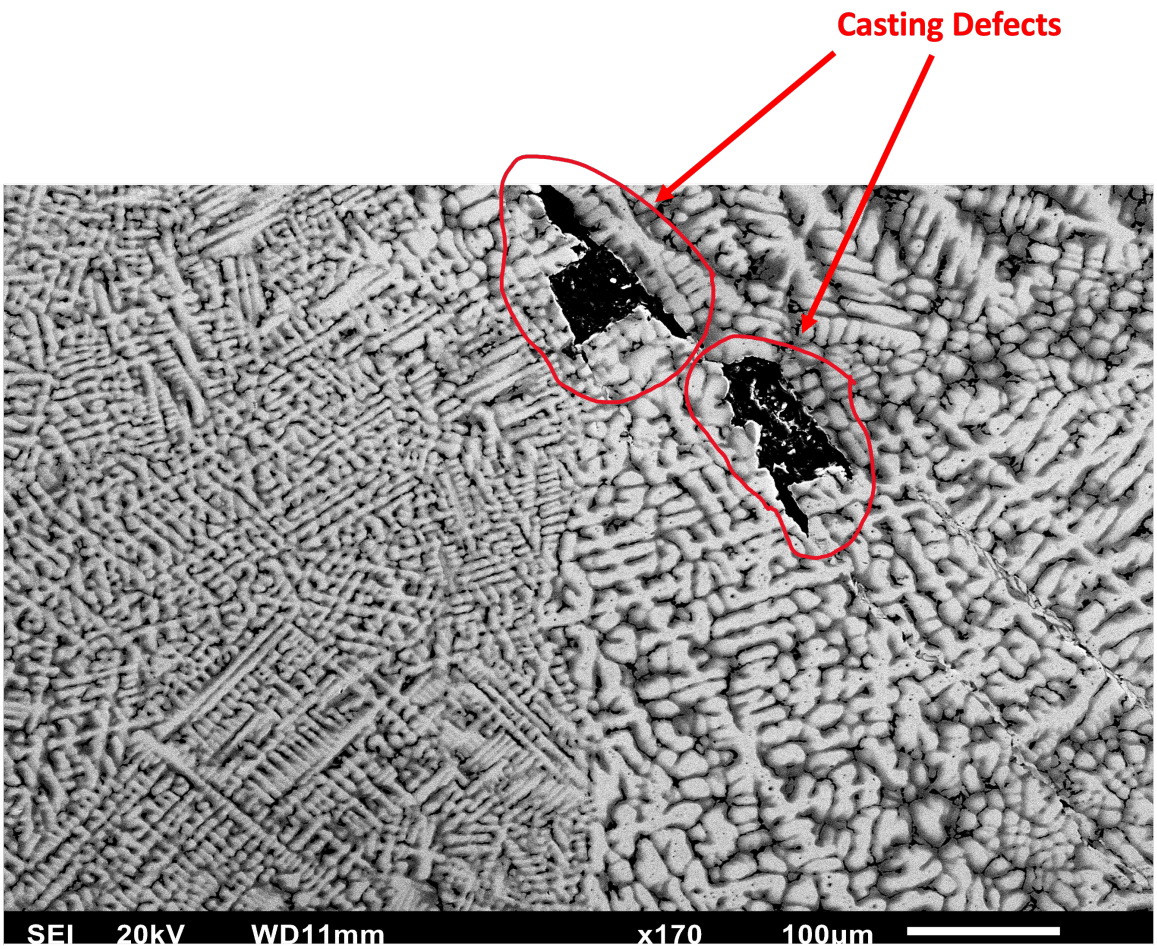

Figure 5-3: Low–magnification (170x) SEM image of as–cast WTaVTiCr HEA

dendritic microstructure which is apparent is different in different locations in the sample. The characteristic length–scale of the dendrites is smaller in regions with a higher cooling rate, so it is reasonable to suspect the portion of the sample with the finer dendritic structure is the portion of the sample which was adjacent to the water–cooled copper hearth and therefore cooled more quickly.

Another low–magnification (230x) SEM image of the as–cast microstructure is shown in Figure 5-4. In this image we again see a strong dendritic microstructure with a light gray dendrite phase, an interdendritic phase which appears black, and a dark gray region in between. In order to understand the distribution of elements within these different regions of the microstructure of as–cast WTaVTiCr, an EDX linescan

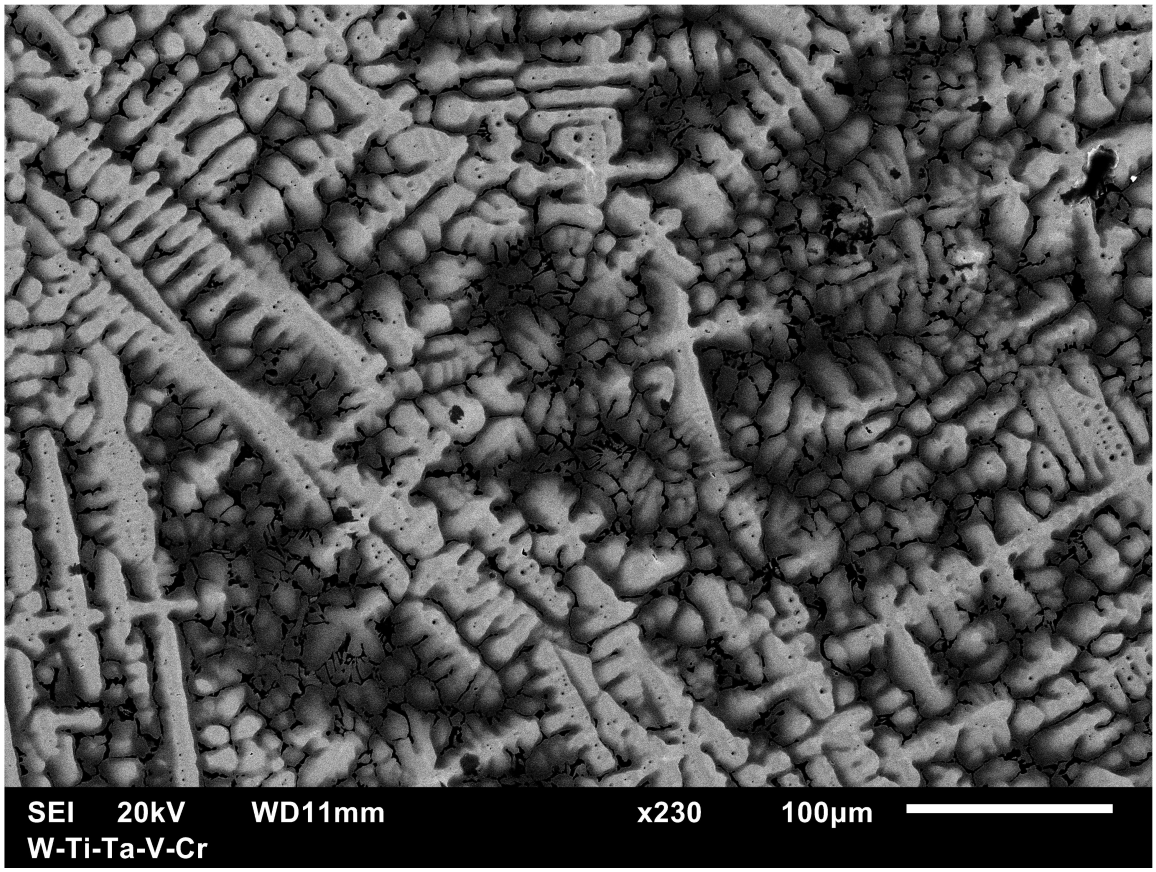

Figure 5-4: SEM image of the as–cast WTaVTiCr microstructure showing bright dendrites with dark interdendritic phase in between

was performed across the different regions of material. Figure 5-5 shows the results of the EDX linescan (the linescan path is marked with the horizontal red line) within the as–cast microstructure. We can see that the bright gray dendritic region is rich in W and Ta, while the dark gray region is rich in V, Cr, and Ti. The black interdendritic phase appears to be very rich in Ti with some V content as well. This interdendritic phase could be an HCP–Ti phase. The results shown here are generally in agreement with the atomistic mixing energy analysis shown previosly. W and Ta are the most favored to mix into the BCC HEA, while Cr, Ti, and V are less stable in the BCC HEA in a relative sense. Although Ti is not the most positive atomistic free energy, it is the element which appears to be precipitating out of the alloy, while V and Cr segregate to the region between the dendrites and the interdendritic phase (Ti).

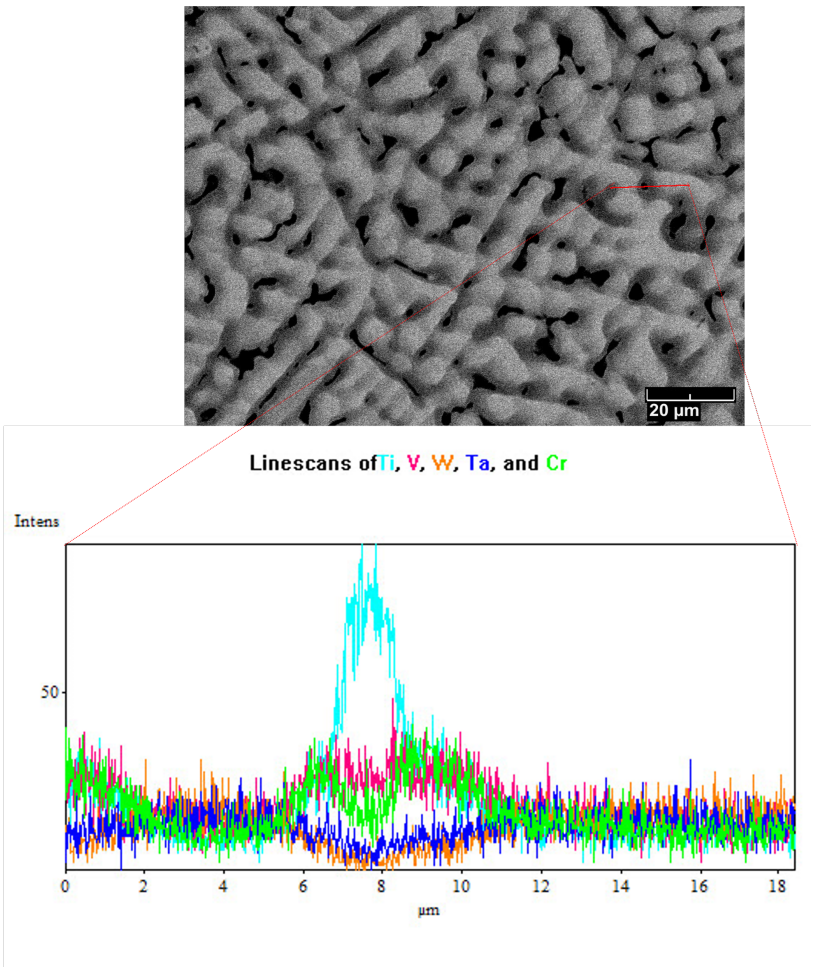

Figure 5-5: EDX linescan of the as–cast WTaVTiCr material showing the distribution of elements in different regions of the microstructure. The linescan path is marked with a horizontal red line on the image.

5.3 High Temperature Annealing

Following examination of the as–cast microstructure, attention turned to understanding the effect of annealing and exposure to high temperatures on the microstructure of the material. In particular, annealing was performed for 24 hours at 1200°C and 1600°C each in order to understand the microstructural evolution at elevated temperatures. After annealing, the samples were again sectioned, mounted in a conductive bakelite material, and polished using SiC metallurgical paper and diamond–particle

suspension in order to examine the resulting microstructure using SEM and EDX.

5.3.1 1200°C, 24 hours

Low–magnification SEM images of the microstructure after 24 hours of annealing at 1200°C are shown in Figure 5-6. The dendritic microstructure present in the as–cast material is still apparent in the sample after annealing for 24 hours at 1200°C. A light gray dendritic region is still present, with a black interdendritic phase with a dark gray region separating these parts of the microstructure. It does appear that there was some degree of dissolution of the interdendritic black phase into the surrounding matrix, but certainly not nearly enough to alter the general dendritic microstructure present in the material. The dark gray region separating the Ti–rich interdendritic phase and the dendrites has become larger and more uniform throughout the microstructure.

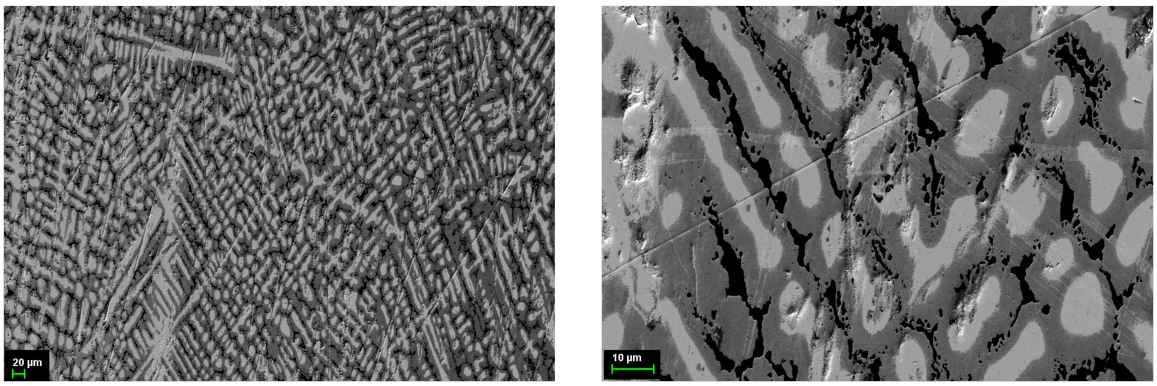

Figure 5-6: 324x (left) and 2,290 (right) SEM images of the microstructure of WTaTiVCr after 24 hours of annealing at 1200°C

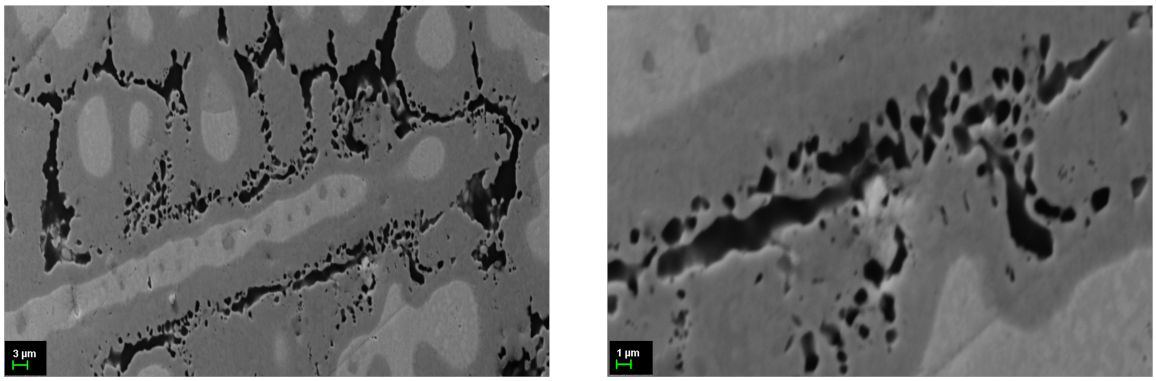

Figure 5-7: Microstructure of Annealed WTaTiVCr after 24 hr at 1200°C

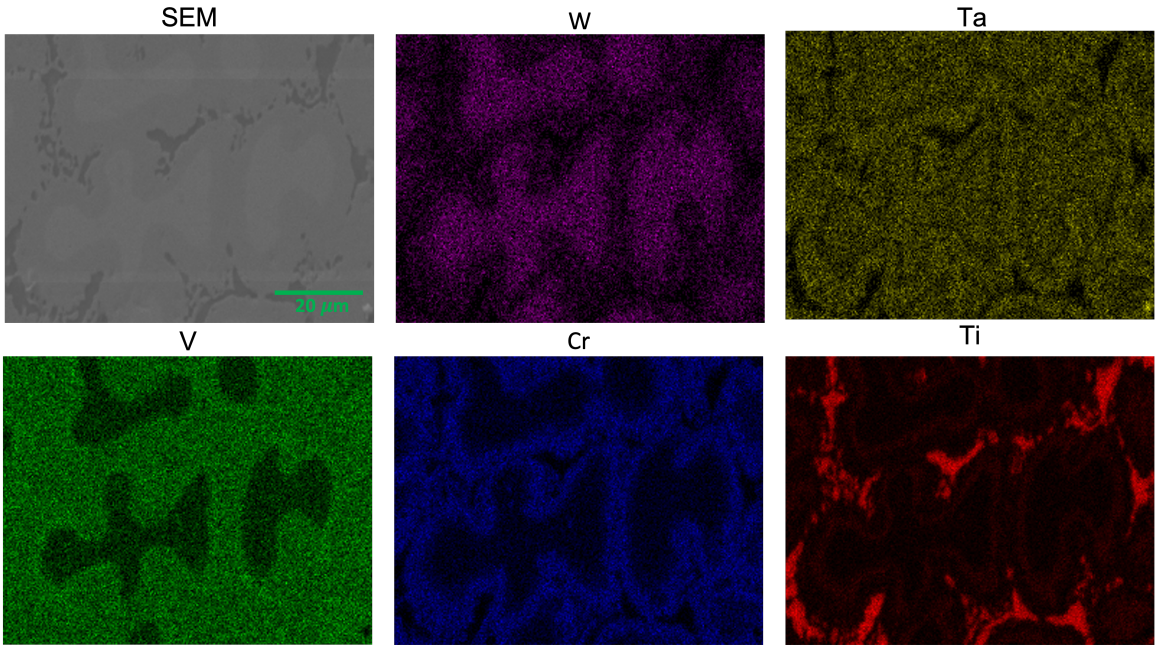

Figure 5-8: WTaVTiCr EDX elemental maps. The imaged region is 64.8μm x 82.9 μm.

Additional SEM images of the microstructure are shown in Figure 5-7, where it is clear that there has been some degree of dissolution of the interdendritic phase by the small discontinuous precipitates surrounding the continuous sections of the interdendritic phase. An EDX elemental map array for the annealed material is shown in Figure 5-8. W is clearly segregated into the bright dendrite phase, is slightly depleted in the boundary region, and is totally absent from the black interdendritic phase. Ta

appears to be most highly concentrated in the dark gray boundary region between the dendrites and the interdendrite phase, and slightly depleted in the dendrites, while it appears absent from the interdendrite phase. Ti is clearly very concentrated in the interdendrite phase, and is present in only in very dilute quantities in the boundary region between the dendrite core and the Ti–rich interdendrite phase and is absent from the dendrite core. Cr is most concentrated within the boundary region and is more dilute within the dendrite core.

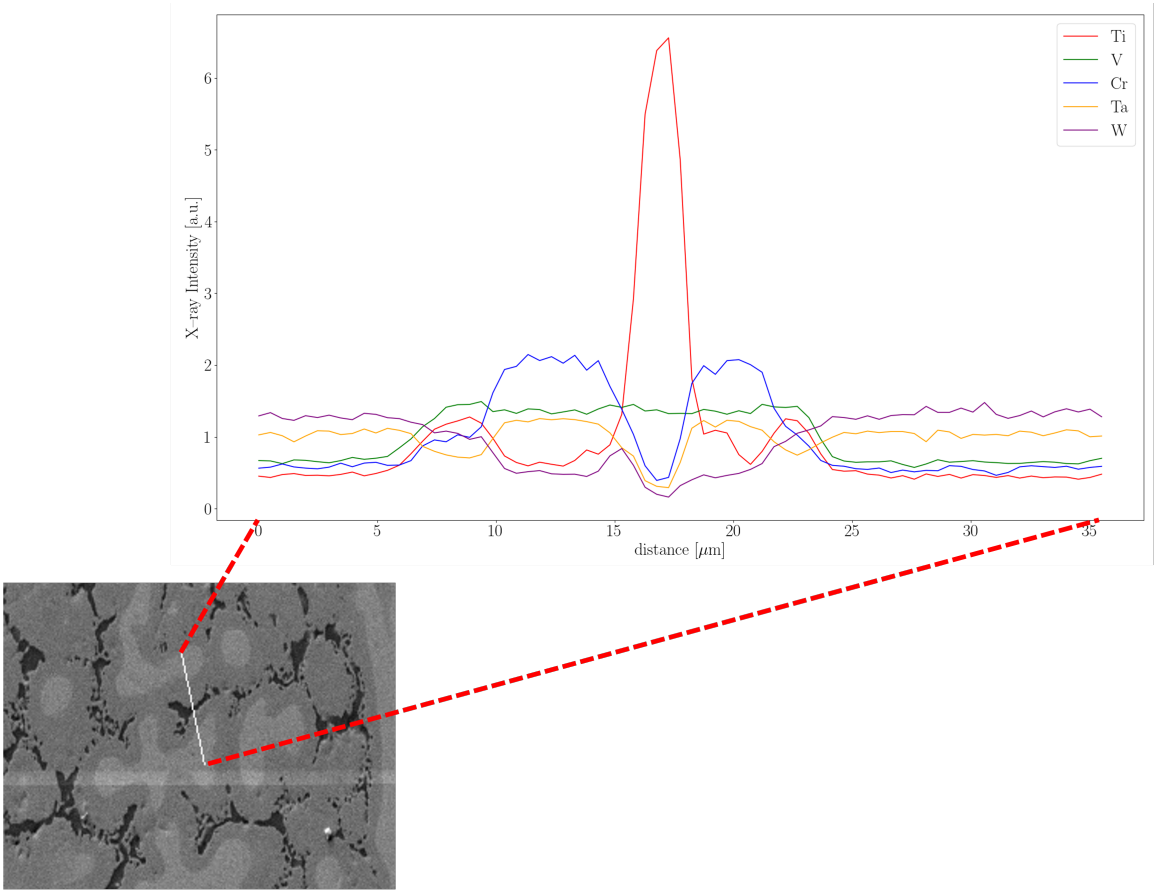

Figure 5-9: WTaVTiCr EDX linescan showing the dendrite, boundary region, and interdendritic phase.

In Figure 5-9 an EDX linescan of the annealed microstructure is shown, crossing different regions of the material, namely the bright dendrite region, the darker boundary

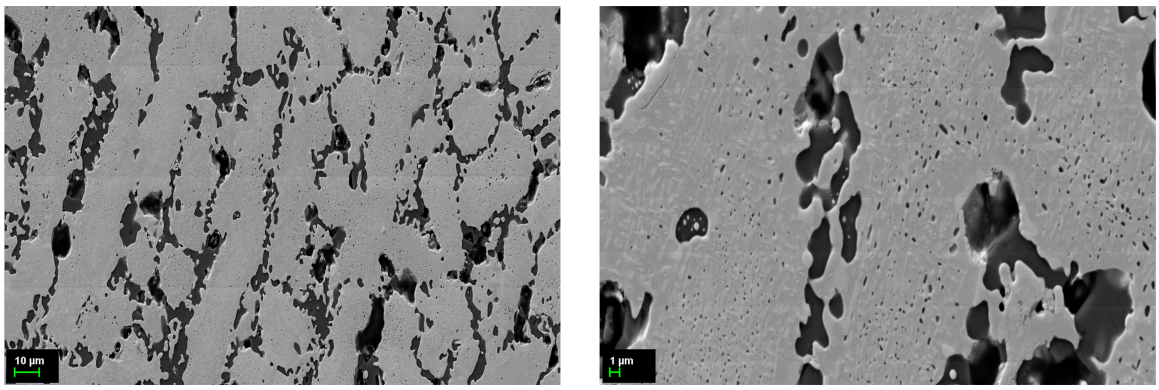

Figure 5-10: 500x (left) and 2,000x (right) secondary electron images of the microstructure of annealed WTaTiVCr after 24 hr at 1600°C

region, and the black interdendritic phase. It is clear that the black interdendritic phase is mostly Ti, with slight enrichment of V compared to the bright dendrite phase and roughly the same V content as the boundary region. It appears that Cr is most strongly enriched in the dark boundary region and is much more dilute in the bright dendrite and black interdendrite phases. Meanwhile, Ta appears mostly absent from the black interdendritic phase, but actually slightly depleted also at the interface between the bright dendrite and the boundary region, while Ti appears slightly enriched at that same location in the microstructure. W is clearly most concentrated in the bright dendrite phase, is much more dilute in the boundary region, and is effectively absent in the black Ti–rich dendrite phase.

5.3.2 1600°C, 24 hours

After the annealing at 1200°C did not show a significant evolution in the microstructure of the as–cast material, a sample was annealed for 24 hours at 1600°C, in order to explore whether such high temperature exposures could evolve the dendritic as–cast microstructure. Within the SEM images shown in Figure 5-10 the microstructure of the sample annealed at 1600°C and there does appear to be some evolution in the microstructure while remnants of the black interdendritic phase are still present. Although the dendritic microstructure is no longer fully intact a heterogeneous distribution of irregularly–shaped precipitates remain.

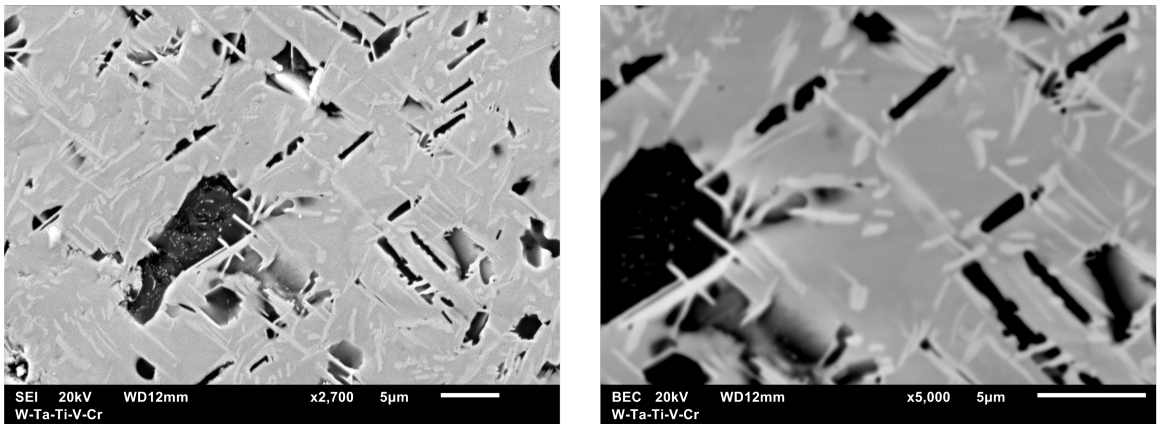

Figure 5-11: 2,700x (left) and 5,000x (right) SEM images of annealed WTaTiVCr after 24 hr at 1600°C. The SEM image on the left was collected in secondary electron mode while the SEM image on the right was collected in backscatter mode.

Higher magnification images of the annealed microstructure are presented in Figure 5-11. There appears to be a gray matrix phase, along with the irregular interdendritic phase precipitates. Now there also appears to be a high density of white precipitates that take a rod–like shape. These precipitates appear to have a preferred orientation as many are parallel. In addition, there are additional black precipitates that appear to take a disc–shape. It is unclear if this phase is distinct from the interdendritic phase or if it is the same phase of material. The rod–shape precipitates appear to penetrate from the matrix phase into the irregular–shaped interdendritic precipitates. Furthermore, this same phase also appears to be present to a certain extent at the interfaces between the matrix and black phase. Shown on the left side of Figure 5-12 is another backscatter SEM image of the annealed microstructure. This figure demonstrates the discontinuous network of the black interdendritic phase throughout the microstructure even after high temperature annealing. An EDX linescan showing the elemental distribution within the microstructure is included on the right side of Figure 5-12. We can observe that the black interdendritic phase is still rich in Ti while also including some V as well. The linescan shows that the matrix is rich in W, V, and Cr, while the bright rod–shaped and interfacial precipitate is clearly rich in Ta while also having some W and Cr, and V as well.

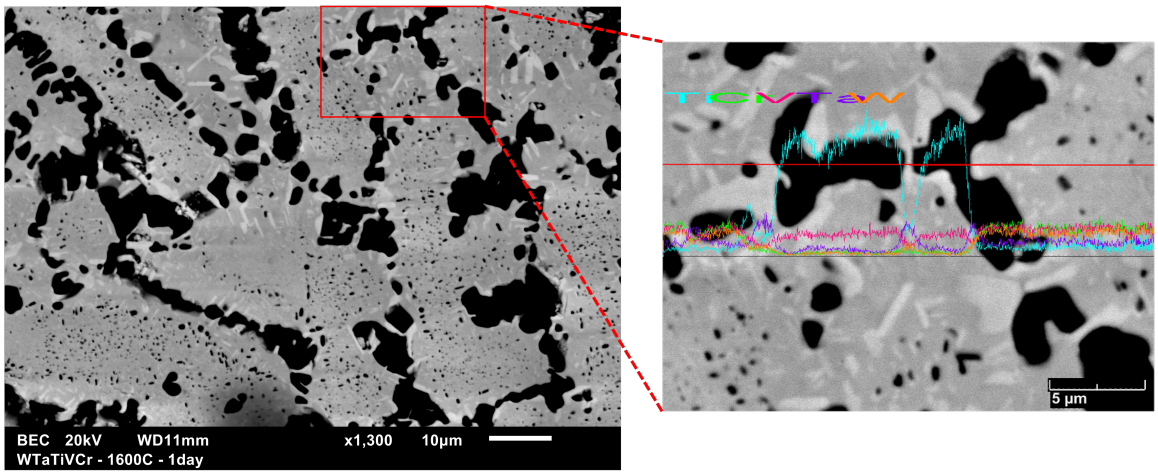

Figure 5-12: EDX linescan of the annealed microstructure showing the distribution of elements. The horizontal line indicates the linescan path. It is noteworthy that the black interdendritic phase is still rich in Ti with some V as well.

5.4 A $W_x(TaVTiCr)_y$ Low Entropy Alloy

In order to design an alloy within the W–Ta–V–Ti–Cr composition system more likely to form a single–phase microstructure, a non–equiatomic compositon was chosen such that the W content is very high. According to the atomistic mixing energy spectrum reported previously, it is clear that W has the most negative mixing energy, so therefore the expectation is that the mixing energy for the system should be increased by increasing the W content, thereby leading to a more likely single–phase composition. To explore this strategy, a W–rich composition of $W_{0.9}(TaVTiCr)_{0.1}$ was chosen. A 10 gram vacuum–pressed pellet of this composition was arc melted several times. The as–cast microstructure did not appear to be multiphase but there was some degree of heterogeneity in the microstructure, so the sample was annealed for 24 hours at 1600°C. A low–magnification SEM image of the annealed microstructure is shown in Figure 5-13. A homogeneous microstructure with large grains is present in the material and no precipitates are observed. This serves as a proof–of–principle in how the atomistic mixing energy can be used to design single–phase complex solid solution alloys, whether they are classified as low, medium, or high entropy. In this case, a

pseudo–binary approach was taken in which the content of the most negative mixing energy element, W in this case, was significantly increased while the molar fraction of all the rest of the components in the alloy were held equal.

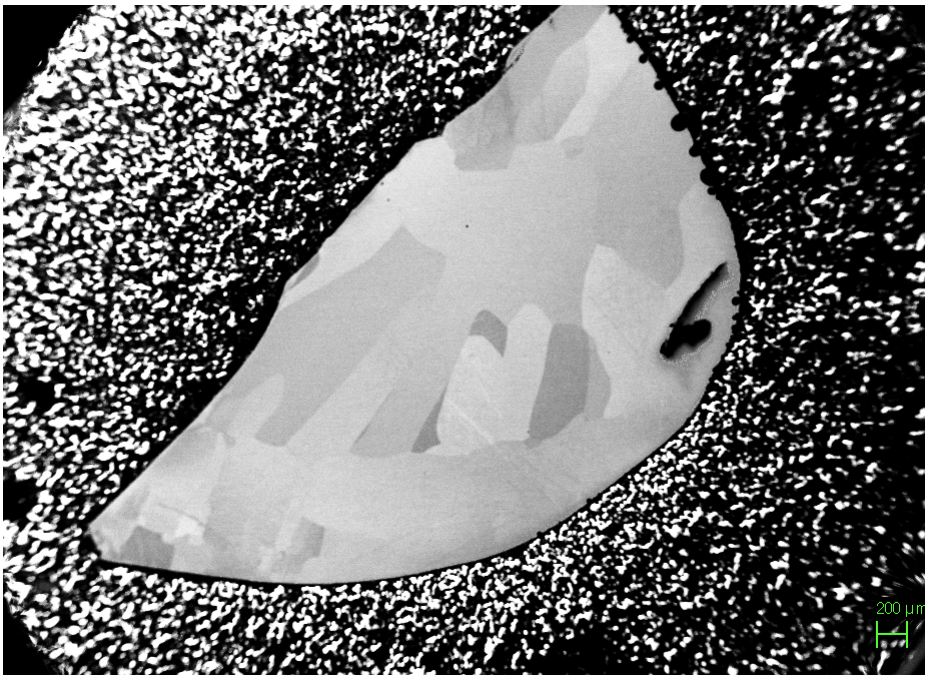

Figure 5-13: Annealed microstructure of the W–rich alloy

5.5 Discussion

In this section, I applied the atomistic model developed in chapter 3 to the W–Ta–V–Ti–Cr alloy system. The first–principles analysis indicated that W has a very strongly negative mixing energy in this system, while Ti has only a slightly negative mixing energy and Cr has some fraction of sites in the BCC SQS with positive mixing energy. Synthesis of the equimolar WTaVTiCr HEA by arc melting created a dendritic multi-phase microstructure with a dark Ti–rich phase. Previous reports of the WTaVTiCr equimolar HEA in the literaeture are limited to synthesis by spark–plasma sintering, which report a multiphase microstructure, with a TiC phase forming partially due to diffusion of carbon from the graphite sintering mold [80].

After discovering the multiphase microstructure of the as–cast equimolar HEA, high temperature annealing was performed in order to understand the evolution of the system at elevated temperature. After 24 hours of exposure in an inert atmosphere at 1200°C, the dendritic structure was still apparent in the microstructure, but some evolution in the elemental distribution was also present. A dark boundary region developed between the bright dendrites and the Ti–rich black interdendritic phase. EDX analysis reveals that this region of material is enriched in Cr, V, and slightly enriched in Ta. It is worth noting that this generally corresponds to the behavior indicated by the atomistic mixing energy analysis in that Cr is the element least thermodynamically favored for mixing, and this is also the element most segregated into the boundary region. So, while the atomistic mixing energy is useful for predicting likely phase stability, it can also give insights into likely segregation behavior at elevated temperatures in HEAs.

The sample microstructure for the equimolar HEA annealed at 1600°C for 24 hours displayed significant evolution. The Ti–rich interdendritic phase was still present, but there was also a distinct Ta–rich intermetallic phase forming throughout the material, including a high density of rod–shaped precipitates as well as precipitates formed preferentially at the interface between the W–rich matrix and the dark Ti–rich interdendritic phase. This complex microstructure is likely to reduce the ductility of the equimolar HEA although one would expect significant strengthening due to solid solution and precipitate hardening.

In order to work towards a derivative composition within the W–Ta–V–Ti–Cr system which forms a single–phase microstructure to avoid embrittlement, non–equimolar compositions were considered. The atomistic mixing energy analysis indicated that increasing the relative composition of W within the HEA should lead to stabilization of the BCC single–phase microstructure because of the strongly negative atomistic mixing energy of W. In order to explore this principle, a W–rich solid solution with molar composition of $W_{0.9}(TaVTiCr)_{0.1}$ was synthesized by arc melting. As opposed

to the equimolar HEA, this W–rich low entropy alloy derivative maintains a single–phase microstructure after casting and annealing at 1600°C including rather large grains. This demonstrates how the atomistic mixing energy analysis can be used to inuitively design non–equimolar compositions which are more likely to form single–phase microstructures.

This work also represents the first reports of the vacancy formation energy in the WTaVTiCr equimolar BCC HEA. The rule–of–mixing prediction of the vacancy formation energy works reasonably well, but there is a significant high energy tail, above the highest elemental vacancy formation energy. A pattern is emerging that the distribution of vacancy formation energies in refractory HEAs is broader than the range of elemental vacancy formation energies. The low energy tail of the vacancy formation energy distribution has previously been speculated in terms of so–called "deep trap" sites for vacancies, in which a low formation energy effectively immobilizes the vacancy and leads to a sluggish diffusion effect. While these results represent some support for this view, there is also a distinctive high energy tail which could be of equal importance. High formation energy sites should lead to particularly mobile vacancies in which there is a strong driving force for migration to a sink or to an interstitial for recombination. This could play an important role non–equilibrium processes such as radiation damage and contribute to the reported enhanced radiation damage tolerance of HEAs.

Chapter 6

Metallic Multilayer Composites

In this chapter, the focus will shift from HEAs to a different class of metallic materials, metallic multilayer composites (MMLCs). MMLCs are a subclass of functionally graded composites (FGC) consisting of separate metal layers which serve specific functionalities. Generally speaking, in this work the functionality between layers can be roughly broken down into (1) a layer that provides the necessary high temperature strength for the material, but is also resilient enough to radiation damage and (2) a layer which provides the material with significant resistance to environmental degradation (mostly corrosion) within the operating conditions of the nuclear reactor. In advanced nuclear energy systems this combination of properties is crucially important because the operating temperatures are significantly higher than current LWRs, and they often use highly corrosive coolants.

The specific focus of this chapter is on the effect of radiation damage at the interfacial region between different layers, called the bimetal interface. In particular, heavy ion irradiation is performed in order to create significant damage in the interfacial region in one MMLC tailored for fluoride molten salt applications, and another intended for lead and lead–bismuth eutectic (LBE) systems. Radiation–enhanced diffusion is identified in one of the MMLCs examined, while both display the formation of an interfacial Cr–rich phase, although it is not clear that this phase formation is driven primarily by radiation damage.

Composite materials appear to be ubiquitous in nature, especially functionally graded composites [82, 83]. A useful analogy to understand the separation of functionality in MMLCs is to relate the materials for a nuclear reactor to the shell of a turtle. The shell of a turtle consists of a strong backbone which supports the frame of the turle and the overall skeletal system, while the backbone is directly integrated with the larger bony shell of the turtle [84]. The analogy here is that we can imagine a general layer which needs to be robust against the volumetric degradation phenomena that materials undergo, namely high temperature, mechanical stress, and radiation damage by neutrons as the **backbone layer** of the MMLC. Meanwhile the **shell layer** serves as a corrosion–resistant layer protecting the material from environmental degradation.

In some cases the key layers of the MMLC are compatible and can be bonded together resulting in a bimetal composite, while in other cases it is necessary to include intermediate layers to facilitate metallurgical bonding between the backbone and shell layers. The use of composite materials in nuclear energy systems has existed for decades, most prominently in the form of the reactor pressure vessel (RPV), which is the single largest, most important component of a nuclear reactor and is the key pressure boundary of the system. In LWRs the thick, low–alloy steel vessel is utilized in order to provide the strength and tolerance to radiation damage, while a thin duplex stainless steel is utilized as a corrosion–resistant inner layer which is exposed to the corrosive coolant of the reactor [28, 85, 86]. The vessel low–alloy steel provides high strength and good resistance to radiation damage, much better than an austenitic stainless steel, while the corrosion–resistant cladding layer applied by the weld–overlay approach prevents corrosion that would rapidly degrade the low–alloy steel. Though the MMLC design principle has been successful in this case, application of this approach to materials for advanced nuclear energy systems has been limited.

6.1 MMLC Design

The design of novel MMLC concepts for advanced nuclear energy systems is relatively straightforward. Given the operating environment of the reactor, namely the coolant which is typically relatively corrosive, the operating temperature range, and the neutron flux and spectrum, the layers can be selected. The backbone layer should be selected primarily based upon having sufficient mechanical strength in the reactor operating temperature range, good radiation damage resistance up to the expected damage level in the reactor, and resistance to creep deformation in the reactor operating temperature range. The shell layer should be selected in order to provide the necessary corrosion resistance in the corrosive fluid present in the reactor over the operational temperature range of the reactor. Finally, some consideration of mutual compatibility between the layers should be considered. This could include factors such as the overall composition, the crystal structures of candidate layer materials, and the phase diagrams between primary components of the different layers.

One of the recent developments in MMLC designs for light water reactors is the significant interest in accident–tolerant fuels (ATF) in the wake of the 2011 nuclear accident at Fukushima Daiichi, Japan [87, 88]. In this case there is a significant advantage to systems engineers if the Zr steam oxidation reaction, which evolves hydrogen gas, can be avoided. Oxidation–resistant ferritic steels have been suggested as a possible solution by removing Zr from the system and replacing it with an advanced ferritic steel such as FeCrAl which contains multiple elements which tend to form protective oxide layers [89, 90]. The replacement of Zr with such a ferritic steel cladding tube would improve the oxidation–resistance of the fuel cladding in accident scenarios but it would significantly degrade the neutronic performance of the reactor. So, improvements would be made to the oxidation performance of the material most relevant to very low–probability severe accidents, while sacrificing the steady–state neutron economy of the reactor.

An alternative approach is the use of an MMLC design in which the majority of the thickness of the cladding tube is composed of Zr (or a Zr–base alloy such as Zircaloy–4) while the outer layer of the tubing is composed of an oxidation–resistant ferritic steel. In this way, the MMLC design approach has the potential to improve the severe accident oxidation behavior of the fuel cladding while having a smaller negative effect on the neutron economy of the reactor. Several approaches have been taken along this line, for instance coating the Zr fuel cladding with pure Cr, but directly bonding Zr with a ferritic steel poses an additional challenge [91]. Zr and Fe participate in a eutectic reaction with a eutectic temperature of 950°C, meaning that direct bonding between Zr fuel cladding and a ferritic steel would likely lead to melting along the interface of the material in the case of a severe accident. For this reason, intermediate layers would be necessary for a design in which the outer layer of the fuel cladding is a ferritic steel while the backbone layer is a Zr–base alloy.

Another practical consideration of MMLC design for advanced nuclear energy applications is regulatory. Specifically, there are few materials which have so far received regulatory approval for high temperature nuclear applications under the ASME Boiler & Pressure Vessel code, which is necessary for eventual commmercial adoption in the US. This process is expensive and time consuming, and it can take well more than a decade for materials to receive such regulatory approval. So, there is an additional motivation to utilize an already approved material (for instance, T91 steel or Incoloy 800H) as the structural backbone and use an MMLC approach to improve the lifetime performance of the material by limiting corrosion, which could greatly improve engineering outcomes while avoiding the need for a particularly time–consuming regulatory process.

The MMLC approach in principle provides a promising route to improve material performance by combining the beneficial properties of materials which are already known and characterized. In practice, high quality manufacturing and processing of such MMLCs in a scalable way can be challenging. Additionally, the use of an

MMLC approach guarantees the introduction of atleast one large bimetal interface into the system. This interface which is the surface over which the different layers are bonded could potentially be problematic. In general, interfaces can serve as "weak links" in material, and could serve as a stress concentration point especially if there is some degree of interfacial porosity. Also, interfaces provide a heterogeneity within the material which often makes nucleation and growth of precipitates more favored. Should a deleterious phase form along the interface, this could seriously degrade the overall material performance and lead to fracture or delamination. In this chapter, I focus on this interfacial region between the layers, and specifically on understanding the evolution of the interfacial structure under high temperature radiation damage.

6.2 MMLC for Fluoride Molten Salt Reactors

The first MMLC that I will focus on is a bimetal composite system with compatible FCC layers, one of which is a high temperature structural material and the shell layer is commercial–purity Ni (Ni–201). Previous studies have demonstrated that Ni–201 is effectively immune to corrosion in fluoride molten salts in comparison with other structural alloys such as 316L Stainless Steel, Incoloy 800H, and Hastelloy N [92]. It is worth noting that Hastelloy N is a costly Ni–base superalloy developed specifically for such high temperature nuclear applications in fluoride molten salt environments. One backbone material which could potentially be used for this MMLC is Incoloy 800H, a Fe–Ni–Cr solid solution alloy which has been developed over several decades and has been approved under the ASME Boiler and Pressure Vessel code for high temperature nuclear applications. Although this would provide significant regulatory advantages, Incoloy 800H is fundametally limited to approximately 700°C operating temperature due to susceptibility to creep deformation at elevated temperatures. In comparison, Haynes 230 has generally better high temperature strength and creep resistance compared to Incoloy 800H and could be used in operational temperatures up to 800°C. So, the MMLC design which will be the focus of this section of the thesis is a bimetal system of Haynes 230 and Ni–201.

Haynes 230 is a Ni–Cr–W alloy with W–rich precipitates dispersed in a FCC matrix. Although the material is not qualified in the same sense as Incoloy 800H, it has been demonstrated to have reasonable resistance to radiation damage at elevated temperatures [93]. Furthermore, with a Ni–base FCC matrix there is reason to believe in good compatibility with the Ni–201 shell layer. The corrosion of structural alloys in fluoride molten salts is largely dominated by Cr selective dissolution into the fluoride molten salt. So, not only does the Ni–201 shell layer provide resistance to corrosion, but also serves as a Cr diffusion barrier, limiting the transport of Cr to the metal/molten salt interface where selective dissolution of Cr can occur.

Although this MMLC design should combine high temperature strength and creep resistance, tolerance to radiation damage, and corrosion–resistance, little is known about the behavior of the interface in such a system and the effect of high temperature radiation damage. Specifically, the possibility of radiation–enhanced diffusion across the interface, and the enhanced transport of Cr across the interface associated with it could lead to degradation in the corrosion resistance. In order to understand the possible behavior of the interface under irradiation, an ion irradiation experiment was conducted to rapidly create damaged material to understand the interfacial radiation phenomena in a timely manner at the laboratory scale.

Self–ion irradiation was chosen in order to create a large degree of damage relatively quickly to emulate the effect of neutron–induced radiation damage. The use of ion irradiation has grown in popularity within the nuclear materials community to quickly emulate the radiation damage caused by neutrons while avoiding the need for a nuclear reactor to conduct irradiations. Protons have been used often for such radiation damage studies, and create a relatively large damaged region for examination, but there is obviously a necessary injection of hydrogen ions. Due to the presence of a bimetal interface in the irradiated region, protons were avoided to prevent any hydrogen bubble formation along the interface. Furthermore, using ions which cor-

respond to the primary element within the material (so–called self ions) causes the least amount of chemical evolution of the system due to the injected interstitials. The drawback of self ion irradiation is that these heavier ions have relatively less range within a given material, compared to protons, for the same incident energy so the damaged region of material for examination is smaller.

Because ions are electrically charged as compared to neutrons, the region of damage is only near the surface of the material upon which the ions were incident. In this study, the specific aim is to understand the behavior at the bimetal interface, which is within the internal part of the MMLC material. In order to cause damage at the interface by ion irradiation, the sample was sectioned and polished in a wedge shape. Doubly charged Ni ions were accelerated to 5 MeV to irradiate the interface of the material, as shown in the schematic diagram in Figure 6-1. The ion beam was aimed at the bimetal interface to ensure damage in the region of interest.

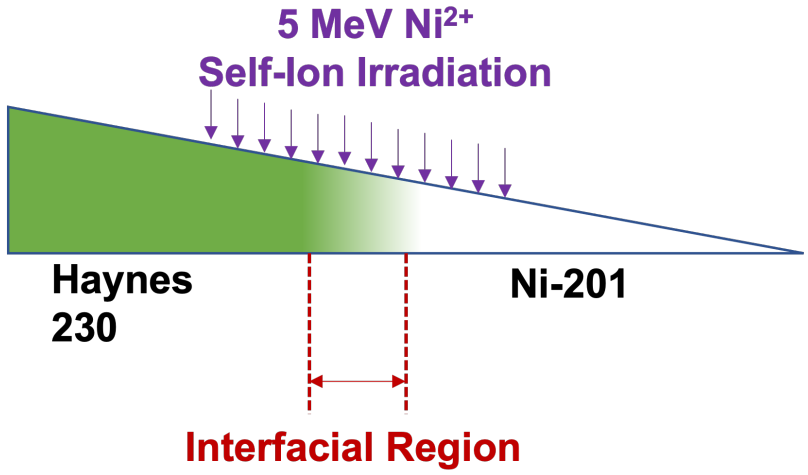

Figure 6-1: A schematic diagram of the ion irradiation of the Ni–base MMLC for fluoride molten salt applications.

A total fluence in the irradiated region of 5×10^{16} ions/cm^2 was achieved during a high temperature irradiation with a sample temperature of 700°C using the CLASS tandem

accelerator at MIT. The total fluence of the irradiation corresponds to a peak damage of approximately 10 displacements–per–atom (dpa), with the primary radiation damage being localized to the $\sim 1\mu$m region below the irradiated surface. Following irradiation, the sample was sectioned in order to expose a cross–section of the irradiated material for microstructural characterization. After careful sectioning and polishing, the material was examined using SEM as well as electron microprobe analysis (EMPA) as described in section B.3. A backscatter SEM image of the interfacial region is shown in Figure 6-2. The irradiated region of the material is demonstrated with the orange dashed line while the unirradiated region, 50 μm into the material from the irradiated surface, is shown in blue.

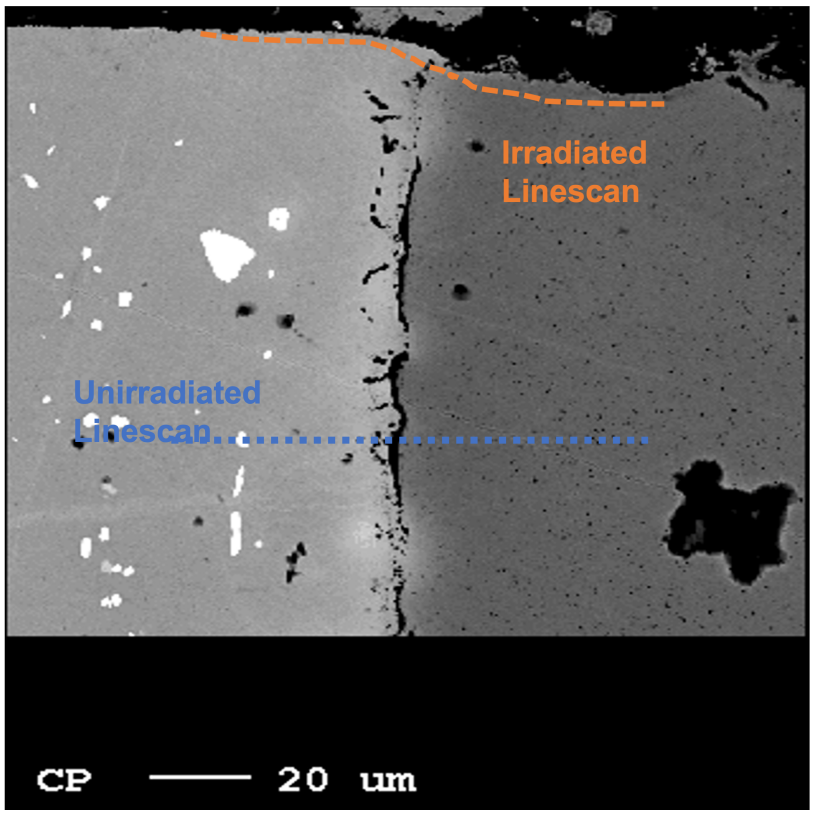

Figure 6-2: Backscatter SEM image of the Haynes 230/Ni–201 MMLC with linescan paths indicated on the image. The linescan path for the irradiated region is in orange while the unirradiated region 50 μm into the material is shown in blue.

EMPA linescan analysis along the linescan paths shown in Figure 6-2 was performed, and the results of the linescan are shown in Figure 6-3. The composition profile in the irradiated region is shown in orange while the unirradiated region is shown in blue. One of the most noticeable characteristics of the results shown here is the spike of Cr along the interface of the material. This interfacial enrichment of Cr is noticeable in both the irradiated and unirradiated regions. Another observation is the change in composition profile between the irradiated and unirradiated regions. For both the Ni and Cr profiles, there appears to be some degree of enhanced transport across the interface due to the relatively less steep composition profiles in the irradiated region, indicating a larger degree of interdiffusion of these elements in the irradiated region.

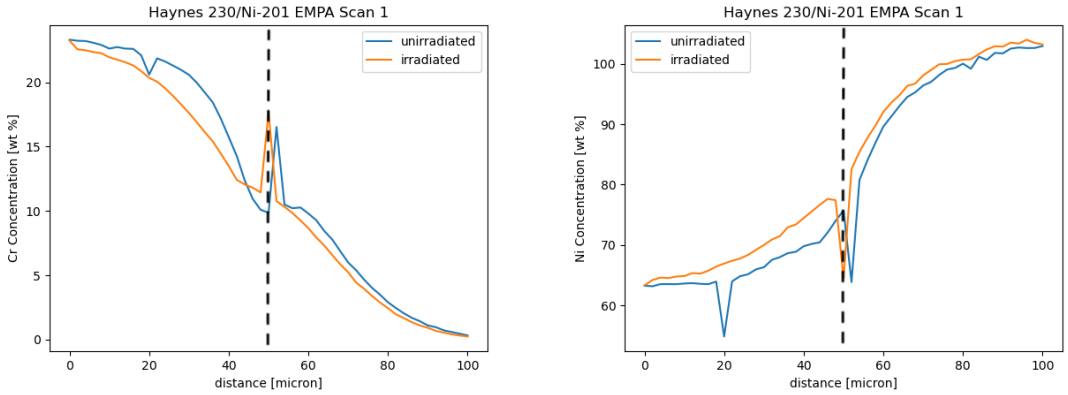

Figure 6-3: EMPA linescans of the Cr and Ni compositions in the irradiated and unirradiated regions of the material. The interface position is indicated with the black dashed vertical line.

In order to further understand the structure of the interfacial region after irradiation, an EMPA map was gathered. Because of the interfacial Cr enrichment along the interface adjacent to the irradiated region, C was included in the EMPA analysis to deduce whether this Cr–enrichment corresponds to the formation of a Cr–rich carbide phase such as $M_{23}C_6$. The results of the EMPA map data are displayed in Figure 6-4.

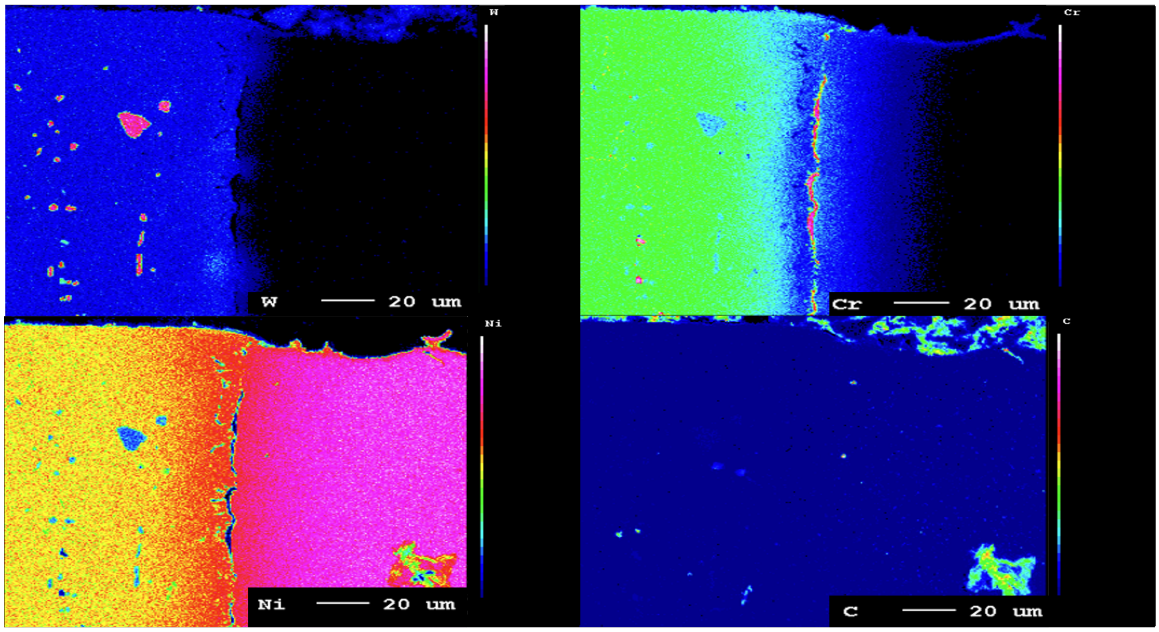

Figure 6-4: An EMPA map of the irradiated Haynes 230/Ni–201 irradiated MMLC.

The EMPA map results confirm the Cr enrichment along the interface, although there does not appear to be any degree of C enrichment coinciding with Cr, so it is reasonable to ascertain that the Cr–rich phase along the interface is not a carbide. The interfacial Cr–rich phase appears to extend along the length of the interface, and if anything appears less prevalent in the near–surface irradiated region, suggesting the possibility that radiation damage caused mixing of some of this Cr–rich phase. The Cr–rich phase could be a deleterious intermetallic such as σ phase, or could be BCC Cr. Examination of the Cr map in the near–surface region supports some degree of radiation–enhanced diffusive transport of Cr across the interface, but the extent of this enhanced transport seems relatively limited to the steep compositional gradient region around the interface, and does not appear likely to cause long–range transport of Cr which would decrease the corrosion–resistance of the Ni–201 layer. The composition gradient of Cr across the interface was 0.307 [wt.%/μm] in the unirradiated region while it was 0.295 [wt.%/μm] in the irradiated region, and the composition gradient of Ni across the interface was 0.551 [wt.%/μm] in the unirradiated region while it was 0.525 [wt.%/μm] in the irradiated region. This slight decrease in composition gradient

across the interface in the irradiated region suggests radiation enhances transport of Cr and Ni across the interface in this MMLC.

6.3 MMLC for Lead and Lead–Bismuth Reactors

Lead–Bismuth eutectic (LBE) is used as a coolant in several advanced fast reactor designs, but poses a significant challenge for materials. In particular, LBE is known to be highly corrosive to austenitic stainless steels in particular, as well as ferritic–martensitic steels. In previous work from MIT, a bimetal composite consisting of T91 as the backbone layer, with Fe–12Cr–2Si as the shell layer was developed for service in LBE systems [94]. Fe–12Cr–2Si forms a particularly protective passive oxide layer in LBE due to the presence of multiple oxide formers (Cr and Si), similar in principle to other oxidation–resistant ferritic steels such as Fe–Cr–Al. T91 is already approved for high temperature nuclear applications under the ASME RPV code. T91 is quite resistant to radiation damage up to a high damage level ($\sim$ 100 dpa) and has good high temperature mechanical strength, but above 600°C the creep resistance of T91 degrades substantially.

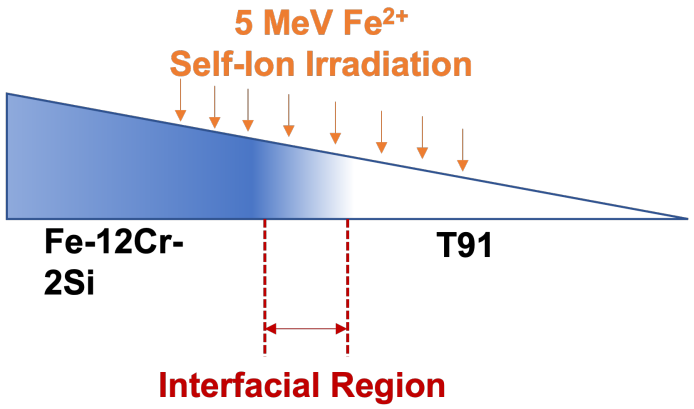

Figure 6-5: A schematic diagram of the T91/Fe–12Cr–2Si MMLC interfacial irradiation

The T91/Fe–12Cr–2Si bimetal composite system has been developed and demonstrated to be serviceable in high temperature LBE environments, but the effect of radiation damage on the bimetal interface is unknown. In order to understand the radiation damage effects in the interfacial region, an ion irradiation experiment was performed in a similar fashion to the previous section. In this case the self ions utilized in the ion irradiation were Fe ions because both metal layers in the composite are Fe–base systems. A schematic diagram of the ion irradiation is shown in Figure 6-5.

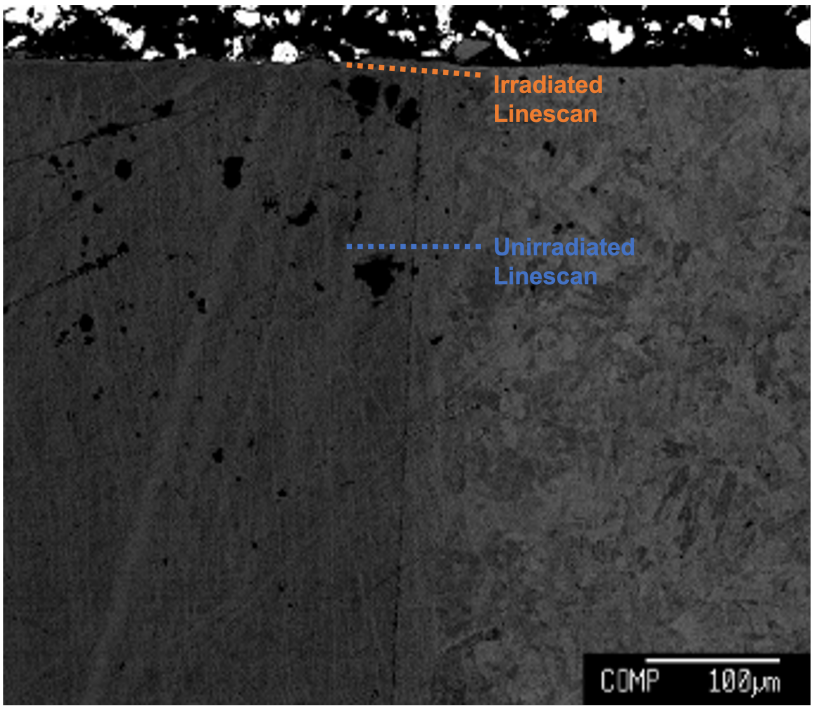

Figure 6-6: Backscatter electron image of the T91/Fe–12Cr–2Si interfacial region and EMPA analysis paths.

Fe ions accelerated to 5 MeV were directed at the interfacial region of material, and the irradiation was conducted until a fluence of 5×10^{16} ions/cm^2 was reached. This irradiation was conducted at a sample temperature of 700°C and a peak damage of approximately 10 dpa was reached, with the primary radiation damage being localized to the $\sim 1\mu$m layer adjacent to the irradiated surface. After irradiation the sample

was sectioned and carefully polished for microstructural characterization of the irradiated cross–section. The composition profile of the elements was measured using EMPA, as described in section B.3. Figure 6-6 shows a backscatter SEM image of the irradiated cross–section, along with the linescan path for the irradiated (orange) and unirradiated regions (blue).

The results of the EMPA linescan analysis are displayed in Figure 6-7. Similar to the results for the irradiated Haynes 230/Ni–201 MMLC, there appears to be a significant enrichment of Cr along the bimetal interface. Si shows quite similar profiles for the irradiated and unirradiated regions, but there does appear to be some slight segregation away from the bimetal interface. Fe shows depletion along the interface (corresponding to the Cr enrichment), while the shape of the curves for the unirradiated and irradiated region are quite similar. It is worth noting that the Fe concentration profile along the linescan path in the irradiated region is approximately 0.5 wt. % higher than the unirradiated region, while for Cr the profile in the irradiated region is approximately 0.5 wt. % lower than the unirradiated region along the same location in the linescan. This could potentially be due to some degree of radiation–induced segregation perpendicular to the irradiated surface.

As with the previous irradiated MMLC, there appears to be significant Cr enrichment along the bimetal interface. In order to understand this behavior in more detail, an EMPA map was measured with particular attention paid to the C content along the interface. The EMPA map for the irradiated T91/Fe–12Cr–2Si MMLC is shown in Figure 6-8. The C map reveals that there is some Cr enrichment along the interface (likely carbide precipitates), but these do not extend to the irradiated near–surface region, and furthermore the Cr enrichment is much more widespread along the interface, indicating that Cr–rich carbide formation is likely contributing to the Cr found at the interface but cannot entirely explain the results of the elemental analysis.

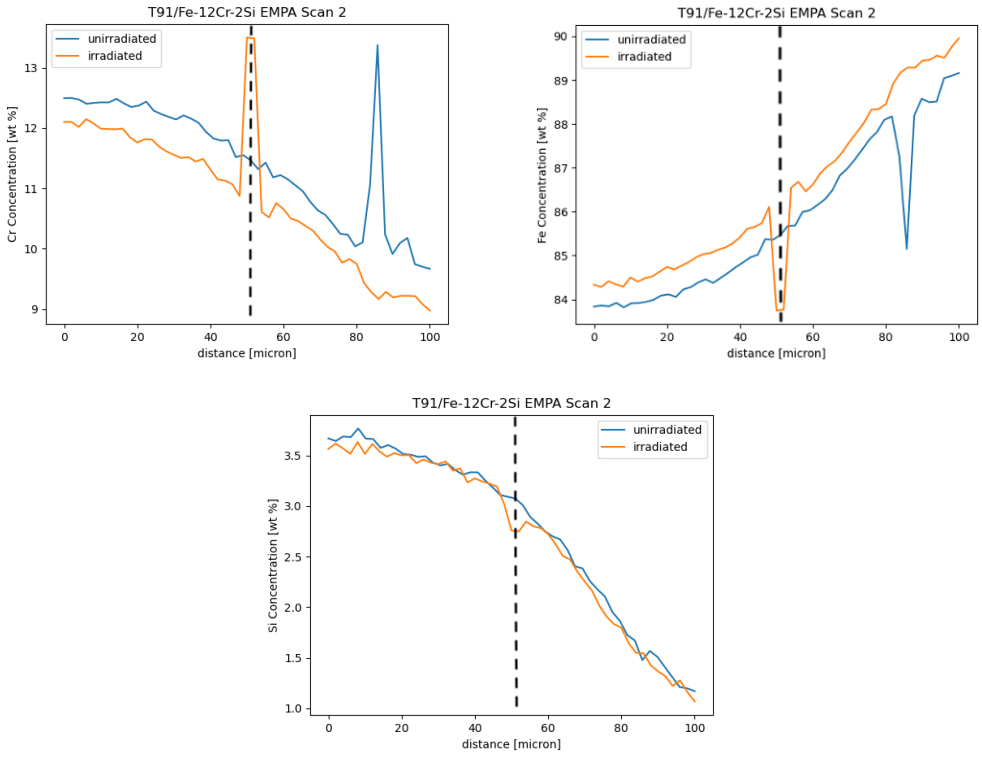

Figure 6-7: The EMPA linescans for Cr, Fe, and Si within the irradiated and unirradiated regions of the T91/Fe–12Cr–2Si MMLC. The interface position is indicated with the black dashed vertical line.

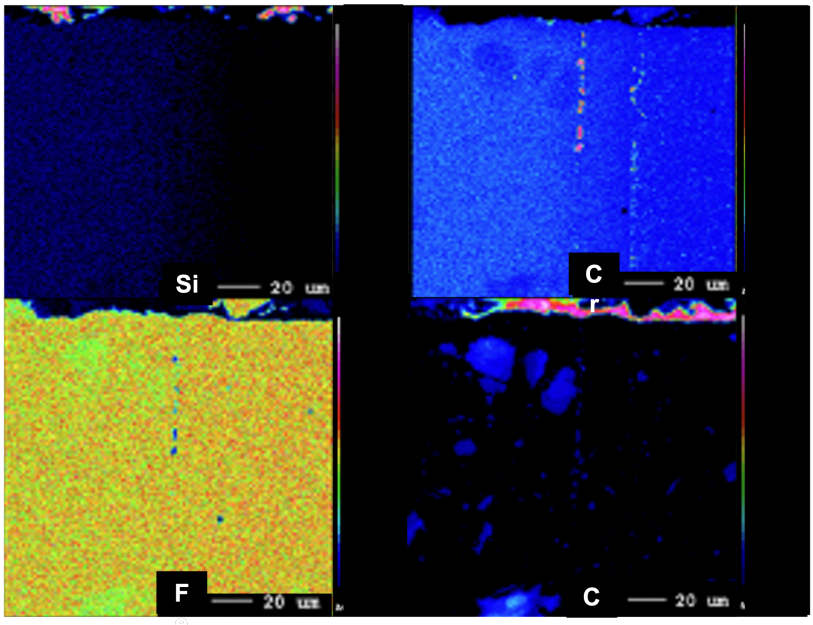

Figure 6-8: The EMPA map results of the irradiated T91/Fe–12Cr–2Si MMLC sample.

6.4 Discussion

In this chapter, I focus on MMLCs relevant to advanced nuclear energy systems, one FCC Ni–base system (Haynes 230/Ni–201) and one ferritic–martensitic steel based system (T91/Fe–12Cr–2Si) and specifically focus on interfacial ion irradiation to understand the applicability of the MMLC design concept to advanced nuclear energy systems. Both MMLCs were irradiated to 10 dpa peak damage at 700°C irradiation temperature. EMPA compositional analysis was conducted on both samples, including linescans in irradiated and unirradiated regions, along with elemental maps. In both of the systems studied here, the compositional analysis reveals Cr enrichment along the bimetal interface of the materials.

In the irradiated Ni–base Haynes 230/Ni–201 MMLC, there was a notable Cr–rich phase formed along the bimetal interface between Ni–201 and Haynes 230. Along with Cr enrichment along the bimetal interface, there was radiation–enhanced diffusion observed between Ni and Cr within the interfacial region. Because the Ni–base MMLC is intended for applications in fluoride molten salt reactors. and corrosion in such fluoride molten salt systems is dominated by selective dissolution of Cr, radiation–enhanced diffusion could reduce the corrosion resistance imparted by the Ni–201 shell layer or require a thicker shell layer to counteract this effect. Elemental analysis of C within the material confirmed that the Cr–rich phase formed along the interface was not a Cr–rich carbide. Although more detailed analysis is required to characterize the interface, it appears possible that this could be a σ phase or BCC Cr, which are known to be relatively brittle and are likely to degrade the ductility of the MMLC.

In the irradiated steel MMLC for LBE applications, some similarities and differences were observed. There was a similar Cr interfacial enrichment observed, but in the case of T91/Fe–12Cr–2Si there were some carbides present at the interface, although not enough to fully account for the Cr enrichment observed. There does not appear to be a significant radiation–enhanced diffusion effect in the T91/Fe–12Cr–2Si, in

contrast to the Ni–Cr pair within the Haynes 230/Ni–201 MMLC. One observation is that in the Haynes 230/Ni–201 composite, the compositional gradient across the interface is quite steep. For instance, the Cr content in Haynes 230 is 22 wt % while it is zero in Ni–201, and the Ni content in Haynes 230 is 57 wt % while in Ni–201 the Ni content is greater that 99 wt %. On the other hand, in the T91/Fe–12Cr–2Si MMLC the compositional gradients across the interface are quite gradual. The Cr content in T91 is 9 wt % while it is 12 wt % in Fe–12Cr–2Si, and the Fe content in T91 is approximately 90 wt % while it is approximately 86 wt % in Fe–12Cr–2Si. It is likely that the larger composition gradient across the interface leads to a more clearly observable radiation–enhanced diffusion effect in the Haynes 230/Ni–201 MMLC.

For future MMLC applications in advanced nuclear energy systems, precipitation of deleterious phases at the interface between the layers is a bigger cause for concern than radiation–enhanced diffusion due to the possibility these phases could lead to fracture or other catastrophic failure for the material. A smaller length scale microstructural analysis and characterization of the interface (such as with transmission electron microscopy) is required to determine the exact nature of this Cr–rich precipitate, and it is worth exploring the effect of the pre–existing microstructure and MMLC manufacturing method on the precipitation of such interfacial phases. For instance, alternative manufacturing methods besides diffusion bonding, namely weld overlay, cold spray, or other additive manufacturing techniques could be utilized and tested in a similar way to the work presented here to understand if this phenomena is inherent to layered MMLCs or if it can be suppressed through microstructure control. Using advanced additive manufacturing approaches such as laser–engineered net shaping [95, 96], more fine spatial control of the concentration is possible, which may be able to mitigate interfacial phase formation.

Chapter 7

Conclusion and Future Directions

In this thesis, I aimed to address significant open questions in the field of structural materials design for advanced nuclear energy systems. I specifically focus on two classes of materials design approaches: high entropy alloys and metallic multilayer composites. In some ways these two design approaches are antithetical. In HEAs, many different elements are mixed together into a highly disordered alloy with the ultimate intent of a material which has properties far surpassing the properties of the different elements constituting the alloy. In contrast the MMLC approach is to partition the material into different layers with specific intended functionalities. Namely, I put forward a mental model analogizing MMLC design to a turtle skeletal structure, with a backbone layer which provides the mechanical strength and tolerance to radiation damage required of the material, and a shell layer with the function of resisting corrosion and protecting the underlying backbone material.

I focus on an open question surrounding both of these approaches in order to pave the way for development of advanced nuclear energy through improved material performance. In HEAs I focus on the question of how to determine which elements to include in the HEA that will be most likely to form a single–phase microstructure. In MMLCs, I aim to understand the effect of the interface separating layers and the behavior of this interfacial region under irradiation by using self–ion irradiation.

Major Contributions

I consider the major contributions of this thesis work to be:

- I develop the atomistic mixing energy as a quantity to determine the site and element–specific driving force for mixing of different elements within an HEA, as well as the approach to determine this quantity for a solid solution of arbitrary composition and complexity
- I apply this model to analyze the thermodynamic behavior of 5 different refractory HEA compositons: NbMoTaTiV, NbMoTaTiW, NbMoTaTiZr, NbMoTaHfW, and WTaVTiCr. I identify a positive mixing energy as characteristic of elements which will tend to precipitate out of a solid solution alloy, while trends in atomistic mixing energy are tied to the segregation behavior of the alloy.
- I synthesize and characterize these 5 HEAs using the arc melting approach in order to test the predictions of the model I developed, in addition to high temperature annealing.
- Using the model, I calculate the vacancy formation energy distribution in the 5 HEA systems listed above
- In general I find that the VFE distribution in HEAs often spans a wider range than the range of VFEs between the pure elemental components of the HEA
- A high VFE tail was identified in the HEAs and it is speculated that this could contribute to the reported superior radiation damage performance of HEAs
- I work to develop 2 different MMLCs relevant to advanced nuclear energy systems and use ion irradiation at 700°C to 10 dpa to understand radiation damage at the interfacial region between layers
- I identify an interfacial Cr enrichment in both systems, which could degrade the mechanical properties of the MMLCs, while this phase formation may not be driven solely by radiation

- Radiation–enhanced diffusion was observed in one MMLC but not the other, and it is speculated that the tendency for radiation–enhanced diffusion between layers is connected to the composition gradients across the MMLC interface

Future Research Directions

Although this thesis represents a significant step forward in the development of structural materials for advanced nuclear energy systems, there remain several research directions I believe should be fruitful paths forward for structural materials development.

Non–Equimolar Solid Solution Alloys

In this thesis, only equimolar HEAs were directly analyzed using the atomistic mixing energy approach I have developed. In the future, an interesting and obvious next area of inquiry is implementing the atomistic mixing energy analysis for non–equimolar solid solution alloys such as the $W_x(TaVTiCr)_{1-x}$ alloys explored in the previous chapter. I intend to develop relevant SQS supercells to represent different compositions within the $W_x(TaVTiCr)_{1-x}$, starting from the 90% W alloy synthesized in the previous chapter in order to understand the variation of atomistic mixing energy of different elemental components of the HEA across different alloy compositions in order to understand the effect of composition within this specific system.

Atomistic Design of Ductile Refractory HEAs

Within the world of refractory HEAs I have explored in this thesis, one major concern is the ductility of the HEA. Although one refractory system (the so–called Senkov alloy) has been found to have reasonable ductility at room temperature, I believe that a promising future direction is to combine the atomistic mixing energy modeling here with a focus on ductile alloy development. One approach has recently developed to create refractory HEAs with intrinsic ductility based on valence electron concentration

of the constituent elements, with the authors suggesting a valence electron concentration (VEC) below 4.5 for intrinsic ductility [73]. Other methods have been developed which facilitate calculation of parameters characterizing the intrinsic ductility of solid solution alloys based on second and third–order elastic constants [97, 98], which can be obtained from atomistic first–principles calculations similar to those performed to obtain the atomistic mixing energy in this work. Furthermore, atomistic simulations have been applied to higher–order defects such as dislocations within refractory HEAs [99], which govern plasticity and the temperature–dependence of strength in these systems. This, coupled with thermodynamic mixing insights could facilitate the design of HEAs (including non–equimolar systems) which favor single–phase stability while also maintaining strength and ductility, which is a central goal within the field of metallurgy. Additionally, this could be coupled with the low–activation refractory HEA approach discussed previously to enable alloys with superior mechanical properties which will also be favored for applications in nuclear energy systems.

Defects and Defect Dynamics in HEAs

One major area of interest which this thesis work shed light upon is the behavior of defects in HEAs, namely the behavior of vacancies. In addition to the formation energy, an important quantity determining system behavior is the vacancy migration energy, or in the case of HEAs the distribution of vacancy migration energies. Although I speculated previously in this thesis about the connection between the high energy tail of the vacancy formation and enhanced mobility of those vacancies (especially in the case of radiation damage) the migration barrier can be determined computationally by applying algorithms such as the climbing image nudged elastic band (CI–NEB) [100, 101]. Establishing the distribution of vacancy migration energies in HEAs and the correlation (or lack there of) between the formation energy and migration energy could provide important insights into the physical mechanisms that enhanced radiation damage tolerance in HEAs. Finally, defect clustering between vacancies [102], and intersitial behavior will be critical for elucidating the behavior of HEAs under radiation damage.

MMLC Development for Nuclear Energy

For MMLCs, this thesis has shed light on potentially problematic microstructural evolution that certainly needs to be explored further to understand whether or not MMLCs should be widely adopted for advanced nuclear energy systems. First, a more detailed smaller length scale characterization campaign is planned for the ion irradiated MMLCs reported in this work. Specifically, I intend to irradiate MMLC samples polished with a much larger wedge angle in order to create a large amount of interfacial irradiated area for more detailed material characterization of the damaged region. Elucidation of the nature of the interfacial phases formed in this work, in addition to similar irradiation testing conducted on MMLCs manufactured using different techniques besides diffusion bonding, such as weld overlay and additive manufacturing could help understand the effect of pre–existing microstructure on interfacial phase formation.

Appendix A

Computational Methodology

A.1 Sequential Quasirandom Structures (SQS)

The use of SQS supercells is a key characteristic of HEA atomistic simulations employed in this thesis. In order to model the fundamentally disordered nature of complex solid solution alloys, we employ the sequential quasirandom structure approach first developed by Zunger in 1990 [103]. This approach allows us to create a supercell in which the pair distribution functions are matched to the random state as closely as possible. The SQS method has been shown to accurately predict the properties of disordered solids with supercells as small as 16 atoms [104–108]. Distinct 30 atom SQS supercells for both alloys were produced using the `mcsqs` code within the Alloy Theoretic Automated Toolkit [109, 110].

The VASP POSCAR input for the 30 atom SQS I developed is shown below, with `xxx` indicating the lattice parameter and A–B–C–D–E being the elemental components of the HEA:

```
POSCAR 30 atom SQS
xxx
   0.00000000   0.00000000   2.00000000
   2.50000000   0.50000000   0.50000000
```

```
   0.00000000   3.00000000   1.00000000
    A    B    C    D    E
    6    6    6    6    6
Direct
   1.00000000   1.00000000   1.00000000
   0.83333333   1.00000000   0.33333333
   0.10000000   0.40000000   0.60000000
   0.20000000   0.80000000   0.20000000
   0.80000000   0.20000000   0.80000000
   0.93333333   0.40000000   0.93333333
   0.50000000   1.00000000   1.00000000
   0.33333333   1.00000000   0.33333333
   0.46666667   0.20000000   0.46666667
   0.23333333   0.60000000   0.73333333
   0.73333333   0.60000000   0.73333333
   0.86666667   0.80000000   0.86666667
   0.13333333   0.20000000   0.13333333
   0.63333333   0.20000000   0.13333333
   0.66666667   1.00000000   0.66666667
   0.76666667   0.40000000   0.26666667
   0.40000000   0.60000000   0.40000000
   0.60000000   0.40000000   0.60000000
   0.16666667   1.00000000   0.66666667
   0.26666667   0.40000000   0.26666667
   0.30000000   0.20000000   0.80000000
   0.90000000   0.60000000   0.40000000
   0.53333333   0.80000000   0.53333333
   0.36666667   0.80000000   0.86666667
   0.06666667   0.60000000   0.06666667
   0.56666667   0.60000000   0.06666667
```

0.96666667 0.20000000 0.46666667
0.70000000 0.80000000 0.20000000
0.03333333 0.80000000 0.53333333
0.43333333 0.40000000 0.93333333

A.2 NbMoTaTiW Vacancy Exchange Potential

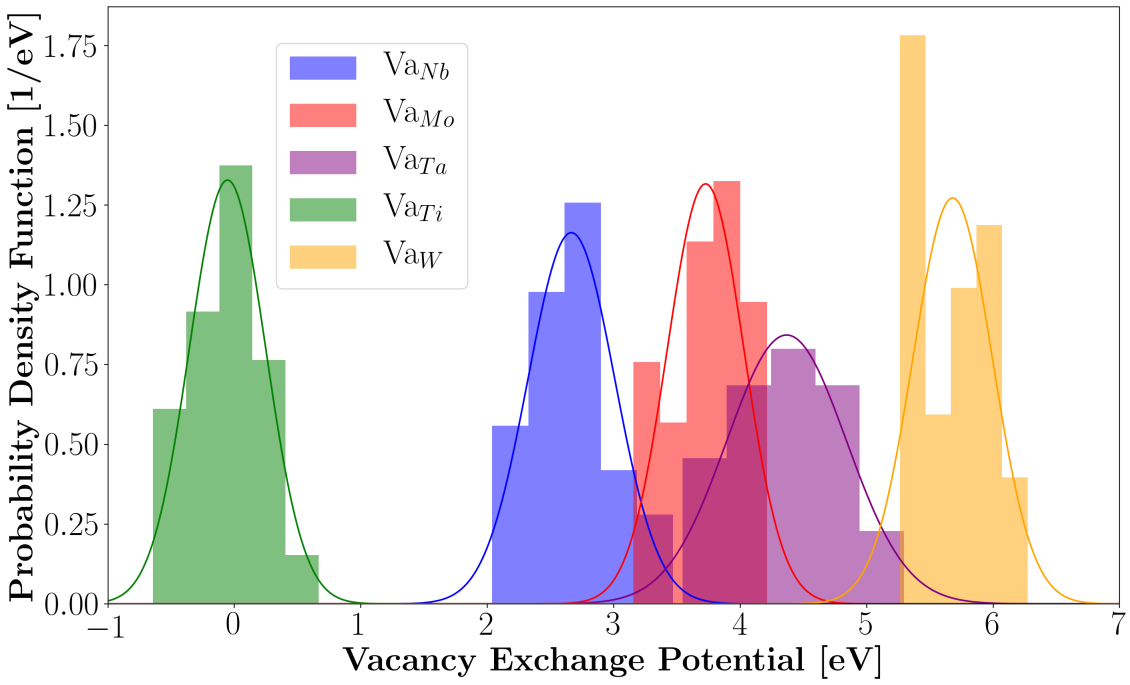

Figure A-1: Vacancy exchange potential distribution for 125–atom NbMoTaTiW SQS

A.3 First–Principles Calculations

All of the first–principles calculations were performed through the plane–wave density functional theory (DFT) approach which is well–established for use in solid materials and provides a method to obtain the thermodynamic properties of the HEAs without the need for initial experimental data. All calculations were done using the Vienne Ab-initio Simulation Package (VASP) which is a widely utilized and well–validated

DFT code [111, 112]. The Projector–Augmented Wave (PAW) pseudopotentials were used for each element in the system to describe the ion–electron interactions in the DFT calculations [113, 114].

Various simulation inputs, outputs, and processed data can be found within the Zenodo repository [115]. An example of a VASP INCAR is shown below:

```
SYSTEM = HEA SQS
ICHARG = 2
ENCUT = 400
ISMEAR = 1
SIGMA = 0.2
NPAR = 4
KPAR = 16
IBRION = 2
POTIM = 0.1
ISIF = 2
ISYM = 0
NSW = 100
LREAL = Auto
IALGO = 38
GGA = PS
```

An example of a bash script used to generate all the swap and vacancy inputs for the atomistic mixing energy analysis of a 125–atom, 5–component SQS is shown below:

```
for SITE in {1..125}
do
   LineSep=8
   Line=$(($SITE+$LineSep))

   Type1=$((1+$LineSep))
```

```
Type2=$((26+$LineSep))
Type3=$((51+$LineSep))
Type4=$((76+$LineSep))
Type5=$((101+$LineSep))



mkdir site${SITE}
cd site$SITE



cp ../POSCAR ./
cp ../POTCAR ./
cp ../INCAR ./
cp ../KPOINTS ./
cp ../sqs125.slurm ./site${SITE}.slurm

# TYPE 1-------------------------------------------------------------------------
if [ $SITE -ge 1 ] && [ $SITE -le 25 ]; then
   mkdir vacancy
   cd vacancy
   awk 'NR==7 {$0=" 24  25  25  25  25"} 1' ../POSCAR > ./POSCAR
   sed -i "${Line}d" POSCAR
   cp ../POTCAR ./
   cp ../INCAR ./
   cp ../KPOINTS ./
   cp ../site${SITE}.slurm ./st${SITE}-vac.slurm
   sbatch st*
   cd ..
```

```
    mkdir swap2
    cd swap2
    Type=$Type2
    awk 'NR==7 {$0=" 24  26  25  25  25"} 1' ../POSCAR > ./POSCAR
    atom=$(sed "${Line}q;d" POSCAR)
    sed -i "${Type2}i\ $atom" POSCAR
    if (("$Line" > "$Type")); then linenum=$(( $Line + 1 )); else linenum=
fi
    sed -i "${linenum}d" POSCAR
    cp ../POTCAR ./
    cp ../INCAR ./
    cp ../KPOINTS ./
    cp ../site${SITE}.slurm ./st${SITE}-sw2.slurm
    sbatch st*
    cd ..

    mkdir swap3
    cd swap3
    Type=$Type3
    awk 'NR==7 {$0=" 24  25  26  25  25"} 1' ../POSCAR > ./POSCAR
    atom=$(sed "${Line}q;d" POSCAR)
    sed -i "${Type3}i\ $atom" POSCAR
    if (("$Line" > "$Type")); then linenum=$(( $Line + 1 )); else linenum=
fi
    sed -i "${linenum}d" POSCAR
    cp    ../POTCAR ./
    cp    ../INCAR ./
    cp ../KPOINTS ./
    cp    ../site${SITE}.slurm ./st${SITE}-sw3.slurm
    sbatch st*
```

```
    cd      ..

    mkdir swap4
    cd      swap4
    Type=$Type4
    awk 'NR==7 {$0=" 24   25   25   26   25"} 1' ../POSCAR > ./POSCAR
    atom=$(sed "${Line}q;d" POSCAR)
    sed -i "${Type4}i\ $atom" POSCAR
    if (("$Line" > "$Type")); then linenum=$(( $Line + 1 )); else linenum=
fi
    sed -i "${linenum}d" POSCAR
    cp ../POTCAR ./
    cp ../INCAR ./
    cp ../KPOINTS ./
    cp ../site${SITE}.slurm ./st${SITE}-sw4.slurm
    sbatch st*
    cd ..

    mkdir swap5
    cd      swap5
    Type=$Type5
    awk 'NR==7 {$0=" 24   25   25   25   26"} 1' ../POSCAR > ./POSCAR
    atom=$(sed "${Line}q;d" POSCAR)
    sed -i "${Type5}i\ $atom" POSCAR
    if (("$Line" > "$Type")); then linenum=$(( $Line + 1 )); else linenum=
fi
    sed -i "${linenum}d" POSCAR
    cp ../POTCAR ./
    cp ../INCAR ./
    cp ../KPOINTS ./
```

```
    cp ../site${SITE}.slurm ./st${SITE}-sw5.slurm
    sbatch st*
    cd ..
# TYPE 2 ------------------------------------------------------------------
  elif [ $SITE -ge 26 ] && [ $SITE -le 50 ]; then
    mkdir vacancy
    cd vacancy
    awk 'NR==7 {$0=" 25  24  25  25  25"} 1' ../POSCAR > ./POSCAR
    sed -i "${Line}d" POSCAR
    cp ../POTCAR ./
    cp ../INCAR ./
    cp ../KPOINTS ./
    cp ../site${SITE}.slurm ./st${SITE}-vac.slurm
    sbatch st*
    cd ..

    mkdir swap1
    cd swap1
    Type=$Type1
    awk 'NR==7 {$0=" 26  24  25  25  25"} 1' ../POSCAR > ./POSCAR
    atom=$(sed "${Line}q;d" POSCAR)
    sed -i "${Type1}i\ $atom" POSCAR
    if (("$Line" > "$Type")); then linenum=$(( $Line + 1 )); else linenum=
fi
    sed -i "${linenum}d" POSCAR
    cp ../POTCAR ./
    cp ../INCAR ./
    cp ../KPOINTS ./
    cp ../site${SITE}.slurm ./st${SITE}-sw1.slurm
    sbatch st*
```

```
    cd ..

    mkdir swap3
    cd swap3
    Type=$Type3
    awk 'NR==7 {$0=" 25  24  26  25  25"} 1' ../POSCAR > ./POSCAR
    atom=$(sed "${Line}q;d" POSCAR)
    sed -i "${Type3}i\ $atom" POSCAR
    if (("$Line" > "$Type")); then linenum=$(( $Line + 1 )); else linenum=
fi
    sed -i "${linenum}d" POSCAR
    cp ../POTCAR ./
    cp ../INCAR ./
    cp ../KPOINTS ./
    cp ../site${SITE}.slurm ./st${SITE}-sw3.slurm
    sbatch st*
    cd ..

    mkdir swap4
    cd swap4
    Type=$Type4
    awk 'NR==7 {$0=" 25  24  25  26  25"} 1' ../POSCAR > ./POSCAR
    atom=$(sed "${Line}q;d" POSCAR)
    sed -i "${Type4}i\ $atom" POSCAR
    if (("$Line" > "$Type")); then linenum=$(( $Line + 1 )); else linenum=
fi
    sed -i "${linenum}d" POSCAR
    cp ../POTCAR ./
    cp ../INCAR ./
    cp ../KPOINTS ./
```

```
    cp ../site${SITE}.slurm ./st${SITE}-sw4.slurm
    sbatch st*
    cd ..

    mkdir swap5
    cd swap5
    Type=$Type5
    awk 'NR==7 {$0=" 25  24  25  25  26"} 1' ../POSCAR > ./POSCAR
    atom=$(sed "${Line}q;d" POSCAR)
    sed -i "${Type5}i\ $atom" POSCAR
    if (("$Line" > "$Type")); then linenum=$(( $Line + 1 )); else linenum=
fi
    sed -i "${linenum}d" POSCAR
    cp ../POTCAR ./
    cp ../INCAR ./
    cp ../KPOINTS ./
    cp ../site${SITE}.slurm ./st${SITE}-sw5.slurm
    sbatch st*
    cd ..

# TYPE 3 ------------------------------------------------------------------
  elif [ $SITE -ge 51 ] && [ $SITE -le 75 ]; then
    mkdir vacancy
    cd vacancy
    awk 'NR==7 {$0=" 25  25  24  25  25"} 1' ../POSCAR > ./POSCAR
    sed -i "${Line}d" POSCAR
    cp ../POTCAR ./
    cp ../INCAR ./
    cp ../KPOINTS ./
    cp ../site${SITE}.slurm ./st${SITE}-vac.slurm
```

```
    sbatch st*
    cd ..

    mkdir swap1
    cd swap1
    Type=$Type1
    awk 'NR==7 {$0=" 26  25  24  25  25"} 1' ../POSCAR > ./POSCAR
    atom=$(sed "${Line}q;d" POSCAR)
    sed -i "${Type1}i\ $atom" POSCAR
    if (("$Line" > "$Type")); then linenum=$(( $Line + 1 )); else linenum=
fi
    sed -i "${linenum}d" POSCAR
    cp ../POTCAR ./
    cp ../INCAR ./
    cp ../KPOINTS ./
    cp ../site${SITE}.slurm ./st${SITE}-sw1.slurm
    sbatch st*
    cd ..

    mkdir swap2
    cd swap2
    Type=$Type2
    awk 'NR==7 {$0=" 25  26  24  25  25"} 1' ../POSCAR > ./POSCAR
    atom=$(sed "${Line}q;d" POSCAR)
    sed -i "${Type2}i\ $atom" POSCAR
    if (("$Line" > "$Type")); then linenum=$(( $Line + 1 )); else linenum=
fi
    sed -i "${linenum}d" POSCAR
    cp ../POTCAR ./
    cp ../INCAR ./
```

```
    cp ../KPOINTS ./
    cp ../site${SITE}.slurm ./st${SITE}-sw2.slurm
    sbatch st*
    cd ..

    mkdir swap4
    cd swap4
    Type=$Type4
    awk 'NR==7 {$0=" 25  25  24  26  25"} 1' ../POSCAR > ./POSCAR
    atom=$(sed "${Line}q;d" POSCAR)
    sed -i "${Type4}i\ $atom" POSCAR
    if (("$Line" > "$Type")); then linenum=$(( $Line + 1 )); else linenum=
fi
    sed -i "${linenum}d" POSCAR
    cp ../POTCAR ./
    cp ../INCAR ./
    cp ../KPOINTS ./
    cp ../site${SITE}.slurm ./st${SITE}-sw4.slurm
    sbatch st*
    cd ..

    mkdir swap5
    cd swap5
    Type=$Type5
    awk 'NR==7 {$0=" 25  25  24  25  26"} 1' ../POSCAR > ./POSCAR
    atom=$(sed "${Line}q;d" POSCAR)
    sed -i "${Type5}i\ $atom" POSCAR
    if (("$Line" > "$Type")); then linenum=$(( $Line + 1 )); else linenum=
fi
    sed -i "${linenum}d" POSCAR
```

```
    cp ../POTCAR ./
    cp ../INCAR ./
    cp ../KPOINTS ./
    cp ../site${SITE}.slurm ./st${SITE}-sw5.slurm
    sbatch st*
    cd ..
# TYPE 4 ------------------------------------------------------------------
  elif [ $SITE -ge 76 ] && [ $SITE -le 100 ]; then
    mkdir vacancy
    cd vacancy
    awk 'NR==7 {$0=" 25  25  25  24  25"} 1' ../POSCAR > ./POSCAR
    sed -i "${Line}d" POSCAR
    cp ../POTCAR ./
    cp ../INCAR ./
    cp ../KPOINTS ./
    cp ../site${SITE}.slurm ./st${SITE}-vac.slurm
    sbatch st*
    cd ..

    mkdir swap1
    cd swap1
    Type=$Type1
    awk 'NR==7 {$0=" 26  25  25  24  25"} 1' ../POSCAR > ./POSCAR
    atom=$(sed "${Line}q;d" POSCAR)
    sed -i "${Type1}i\ $atom" POSCAR
    if (("$Line" > "$Type")); then linenum=$(( $Line + 1 )); else linenum=
fi
    sed -i "${linenum}d" POSCAR
    cp ../POTCAR ./
    cp ../INCAR ./
```

```
    cp ../KPOINTS ./
    cp ../site${SITE}.slurm ./st${SITE}-sw1.slurm
    sbatch st*
    cd ..

    mkdir swap2
    cd swap2
    Type=$Type2
    awk 'NR==7 {$0=" 25  26  25  24  25"} 1' ../POSCAR > ./POSCAR
    atom=$(sed "${Line}q;d" POSCAR)
    sed -i "${Type2}i\ $atom" POSCAR
    if (("$Line" > "$Type")); then linenum=$(( $Line + 1 )); else linenum=
fi
    sed -i "${linenum}d" POSCAR
    cp ../POTCAR ./
    cp ../INCAR ./
    cp ../KPOINTS ./
    cp ../site${SITE}.slurm ./st${SITE}-sw2.slurm
    sbatch st*
    cd ..

    mkdir swap3
    cd swap3
    Type=$Type3
    awk 'NR==7 {$0=" 25  25  26  24  25"} 1' ../POSCAR > ./POSCAR
    atom=$(sed "${Line}q;d" POSCAR)
    sed -i "${Type3}i\ $atom" POSCAR
    if (("$Line" > "$Type")); then linenum=$(( $Line + 1 )); else linenum=
fi
    sed -i "${linenum}d" POSCAR
```

```
    cp ../POTCAR ./
    cp ../INCAR ./
    cp ../KPOINTS ./
    cp ../site${SITE}.slurm ./st${SITE}-sw3.slurm
    sbatch st*
    cd ..

    mkdir swap5
    cd swap5
    Type=$Type5
    awk 'NR==7 {$0=" 25  25  25  24  26"} 1' ../POSCAR > ./POSCAR
    atom=$(sed "${Line}q;d" POSCAR)
    sed -i "${Type5}i\ $atom" POSCAR
    if (("$Line" > "$Type")); then linenum=$(( $Line + 1 )); else linenum=
fi
    sed -i "${linenum}d" POSCAR
    cp ../POTCAR ./
    cp ../INCAR ./
    cp ../KPOINTS ./
    cp ../site${SITE}.slurm ./st${SITE}-sw5.slurm
    sbatch st*
    cd ..
# TYPE 5 ------------------------------------------------------------------
  elif [ $SITE -ge 101 ] && [ $SITE -le 125 ]; then
    mkdir vacancy
    cd vacancy
    awk 'NR==7 {$0=" 25  25  25  25  24"} 1' ../POSCAR > ./POSCAR
    sed -i "${Line}d" POSCAR
    cp ../POTCAR ./
    cp ../INCAR ./
```

```
    cp ../KPOINTS ./
    cp ../site${SITE}.slurm ./st${SITE}-vac.slurm
    sbatch st*
    cd ..

    mkdir swap1
    cd swap1
    Type=$Type1
    awk 'NR==7 {$0=" 26  25  25  25  24"} 1' ../POSCAR > ./POSCAR
    atom=$(sed "${Line}q;d" POSCAR)
    sed -i "${Type1}i\ $atom" POSCAR
    if (("$Line" > "$Type")); then linenum=$(( $Line + 1 )); else linenum=
fi
    sed -i "${linenum}d" POSCAR
    cp ../POTCAR ./
    cp ../INCAR ./
    cp ../KPOINTS ./
    cp ../site${SITE}.slurm ./st${SITE}-sw1.slurm
    sbatch st*
    cd ..

    mkdir swap2
    cd swap2
    Type=$Type2
    awk 'NR==7 {$0=" 25  26  25  25  24"} 1' ../POSCAR > ./POSCAR
    atom=$(sed "${Line}q;d" POSCAR)
    sed -i "${Type2}i\ $atom" POSCAR
    if (("$Line" > "$Type")); then linenum=$(( $Line + 1 )); else linenum=
fi
    sed -i "${linenum}d" POSCAR
```

```
        cp ../POTCAR ./
        cp ../INCAR ./
        cp ../KPOINTS ./
        cp ../site${SITE}.slurm ./st${SITE}-sw2.slurm
        sbatch st*
        cd ..

        mkdir swap3
        cd swap3
        Type=$Type3
        awk 'NR==7 {$0=" 25  25  26  25  24"} 1' ../POSCAR > ./POSCAR
        atom=$(sed "${Line}q;d" POSCAR)
        sed -i "${Type3}i\ $atom" POSCAR
        if (("$Line" > "$Type")); then linenum=$(( $Line + 1 )); else linenum=
fi
        sed -i "${linenum}d" POSCAR
        cp ../POTCAR ./
        cp ../INCAR ./
        cp ../KPOINTS ./
        cp ../site${SITE}.slurm ./st${SITE}-sw3.slurm
        sbatch st*
        cd ..

        mkdir swap4
        cd swap4
        Type=$Type4
        awk 'NR==7 {$0=" 25  25  25  26  24"} 1' ../POSCAR > ./POSCAR
        atom=$(sed "${Line}q;d" POSCAR)
        sed -i "${Type}i\ $atom" POSCAR
        if (("$Line" > "$Type")); then linenum=$(( $Line + 1 )); else linenum=
```

```
fi
        sed -i "${linenum}d" POSCAR
        cp ../POTCAR ./
        cp ../INCAR ./
        cp ../KPOINTS ./
        cp ../site${SITE}.slurm ./st${SITE}-sw4.slurm
        sbatch st*
        cd ..
    fi
    cd ..
done
```

Appendix B

Synthesis and Characterization

B.1 Arc Melting

Each of the HEAs synthesized in this thesis were produced by the arc melting technique. An Series 5SA single–arc melter produced by Centorr Vacuum Industries was used for arc melting the alloys. Elemental powders of each of the relevant metals were purchased from Alfa Aesar. The purity of each metal used in the HEA synthesis was at least 99.99%. 20 gram pellets of each HEA were vacuum pressed in a Carver pellet die while the die pellet volume was under vacuum. The pellets were compressed with 9 ton force while under vacuum for 1 minute. Then, the vacuum–pressed pellets were placed within the copper hearth for casting. After sealing the hearth within the arc melter, a pump–an–purge procedure was conducted 10 times using a vacuum pump and 99.999% purity Ar source to ensure the volume of the arc melter was completely filled with inert gas to limit oxidation of the materials upon casting. Following electric arc melting of the vacuum–pressed pellet and cooling to room temperature through the circulated chilled–water, the solidified pellet was removed, flipped over, and recast. This was performed an additional 2 times for a total of 4 melts for each pellet.

B.2 Electron Microscopy

Two scanning electron microscopes equipped with enery–dispersive X–ray spectroscopy (EDX) were utilized in this thesis for microstructural and compositional analysis of the materials. The first is a JEOL 6610 microscope located in MIT building 4. The second is an Zeiss Nvision 40 located in MIT building NW13.

B.3 Electron Microprobe Analysis

The electron microprobe analysis was conducted with collaboration and generous assistance from Dr. Nilanjan Chatterjee of the MIT Department of Earth and Planetary Sciences using the JEOL–JXA–8200 Superprobe located in building 54 at MIT. The LaB_6 electron gun creates high beam currents with a smaller spot size than traditional SEM/EDX instruments providing a better signal strength and spatial resolution. The wavelength–dispersive X–ray spectrometer (WDS) provides a more accurate spectral analysis approach compared to EDX, facilitating highly accurate compositional analysis, while also being far more sensitive to light elements such as C, O, and N.

B.4 X–Ray Diffraction

The powder XRD measurements were performed at the MIT Materials Research Laboratory. A Bruker D8 Discover General Area Detector Diffraction System (GADDS) employing a 1.6kW sealed tube cobalt anode and Vantec-2000 two-dimensional detector was used to acquire the XRD spectra. These are acquired with sample rotation and scan axis oscillation to ensure that the data obtained are representative of the sample at large.

Bibliography

[1] H.G. Rickover. Academic vs. Practical Reactors, 1953. Statement to the U.S. Congress.

[2] R.C. Briant and A.M. Weinberg. Molten Fluorides as Power Reactor Fuels. *Nucl. Sci. Eng.*, 2:797–803, 1957.

[3] HG Olson, HL Brey, and FE Swart. The Fort St. Vrain high temperature gas-cooled reactor: VI. Evaluation and removal of primary coolant contaminants. *Nuclear Engineering and Design*, 61(3):315–322, 1980.

[4] KL Murty and I Charit. Structural materials for Gen-IV nuclear reactors: Challenges and opportunities. *Journal of Nuclear Materials*, 383(1-2):189–195, 2008.

[5] GS Was, D Petti, S Ukai, and S Zinkle. Materials for future nuclear energy systems. *J. Nucl. Mater.*, 527:151837, 2019.

[6] Genrich Altshuller. *And Suddenly the Inventor Appeared: TRIZ, the Theory of Inventive Problem Solving.* Technical Innovation Center, Inc., Worcester, MA, 1992.

[7] I Yu Litovchenko, NA Polekhina, AN Tyumentsev, EG Astafurova, VM Chernov, and MV Leontyeva-Smirnova. The effect of heat treatment on the microstructure and mechanical properties of heat-resistant ferritic–martensitic steel EK-181. *J. Nucl. Mater.*, 455(1-3):665–668, 2014.

[8] OI Eliseeva, VP Tsisar, VM Fedirko, and Ya S Matychak. Changes in the phase composition of an oxide film on EP-823 steel in contact with stagnant lead melt. *Materials Science*, 40(2):260–269, 2004.

[9] RG Pahl, CE Lahm, and SL Hayes. Performance of HT9 clad metallic fuel at high temperature. *Journal of Nuclear Materials*, 204:141–147, 1993.

[10] M Nie, J Zhang, F Huang, JW Liu, XK Zhu, ZL Chen, and LZ Ouyang. Microstructure evolution and life assessment of T92 steel during long-term creep. *Journal of alloys and compounds*, 588:348–356, 2014.

[11] JR Keiser. Compatibility studies of potential molten-salt breeder reactor materials in molten fluoride salts. Technical report, Oak Ridge National Lab., 1977.

[12] H McCoy and J Weir. Development of a titanium-modified hastelloy N with improved resistance to radiation damage. In *Irradiation Effects in Structural Alloys for Thermal and Fast Reactors*. ASTM International, 1969.

[13] Wenguan Liu, Han Han, Cuilan Ren, Xiujie He, Yanyan Jia, Song Wang, Wei Zhang, Zhijun Li, Xingtai Zhou, Yang Zou, et al. First-principles study of intergranular embrittlement induced by Te in the Ni Σ 5 grain boundary. *Computational materials science*, 88:22–27, 2014.

[14] Andrei A Komlev, Vyacheslav I Almjashev, Sevostian V Bechta, Vladimir B Khabensky, Vladimir S Granovsky, and Victor V Gusarov. New sacrificial material for ex-vessel core catcher. *Journal of Nuclear Materials*, 467:778–784, 2015.

[15] M Fischer, O Herbst, and H Schmidt. Demonstration of the heat removing capabilities of the EPR core catcher. *Nuclear Engineering and Design*, 235(10-12):1189–1200, 2005.

[16] R Gontard and H Nabielek. Performance evaluation of modern HTR TRISO fuels. Technical report, Kernforschungsanlage Jülich GmbH, 1990.

[17] Takaaki Koyanagi, Yutai Katoh, and Takashi Nozawa. Design and strategy for next-generation silicon carbide composites for nuclear energy. *Journal of Nuclear Materials*, 540:152375, 2020.

[18] Yutai Katoh and Lance L Snead. Silicon carbide and its composites for nuclear applications–Historical overview. *Journal of Nuclear Materials*, 526:151849, 2019.

[19] Joon-Soo Park, Akira Kohyama, Tatsuya Hinoki, Kazuya Shimoda, and Yi-Hyun Park. Efforts on large scale production of NITE-SiC/SiC composites. *Journal of Nuclear Materials*, 367:719–724, 2007.

[20] EN Hoffman, DW Vinson, RL Sindelar, DJ Tallman, G Kohse, and MW Barsoum. MAX phase carbides and nitrides: Properties for future nuclear power plant in-core applications and neutron transmutation analysis. *Nuclear Engineering and Design*, 244:17–24, 2012.

[21] Darin J Tallman, Elizabeth N Hoffman, N Caspi El'ad, Brenda L Garcia-Diaz, Gordon Kohse, Robert L Sindelar, and Michel W Barsoum. Effect of neutron irradiation on select MAX phases. *Acta Materialia*, 85:132–143, 2015.

[22] Martin Magnuson, Ola Wilhelmsson, J-P Palmquist, Ulf Jansson, M Mattesini, S Li, Rajeev Ahuja, and Olle Eriksson. Electronic structure and chemical bonding in Ti 2 Al C investigated by soft x-ray emission spectroscopy. *Physical Review B*, 74(19):195108, 2006.

[23] Thomas Lapauw, Joseph Halim, Jun Lu, Thierry Cabioc'h, Lars Hultman, Michel W Barsoum, Konstantza Lambrinou, and Jozef Vleugels. Synthesis of the novel Zr_3AlC_2 MAX phase. *Journal of the European Ceramic Society*, 36(3):943–947, 2016.

[24] Mohamed S El-Genk and Jean-Michel Tournier. A review of refractory metal alloys and mechanically alloyed-oxide dispersion strengthened steels for space nuclear power systems. *Journal of Nuclear materials*, 340(1):93–112, 2005.

[25] Tae Kyu Kim, Sanghoon Noh, Suk Hoon Kang, Jin Ju Park, Hyun Ju Jin, Min Ku Lee, Jinsugn Jang, and Chang Kyu Rhee. Current status and future prospective of advanced radiation resistant oxide dispersion strengthened steel (ARROS) development for nuclear reactor system applications. *Nuclear Engineering and Technology*, 48(2):572–594, 2016.

[26] Raul B Rebak. Nuclear applications of oxide dispersion strengthened and nano-featured alloys: an introduction. *JOM*, 66(12):2424–2426, 2014.

[27] Shigeharu Ukai and Masayuki Fujiwara. Perspective of ODS alloys application in nuclear environments. *Journal of Nuclear Materials*, 307:749–757, 2002.

[28] T Takeuchi, J Kameda, Y Nagai, T Toyama, Y Nishiyama, and K Onizawa. Study on microstructural changes in thermally-aged stainless steel weld-overlay cladding of nuclear reactor pressure vessels by atom probe tomography. *Journal of nuclear materials*, 415(2):198–204, 2011.

[29] Theodore A Lang. Significant corrosion of the Davis-Besse nuclear reactor pressure vessel head. In *ASME Pressure Vessels and Piping Conference*, volume 41596, pages 169–176, 2003.

[30] SH Shann and DR Olander. Stress corrosion cracking of zircaloy by cadmium, iodine, and metal iodides. *Journal of Nuclear Materials*, 113(2-3):234–248, 1983.

[31] Sachio Shimada and Masayuki Nagai. Evaluation of the resistance of irradiated zirconium-liner cladding to iodine-induced stress corrosion cracking. *Journal of Nuclear Materials*, 114(2-3):305–311, 1983.

[32] K Huang, CC Kammerer, DD Keiser, and YH Sohn. Diffusion barrier selection from refractory metals (Zr, Mo and Nb) via interdiffusion investigation for U-Mo RERTR fuel alloy. *Journal of phase equilibria and diffusion*, 35(2):146–156, 2014.

[33] T Egami, W Guo, PD Rack, and T Nagase. Irradiation resistance of multicomponent alloys. *Metallurgical and Materials Transactions A*, 45(1):180–183, 2014.

[34] Takeshi Nagase, Philip D Rack, Joo Hyon Noh, and Takeshi Egami. In-situ TEM observation of structural changes in nano-crystalline CoCrCuFeNi multicomponent high-entropy alloy (HEA) under fast electron irradiation by high voltage electron microscopy (HVEM). *Intermetallics*, 59:32–42, 2015.

[35] F Granberg, K Nordlund, MW Ullah, K Jin, C Lu, H Bei, LM Wang, F Djurabekova, WJ Weber, and Y Zhang. Mechanism of radiation damage reduction in equiatomic multicomponent single phase alloys. *Physical review letters*, 116(13):135504, 2016.

[36] B Gludovatz, A Hohenwarter, D Catoor, EH Chang, EP George, and RO Ritchie. A fracture-resistant high-entropy alloy for cryogenic applications. *Science*, 345(6201):1153–1158, 2014.

[37] Fabian Von Rohr, Michał J Winiarski, Jing Tao, Tomasz Klimczuk, and Robert Joseph Cava. Effect of electron count and chemical complexity in the Ta-Nb-Hf-Zr-Ti high-entropy alloy superconductor. *Proceedings of the National Academy of Sciences*, 113(46):E7144–E7150, 2016.

[38] ON Senkov, GB Wilks, DB Miracle, CP Chuang, and PK Liaw. Refractory high-entropy alloys. *Intermetallics*, 18(9):1758–1765, 2010.

[39] Oleg N Senkov, Daniel B Miracle, Kevin J Chaput, and Jean-Philippe Couzinie. Development and exploration of refractory high entropy alloys—a review. *Journal of materials research*, 33(19):3092–3128, 2018.

[40] A Kareer, JC Waite, B Li, A Couet, DEJ Armstrong, and AJ Wilkinson. Short communication: 'low activation, refractory, high entropy alloys for nuclear applications'. *J. Nucl. Mater.*, 526:151744, 2019.

[41] Aditya Ayyagari, Riyadh Salloom, Saideep Muskeri, and Sundeep Mukherjee. Low activation high entropy alloys for next generation nuclear applications. *Materialia*, 4:99–103, 2018.

[42] J-P Couzinié and G Dirras. Body-centered cubic high-entropy alloys: From processing to underlying deformation mechanisms. *Materials Characterization*, 147:533–544, 2019.

[43] Changning Niu. *First Principles Studies of NiFeCrCoMn High Entropy Alloys*. PhD thesis, North Carolina State University, Raleigh, North Carolina, 2015.

[44] Zemeng Yang, Dingshun Yan, Wenjun Lu, and Zhiming Li. A twip-trip quinary high-entropy alloy: Tuning phase stability and microstructure for enhanced mechanical properties. *Materials Science and Engineering: A*, 801:140441, 2021.

[45] Xiaoxiang Wu, David Mayweg, Dirk Ponge, and Zhiming Li. Microstructure and deformation behavior of two twip/trip high entropy alloys upon grain refinement. *Materials Science and Engineering: A*, 802:140661, 2021.

[46] Jing Su, Dierk Raabe, and Zhiming Li. Hierarchical microstructure design to tune the mechanical behavior of an interstitial trip-twip high-entropy alloy. *Acta Materialia*, 163:40–54, 2019.

[47] Easo P George, Dierk Raabe, and Robert O Ritchie. High-entropy alloys. *Nat. Rev. Mater.*, 4(8):515–534, 2019.

[48] Hongquan Song, Fuyang Tian, Qing-Miao Hu, Levente Vitos, Yandong Wang, Jiang Shen, and Nanxian Chen. Local lattice distortion in high-entropy alloys. *Physical Review Materials*, 1(2):023404, 2017.

[49] Yang Tong, Gihan Velisa, Shiteng Zhao, Wei Guo, Taini Yang, Ke Jin, Chenyang Lu, Hongbin Bei, JYP Ko, DC Pagan, et al. Evolution of local lattice distortion under irradiation in medium-and high-entropy alloys. *Materialia*, 2:73–81, 2018.

[50] Quanfeng He and Yong Yang. On lattice distortion in high entropy alloys. *Frontiers in Materials*, 5:42, 2018.

[51] E. A. Guggenheim. *Mixtures: the theory of the equilibrium properties of some simple classes of mixtures solutions and alloys*. Oxford University Press, London, 1952.

[52] William Paul Huhn and Michael Widom. Prediction of A2 to B2 phase transition in the high-entropy alloy Mo-Nb-Ta-W. *Jom*, 65(12):1772–1779, 2013.

[53] A Fernández-Caballero, JS Wróbel, PM Mummery, and D Nguyen-Manh. Short-range order in high entropy alloys: Theoretical formulation and application to Mo-Nb-Ta-VW system. *Journal of Phase Equilibria and Diffusion*, 38(4):391–403, 2017.

[54] Michael Widom. Modeling the structure and thermodynamics of high-entropy alloys. *Journal of Materials Research*, 33(19):2881–2898, 2018.

[55] Sheng Guo, Chun Ng, Jian Lu, and CT Liu. Effect of valence electron concentration on stability of fcc or bcc phase in high entropy alloys. *Journal of applied physics*, 109(10):103505, 2011.

[56] MC Troparevsky, JR Morris, PRC Kent, AR Lupini, and GM Stocks. Criteria for predicting the formation of single-phase high-entropy alloys. *Phys. Rev. X*, 5(1):011041, 2015.

[57] AR Miedema, PF De Chatel, and FR De Boer. Cohesion in alloys—fundamentals of a semi-empirical model. *Physica B+ c*, 100(1):1–28, 1980.

[58] MC Gao, CS Carney, ÖN Doğan, PD Jablonksi, JA Hawk, and DE Alman. Design of refractory high-entropy alloys. *Jom*, 67(11):2653–2669, 2015.

[59] Yong Zhang, Yun Jun Zhou, Jun Pin Lin, Guo Liang Chen, and Peter K Liaw. Solid-solution phase formation rules for multi-component alloys. *Advanced engineering materials*, 10(6):534–538, 2008.

[60] X Yang and Yong Zhang. Prediction of high-entropy stabilized solid-solution in multi-component alloys. *Materials Chemistry and Physics*, 132(2-3):233–238, 2012.

[61] Jian-Hong Li, Ting Chang, Ze-Chen Wu, and Ming-Hung Tsai. Quantitative prediction of solid solubility limit in single phase high-entropy alloys. *Applied Physics Letters*, 119(14):141906, 2021.

[62] Xiusong Huang, Lehua Liu, Xianbao Duan, Weibing Liao, Jianjun Huang, Huibin Sun, and Chunyan Yu. Atomistic simulation of chemical short-range order in hfnbtazr high entropy alloy based on a newly-developed interatomic potential. *Materials & Design*, 202:109560, 2021.

[63] Xiang-Guo Li, Chi Chen, Hui Zheng, Yunxing Zuo, and Shyue Ping Ong. Complex strengthening mechanisms in the NbMoTaW multi-principal element alloy. *npj Computational Materials*, 6(1):1–10, 2020.

[64] Ryoichi Kikuchi. A theory of cooperative phenomena. *Physical review*, 81(6):988, 1951.

[65] Damian Sobieraj, Jan S Wróbel, Tomasz Rygier, Krzysztof J Kurzydłowski, Osman El Atwani, Arun Devaraj, Enrique Martinez Saez, and Duc Nguyen-Manh. Chemical short-range order in derivative Cr–Ta–Ti–V–W high entropy alloys from the first-principles thermodynamic study. *Physical Chemistry Chemical Physics*, 22(41):23929–23951, 2020.

[66] Congyi Li. *Characterization of Radiation Effects and Ab Initio Modeling of Defects in a High Entropy Alloy for Nuclear Power Application*. PhD thesis, University of Tennessee–Knoxville, 2018.

[67] Congyi Li, Junqi Yin, Khorgolkhuu Odbadrakh, Brian C Sales, Steven J Zinkle, G Malcolm Stocks, and Brian D Wirth. First principle study of magnetism and vacancy energetics in a near equimolar NiFeMnCr high entropy alloy. *Journal of Applied Physics*, 125(15):155103, 2019.

[68] Samuel W McAlpine, Julie V Logan, and Michael P Short. Predicting single phase stability and segregation in the NbMoTaTi–(W, V) high entropy alloy system with the vacancy exchange potential. *Scripta Materialia*, 191:29–33, 2021.

[69] S.C. Middleburgh, D.M. King, G.R. Lumpkin, M. Cortie, and L. Edwards. Segregation and migration of species in the CrCoFeNi high entropy alloy. *Journal of Alloys and Compounds*, 599:179–182, 2014.

[70] Frederik Otto, Antonín Dlouhỳ, Konda Gokuldoss Pradeep, Monika Kuběnová, Dierk Raabe, G Eggeler, and Easo P George. Decomposition of the single-phase high-entropy alloy CrMnFeCoNi after prolonged anneals at intermediate temperatures. *Acta Materialia*, 112:40–52, 2016.

[71] Z Wang, CT Liu, and P Dou. Thermodynamics of vacancies and clusters in high-entropy alloys. *Physical Review Materials*, 1(4):043601, 2017.

[72] ON Senkov, GB Wilks, JM Scott, and DB Miracle. Mechanical properties of $Nb_{25}Mo_{25}Ta_{25}W_{25}$ and $V_{20}Nb_{20}Mo_{20}Ta_{20}W_{20}$ refractory high entropy alloys. *Intermetallics*, 19(5):698–706, 2011.

[73] Saad Sheikh, Samrand Shafeie, Qiang Hu, Johan Ahlström, Christer Persson, Jaroslav Veselỳ, Jiří Zỳka, Uta Klement, and Sheng Guo. Alloy design for intrinsically ductile refractory high-entropy alloys. *Journal of applied physics*, 120(16):164902, 2016.

[74] DM King, SC Middleburgh, L Edwards, GR Lumpkin, and M Cortie. Predicting the crystal structure and phase transitions in high-entropy alloys. *JOM*, 67(10):2375–2380, 2015.

[75] DJM King, SC Middleburgh, AG McGregor, and MB Cortie. Predicting the formation and stability of single phase high-entropy alloys. *Acta Mater.*, 104:172–179, 2016.

[76] Shun-Li Shang, Bi-Cheng Zhou, William Y Wang, Austin J Ross, Xuan L Liu, Yong-Jie Hu, Hua-Zhi Fang, Yi Wang, and Zi-Kui Liu. A comprehensive first-principles study of pure elements: Vacancy formation and migration energies and self-diffusion coefficients. *Acta Materialia*, 109:128–141, 2016.

[77] Shao-Ping Wang and Jian Xu. TiZrNbTaMo high-entropy alloy designed for orthopedic implants: As-cast microstructure and mechanical properties. *Materials Science and Engineering: C*, 73:80–89, 2017.

[78] Leonie Koch, Fredric Granberg, Tobias Brink, Daniel Utt, Karsten Albe, Flyura Djurabekova, and Kai Nordlund. Local segregation versus irradiation effects in high-entropy alloys: Steady-state conditions in a driven system. *Journal of Applied Physics*, 122(10):105106, 2017.

[79] Hongjing Cui, Ning Liu, Laima Luo, Yue Xu, Jigui Cheng, and Yucheng Wu. Behavior of high-entropy w-rich alloys wx(tavcrti)y under he+ irradiation. *Fusion Engineering and Design*, 172:112904, 2021.

[80] Owais Ahmed Waseem and Ho Jin Ryu. Powder metallurgy processing of a w x tativcr high-entropy alloy and its derivative alloys for fusion material applications. *Scientific reports*, 7(1):1–14, 2017.

[81] Owais Ahmed Waseem and Ho Jin Ryu. Helium ions irradiation analysis of w0. 5 (tativcr) 0.5 for application as a future fusion plasma-facing material. *Materials Chemistry and Physics*, 260:124198, 2021.

[82] Maximilien E Launey, Etienne Munch, Daan H Alsem, Holly B Barth, Eduardo Saiz, Antoni P Tomsia, and Robert O Ritchie. Designing highly toughened hybrid composites through nature-inspired hierarchical complexity. *Acta Materialia*, 57(10):2919–2932, 2009.

[83] Gururaja Udupa, S Shrikantha Rao, and KV Gangadharan. Functionally graded composite materials: an overview. *Procedia Materials Science*, 5:1291–1299, 2014.

[84] Irene H Chen, Wen Yang, and Marc A Meyers. Leatherback sea turtle shell: a tough and flexible biological design. *Acta biomaterialia*, 28:2–12, 2015.

[85] T Takeuchi, Y Kakubo, Y Matsukawa, Y Nozawa, T Toyama, Y Nagai, Y Nishiyama, J Katsuyama, Y Yamaguchi, K Onizawa, et al. Effects of thermal aging on microstructure and hardness of stainless steel weld-overlay claddings of nuclear reactor pressure vessels. *Journal of Nuclear Materials*, 452(1-3):235–240, 2014.

[86] Tohru Tobita, Makoto Udagawa, Yasuhiro Chimi, Yutaka Nishiyama, and Kunio Onizawa. Effect of neutron irradiation on the mechanical properties of weld overlay cladding for reactor pressure vessel. *Journal of Nuclear Materials*, 452(1-3):61–68, 2014.

[87] Kyle Johnson, Valter Ström, Janne Wallenius, and Denise Adorno Lopes. Oxidation of accident tolerant fuel candidates. *Journal of Nuclear Science and Technology*, 54(3):280–286, 2017.

[88] Steven J Zinkle, Kurt A Terrani, Jess C Gehin, Larry J Ott, and Lance Lewis Snead. Accident tolerant fuels for LWRs: A perspective. *Journal of Nuclear Materials*, 448(1-3):374–379, 2014.

[89] Tyler Dabney, Greg Johnson, Hwasung Yeom, Ben Maier, Jorie Walters, and Kumar Sridharan. Experimental evaluation of cold spray FeCrAl alloys coated zirconium-alloy for potential accident tolerant fuel cladding. *Nuclear Materials and Energy*, 21:100715, 2019.

[90] Keke Chang, Fanping Meng, Fangfang Ge, Gongshu Zhao, Shiyu Du, and Feng Huang. Theory-guided bottom-up design of the FeCrAl alloys as accident tolerant fuel cladding materials. *Journal of Nuclear Materials*, 516:63–72, 2019.

[91] Jean-Christophe Brachet, Isabel Idarraga-Trujillo, Marion Le Flem, Matthieu Le Saux, Valérie Vandenberghe, Stephane Urvoy, Elodie Rouesne, Thomas Guilbert, Caroline Toffolon-Masclet, Marc Tupin, et al. Early studies on Cr-Coated

Zircaloy-4 as enhanced accident tolerant nuclear fuel claddings for light water reactors. *Journal of Nuclear Materials*, 517:268–285, 2019.

[92] Samuel W McAlpine, Natasha C Skowronski, Weiyue Zhou, Guiqiu Tony Zheng, and Michael P Short. Corrosion of commercial alloys in flinak molten salt containing euf3 and simulant fission product additives. *Journal of Nuclear Materials*, 532:151994, 2020.

[93] D Kaoumi and V Jammot. Insights into the plastic behavior of irradiated ni-based alloy through in-situ tem experiments: Formation and evolution of defect-free channels. *Journal of Nuclear Materials*, 523:33–42, 2019.

[94] Michael P. Short. *Design of a functionally graded composite for service in high temperature lead and lead-bismuth cooled nuclear reactors*. PhD thesis, Massachusetts Institute of Technology, Cambridge, MA, 2010.

[95] Tomasz Durejko, Michał Ziętala, Wojciech Polkowski, and Tomasz Czujko. Thin wall tubes with Fe_3Al/SS316L graded structure obtained by using laser engineered net shaping technology. *Materials & Design*, 63:766–774, 2014.

[96] Weiping Liu and JN DuPont. Fabrication of functionally graded tic/ti composites by laser engineered net shaping. *Scripta Materialia*, 48(9):1337–1342, 2003.

[97] IS Winter, M de Jong, J Montoya, E Rothchild, and DC Chrzan. Intrinsic ductility of random substitutional alloys from nonlinear elasticity theory. *Physical Review Materials*, 3(11):113608, 2019.

[98] Maarten De Jong, Ian Winter, DC Chrzan, and Mark Asta. Ideal strength and ductility in metals from second-and third-order elastic constants. *Physical Review B*, 96(1):014105, 2017.

[99] Xinran Zhou, Sicong He, and Jaime Marian. Cross-kinks control screw dislocation strength in equiatomic bcc refractory alloys. *Acta Materialia*, 211:116875, 2021.

[100] Daniel Sheppard, Penghao Xiao, William Chemelewski, Duane D Johnson, and Graeme Henkelman. A generalized solid-state nudged elastic band method. *The Journal of chemical physics*, 136(7):074103, 2012.

[101] Graeme Henkelman, Blas P Uberuaga, and Hannes Jónsson. A climbing image nudged elastic band method for finding saddle points and minimum energy paths. *The Journal of chemical physics*, 113(22):9901–9904, 2000.

[102] Q Xu, HQ Guan, ZH Zhong, SS Huang, and JJ Zhao. Irradiation resistance mechanism of the CoCrFeMnNi equiatomic high-entropy alloy. *Scientific Reports*, 11(1):1–8, 2021.

[103] Alex Zunger, S-H Wei, LG Ferreira, and James E Bernard. Special quasirandom structures. *Phys. Rev. Lett.*, 65(3):353, 1990.

[104] C Wolverton. Crystal structure and stability of complex precipitate phases in Al–Cu–Mg–(Si) and Al–Zn–Mg alloys. *Acta Mater.*, 49(16):3129–3142, 2001.

[105] Chao Jiang. First-principles study of ternary bcc alloys using special quasirandom structures. *Acta Mater.*, 57(16):4716–4726, 2009.

[106] James E Saal and Chris Wolverton. Thermodynamic stability of Co–Al–W L12 γ'. *Acta Mater.*, 61(7):2330–2338, 2013.

[107] ZTY Liu, Benjamin P Burton, SV Khare, and D Gall. First-principles phase diagram calculations for the rocksalt-structure quasibinary systems TiN–ZrN, TiN–HfN and ZrN–HfN. *J. Phys.: Condens. Matter*, 29(3):035401, 2016.

[108] Yi Wang, Ming Yan, Qiang Zhu, Williams Yi Wang, Yidong Wu, Xidong Hui, Richard Otis, Shun-Li Shang, Zi-Kui Liu, and Long-Qing Chen. Computation of entropies and phase equilibria in refractory V-Nb-Mo-Ta-W high-entropy alloys. *Acta Mater.*, 143:88 – 101, 2018.

[109] A Van de Walle, P Tiwary, M De Jong, DL Olmsted, M Asta, A Dick, D Shin, Yi Wang, L-Q Chen, and Z-K Liu. Efficient stochastic generation of special quasirandom structures. *Calphad*, 42:13–18, 2013.

[110] Axel Van De Walle. Multicomponent multisublattice alloys, nonconfigurational entropy and other additions to the Alloy Theoretic Automated Toolkit. *Calphad*, 33(2):266–278, 2009.

[111] Georg Kresse and Jürgen Furthmüller. Efficiency of ab-initio total energy calculations for metals and semiconductors using a plane-wave basis set. *Comput. Mater. Sci*, 6(1):15–50, 1996.

[112] Jürgen Hafner. Ab-initio simulations of materials using VASP: Density-functional theory and beyond. *J. Comput. Chem.*, 29(13):2044–2078, 2008.

[113] Peter E Blöchl. Projector augmented-wave method. *Phys. Rev. B: Condens. Matter Mater. Phys.*, 50(24):17953, 1994.

[114] Georg Kresse and Daniel Joubert. From ultrasoft pseudopotentials to the projector augmented-wave method. *Phys. Rev. B: Condens. Matter Mater. Phys.*, 59(3):1758, 1999.

[115] Samuel W. McAlpine. Thesis code and data. `https://doi.org/10.5281/zenodo.5889125`, 2022.